



**UNIVERSITY OF THESSALY**  
**SCHOOL OF ENGINEERING**  
**DEPARTMENT OF MECHANICAL ENGINEERING**  
**LABORATORY OF FLUID MECHANICS & TURBOMACHINES**

**MASTER THESIS**

*Analytical and numerical study of the magnetohydrodynamic natural convection in an internally heated horizontal shallow cavity*

**Lefteris Benos**

**Physics Degree, Aristotelian Univ. of Thessaloniki**

**Examination Committee:**

Nicholas Vlachos	Advisor	Professor emeritus U. of Thessaly
Nikos Pelekasis	Member	Professor U. of Thessaly
Ioannis Sarris	Member	Assistant Professor of TEI of Athens

**ΒΟΛΟΣ - 2012**



© 2012 Μπένος Ελευθέριος

Η έγκριση της μεταπτυχιακής εργασίας από το Τμήμα Μηχανολόγων Μηχανικών της Πολυτεχνικής Σχολής του Πανεπιστημίου Θεσσαλίας δεν υποδηλώνει αποδοχή των απόψεων του συγγραφέα (Ν. 5343/32 αρ. 202 παρ. 2).

***“Theories are developed with the most sophisticated methods. However, it is only the plasma itself which does not understand how beautiful many mathematical theories are and absolutely refuses to obey them!”***

***Hannes Alfvén - winner of the 1970 Nobel Prize in Physics for his work on Magnetohydrodynamics***

## ***Acknowledgements***

Nuclear fusion has been called "the Holy Grail of the energy field". Thus, the choice of an attractive energy source because of its virtually inexhaustible supply of fuel, the promise of minimal adverse environmental impact and its inherent safety motivated me to undertake this study. Therefore, I wholeheartedly enjoyed the challenge of examining and researching a controversial issue that will greatly impact the whole world in the next decades.

For the completion of this Thesis, I would like to thank the members of my advisory committee. First of all, I am most grateful to my supervisor, emeritus professor Nikolas Vlachos, to associate professor Nikos Pelekasis and to assistant professor Ioannis Sarris for their scientific and friendly advice on this Master thesis and also for their support during the Master program. Besides, they introduced me to the Physics of Fluids and Computational Fluid Mechanics via the Master courses.

Thanks also extended to the associate professor Nikolaos Andritsos and professor Dimitris Valougeorgis for their crucial contribution in understanding the true meaning of Transport Phenomena.

Furthermore, very special thanks go to the post-doc researcher Dr. Sotiris Kakaratzas for his opinions, criticism, useful remarks and true support in this Thesis.

I would also like to thank the post-doc researcher Dr. Christos Dritselis and the PhD students of the University of Thessaly Dimitris Dimopoulos and Alexandros Iatridis for the constructive discussions on Magnetohydrodynamics. Also, the PhD student of the University of Texas Nikolaos Vergos for his contribution in understanding the strange paths of plasma physics and controlled nuclear fusion.

Finally, I would like to thank Dimitris Tsokolis and Petros Christodoulou, who attended together with me the Master program, for their friendship. Also, I would be ungrateful if I did not mention my office mate Nikolaos Polychronopoulos who was supporting me with his company for at least 12 hours per day.

Last but not least, special recognition goes to my family and my girlfriend Ioanna for their continuous support and encouragement during this study.

To conclude, this work is financially supported by the European Commission within the Association EURATOM-Hellenic Republic. The views expressed in this thesis are the sole responsibility of the author and do not necessarily reflect the views of the European Commission.



## SUMMARY

Magnetohydrodynamic (MHD) natural convection in enclosures has received considerable attention in the past few decades. The interest comes from its importance in a variety of technological, geophysical and engineering applications, such as nuclear reactors, cooling of electrical equipment, solar collectors and crystals manufacturing. The main motive of the research presented in this Thesis is related to the ongoing European and worldwide research in Fusion science and technology.

Firstly, the MHD natural convection flow in shallow horizontal cavities due to internal heating is studied analytically by means of asymptotic expansions. The hydrodynamic part of the flow has already been solved by Daniels & Jones (1998). Using their framework, the solution is extended for the case where the cavity contains an electrically conductive fluid in the presence of a uniform transverse magnetic field. More specifically, the shallow rectangular cavity consists of two adiabatic horizontal walls and two isothermal vertical walls, held at the same uniform temperature. The natural convection flow is driven by a uniformly distributed internal heat source. The resulting flow consists of a symmetric double-cell circulation with fluid ascending in the center of the cavity and descending in the regions of the end walls. The analysis is limited to laminar flows before any unstable convection or multicellular flow structures being developed. These analytical solutions are particularly helpful for the determination of the flow patterns with inexpensive calculations. In addition to the analytical solution, the same flow is also studied numerically for a range of Hartmann, Prandtl and Rayleigh numbers in order to verify the accuracy and validity of the analytical results, to calculate the constants arising in the analytical approach and to characterize the non-linear regions of the flow. This low- $R_m$  numerical model was developed within OpenFOAM CFD library. Finally, the comparison of the results between the analytical and numerical solutions was found to be fairly good and this indicates the correctness of our analysis and its applicability.

Much work has been carried out in the past in an effort to study numerically the MHD natural convection flow. In the majority of these models, the Lorentz force due to the magnetic field is suppressed into a damping term resisting the fluid motion. Using this hypothesis, commonly called the low- $R_m$  approximation, there is a considerable reduction of the number of equations required to be solved.

The scope and the contribution of the present Master thesis were, apart from finding an analytical approach in order to describe the MHD natural convection flows, to develop a full MHD numerical model.

The aforementioned in-house numerical models were initially validated before any simulation took place. Specifically, the low- $R_m$  and full MHD models, which were developed during this research work, were compared successfully with the work of Al-Najem et al. (1998). The full MHD model, on the other hand, was validated using the work of Orszag and Tang (1979). Then, the energy equation and the Boussinesq approximation were added in the full MHD model and were validated successfully with the results of Sarris et al. (2006). Both studies of Al-Najem et al. (1998) and Sarris et al. (2006) deal with cavities whose the horizontal walls are perfectly insulated, while the vertical ones are isothermal with the left wall at high temperature and the right one at low temperature. The fluid is permeated by a uniform external magnetic field. They assumed that the induced magnetic field produced by the motion of the electrically conducting fluid is negligible compared to the externally applied magnetic field.

In the present numerical models, Joule heating and viscous dissipation were considered negligible. All numerical calculations in this thesis were carried out using the Open Source Field Operation and Manipulation (OpenFOAM) software, a C++ class library which uses object-orientation techniques that enable the creation of data types that closely mimics those of continuum mechanics, OpenFOAM (2004).



## ΠΕΡΙΛΗΨΗ

Η μελέτη των ροών της μαγνητοϋδροδυναμικής (ΜΥΔ) φυσικής συναγωγής μέσα σε δοχεία έλαβαν τα τελευταία χρόνια μεγάλη διάσταση. Το ενδιαφέρον γι' αυτές τις ροές έγκειται στις εφαρμογές που βρίσκουν σε ένα μεγάλο εύρος τεχνολογικών, γεωφυσικών και μηχανολογικών τομέων. Παραδείγματα αυτών των εφαρμογών αποτελούν οι πυρηνικοί αντιδραστήρες, η ψύξη ηλεκτρικού εξοπλισμού και ηλιακών συλλεκτών και η δημιουργία κρυστάλλων. Τα τελευταία χρόνια, η τεχνολογία απαγωγής της θερμότητας από αντιδραστήρες σύντηξης και της μεταφοράς της σε εναλλάκτες θερμότητας για την παραγωγή ατμού είναι μια σημαντική εφαρμογή. Κατόπιν, ο παραγόμενος ατμός περνά μέσα από στροβίλους οι οποίοι παράγουν ηλεκτρικό ρεύμα.

Αρχικά, στην παρούσα μεταπτυχιακή εργασία μελετάται η δισδιάστατη μαγνητοϋδροδυναμική φυσική συναγωγή σε ορθογώνιες αβαθείς κοιλότητες εξαιτίας ομοιόμορφα κατανεμημένων εσωτερικών πηγών θερμότητας. Πιο αναλυτικά, εξετάζεται η ροή όταν τα οριζόντια τοιχώματα είναι αδιαβατικά ενώ τα κατακόρυφα διατηρούνται στην ίδια θερμοκρασία. Σαν μία πρώτη προσέγγιση αυτού του προβλήματος χρησιμοποιείται η μέθοδος των ασυμπτωτικών αναπτυγμάτων για την περίπτωση που στην παραπάνω ροή επιδρά εξωτερικό μαγνητικό πεδίο παράλληλο στο διάνυσμα της επιτάχυνσης της βαρύτητας. Το υδροδυναμικό σκέλος (δηλαδή απουσία εξωτερικού μαγνητικού πεδίου) έχει ήδη λυθεί από τους Daniels & Jones (1998). Επιβάλλοντας εξωτερικό μαγνητικό πεδίο παράλληλο στο διάνυσμα της επιτάχυνσης της βαρύτητας, η αλληλεπίδραση μεταξύ των αριθμών Rayleigh, Prandtl και Hartmann είναι αυτή που καθορίζει την ροή. Η ροή οδηγείται από τις ομοιόμορφα κατανεμημένες πηγές θερμότητας και χαρακτηρίζεται από δύο συμμετρικές ανακυκλοφορίες με το ρευστό να ανέρχεται στο κεντρικό τμήμα της κοιλότητας και να κατέρχεται στα κάθετα τοιχώματα. Η ανάλυση περιορίζεται για μικρούς αριθμούς Rayleigh και για στρωτή ροή. Η μελέτη της ροής με τα ασυμπτωτικά αναπτύγματα είναι πολύ χρήσιμη λόγω της αποφυγής των χρονοβόρων αριθμητικών μοντέλων.

Στα όρια όπου ο αριθμός Hartmann τείνει στο μηδέν τα αποτελέσματα της παρούσας μελέτης ταυτίζονται ακριβώς με αυτά των Daniels & Jones (1998), κάτι που ενισχύει τα αποτελέσματα που αποκομίστηκαν.

Πέρα την αναλυτικής λύσης με την μέθοδο των ασυμπτωτικών αναπτυγμάτων, στην παρούσα μεταπτυχιακή εργασία μελετήθηκε το προαναφερθέν πρόβλημα

μαγνητοϋδροδυναμικής φυσικής συναγωγής και αριθμητικά. Συγκεκριμένα, οι μερικές διαφορικές εξισώσεις της ροής, της μετάδοσης θερμότητας μαζί με τις συνοριακές τους συνθήκες επιλύθηκαν αριθμητικά με την μέθοδο των πεπερασμένων όγκων. Σε αυτή την μέθοδο οι εξισώσεις διακριτοποιούνται σε ένα αριθμό πεπερασμένων όγκων. Οι ποσότητες υπολογίζονται στο κέντρο του κάθε όγκου. Τα διαφορικά, από την άλλη πλευρά, υπολογίζονται με βάση τις διακριτές τιμές των μεταβλητών στις θέσεις που έχουν τοποθετηθεί. Η σύνδεση της ορμής με την πίεση γίνεται μέσω της μεθόδου PISO. Τέλος, το πλέγμα, κατασκευάστηκε πιο πυκνό κοντά στα τοιχώματα έτσι ώστε να είναι πιο ακριβής η μελέτη στον υπολογισμό των οριακών στρωμάτων.

Στην μεγάλη πλειοψηφία των άρθρων που έχουν δημοσιευτεί έχει εφαρμοστεί η προσέγγιση χαμηλού μαγνητικού αριθμού Reynolds (low- $R_m$  approximation) που οδηγεί στην μείωση των προς λύση εξισώσεων. Με αυτόν το τρόπο, συνεπώς, μειώνεται το υπολογιστικό κόστος, αφού αγνοείται η επαγωγή του μαγνητικού πεδίου που επιφέρει η κίνηση του αγώγιμου ρευστού. Με άλλα λόγια αγνοείται η εξίσωση της επαγωγής του Faraday. Ο όρος της δύναμης Lorentz μειώνεται στον  $-\sigma B_0^2 V_{καθ}$ , όπου  $V_{καθ}$  είναι η κάθετη συνιστώσα της ταχύτητας στην διεύθυνση του εξωτερικού μαγνητικού πεδίου  $B_0$  και  $\sigma$  η ηλεκτρική αγωγιμότητα του ρευστού.

Ο σκοπός και η συνεισφορά της παρούσας εργασίας είναι αρχικά να βρεθεί μία αναλυτική λύση που να περιγράφει την ΜΥΔ φυσική συναγωγή με τις προαναφερθείσες συνοριακές συνθήκες. Αφετέρου, να δημιουργηθεί ένα ΜΥΔ αριθμητικό μοντέλο που να περιλαμβάνει και την επαγωγή του μαγνητικού πεδίου που επιφέρει η κίνηση του αγώγιμου ρευστού.

Εν συντομία, τα αποτελέσματα των αναλυτικών λύσεων δείχνουν ότι τα προφίλ της θερμοκρασίας είναι σε συμφωνία με αυτά του OpenFOAM για μικρά Rayleigh, ενώ για μεγάλα Hartmann οι λύσεις είναι ίδιες με αυτές των προσομοιώσεων και ανεξάρτητες από την επιλογή του αριθμού Rayleigh. Τα προφίλ της θερμοκρασίας, τέλος, φαίνονται να είναι ανεξάρτητα του αριθμού Prandtl για τους συνδυασμούς των αδιάστατων αριθμών που χρησιμοποιήθηκαν.

Όσο αναφορά τα προφίλ της ταχύτητας που λήφθηκαν με την μέθοδο των ασυμπτωτικών αναπτυγμάτων, δείχνουν την τάση του μαγνητικού πεδίου να επιβραδύνει την ροή του αγώγιμου ρευστού. Επιπλέον, η αύξηση του αριθμού Rayleigh κάνει την ροή να χαρακτηρίζεται πιο πολύ από συναγωγή.

Η αναλυτική προσέγγιση, δεν μπορούσε να προβλέψει την συμπεριφορά του ρευστού κοντά στα κάθετα τοιχώματα. Εκεί η μελέτη πρέπει να γίνει με σειρές

αναπτυγμάτων, κάτι που φαίνεται στην εργασία των Garandet et al. (1992). Όπως έδειξαν οι προσομοιώσεις, υπάρχει μια σθεναρή καθοδική κίνηση κοντά στα κάθετα ισόθερμα τοιχώματα που εξαρτάται από τον συνδυασμό των προαναφερθέντων αδιάστατων αριθμών. Τα προφίλ της κάθετης συνιστώσας της ταχύτητας στο μέσο της κοιλότητας στην αναλυτική λύση φαίνονται να είναι σε συμφωνία με αυτά των αριθμητικών προσομοιώσεων για μικρούς αριθμούς Rayleigh, ενώ για εφαρμογή μεγάλων εξωτερικών μαγνητικών πεδίων τα αποτελέσματα συγκλίνουν ανεξάρτητα από την επιλογή αριθμού Rayleigh.

Όλα τα αριθμητικά μοντέλα έλαβαν χώρα μέσα στο υπολογιστικό πακέτο OpenFOAM (Open Source Field Operation and Manipulation), το οποίο είναι γραμμένο σε γλώσσα C++ και χρησιμοποιεί αντικειμενοστραφή προγραμματισμό που δίνει την δυνατότητα στην δημιουργία τελεστών που “μιμούνται” αυτούς της υπολογιστικής ρευστοδυναμικής. Πριν τις αριθμητικές προσομοιώσεις που αφορούν την δισδιάστατη μαγνητοϋδροδυναμική φυσική συναγωγή σε ορθογώνιες αβαθείς κοιλότητες έγινε επιτυχής σύγκριση των μοντέλων με κάποια από την βιβλιογραφία. Συγκεκριμένα, για το low- $R_m$  μοντέλο ελέγχθηκε η εγκυρότητα του με βάση την εργασία των Al-Najem et al. (1998). Το full MHD μοντέλο, από την άλλη πλευρά, συγκρίθηκε αρχικά με την εργασία των Orszag και Tang (1979). Επιπροσθέτως, μετά την προσθήκη της εξίσωσης της ενέργειας και της προσέγγισης Boussinesq ελέγχθηκαν επιτυχώς με αυτό των Sarris et al. (2006). Και τα δύο προαναφερθέντα άρθρα πραγματεύονται τετραγωνικές δισδιάστατες κοιλότητες με τα οριζόντια τοιχώματα να είναι θερμικά μονωμένα, ενώ τα κάθετα διατηρούνται σε σταθερή θερμοκρασία. Το αριστερό τοίχωμα είναι σε υψηλότερη θερμοκρασία  $T_H$ , ενώ το δεξί αποτελεί το κρύο τοίχωμα με θερμοκρασία  $T_C$ . Στο αγωγίμο ρευστό εφαρμόζεται εξωτερικό μαγνητικό πεδίο  $B_0$ .

Στα αριθμητικά μοντέλα που δημιουργήθηκαν, η θέρμανση εξαιτίας του φαινομένου Joule και ιξώδους σκέδασης θεωρήθηκαν αμελητέα. Τέλος, και οι δύο κώδικες έγιναν σε αδιάστατη μορφή ώστε να είναι εύκολη η χρησιμοποίησή τους από οποιοδήποτε ερευνητή θέλει να ασχοληθεί με φαινόμενα μαγνητοϋδροδυναμικής αλλά και υδροδυναμικής συναγωγής (θέτοντας  $Ha=0$ ) μέσα σε αβαθείς κοιλότητες.

# Contents

Acknowledgements.....	v
SUMMARY.....	vii
ΠΕΡΙΛΗΨΗ.....	ix
Contents.....	xii
Nomenclature.....	xvii
Outline of the Thesis.....	1
Contribution and novelties of the Thesis.....	1
CHAPTER 1: CONTROLLED THERMONUCLEAR FUSION.....	2
1.1 What is Fusion?.....	2
1.2 Approaches to Fusion.....	4
1.2.1 Magnetic Mirror.....	4
1.2.2 Z-Pinch.....	5
1.2.3 Stellarator.....	5
1.2.4 Tokamak.....	6
1.2.5 Basic components of the Tokamak.....	7
1.3 Plasma Heating.....	9
1.4 The Case of Fusion.....	11
1.5 Fusion versus Fission.....	13
1.6 Relation of Present Work to Controlled Thermonuclear Fusion.....	13
CHAPTER 2: MAGNETOHYDRODYNAMICS.....	15
2.1 Introduction.....	15
2.2 Basic concepts on electromagnetic theory.....	16
2.3 Ideal MHD.....	20
2.4 Resistive MHD.....	22
2.5 MHD turbulence.....	26

CHAPTER 3: MAIN CHARACTERISTICS OF OPENFOAM .....	32
3.1 History.....	32
3.2 Features of OpenFOAM .....	32
3.3 Standard Solvers.....	32
3.4 Creating Solvers.....	33
3.5 File structure of OpenFOAM cases .....	35
3.6 Numerical schemes .....	36
3.7 Mesh generation with the blockMesh utility.....	39
3.8 Linear solver control .....	40
3.9 Post-processing .....	43
Epilogue .....	43
CHAPTER 4: THE ORSZAG-TANG VORTEX MHD FLOW .....	45
4.1. Literature survey .....	45
4.2. Orszag-Tang vortex modeling in the OpenFoam CFD library .....	50
CHAPTER 5: MHD NATURAL CONVECTION IN SHALLOW CAVITIES .....	58
5.1. Literature survey .....	58
5.2 Geometry and mathematical formulation.....	59
5.3 Analytical solutions with matched asymptotic expansions .....	63
5.4 Numerical simulation of MHD natural convection in an internally heated horizontal shallow cavity with OpenFOAM CFD library .....	68
CLOSURE AND FUTURE WORK.....	85
References.....	86
Appendix.....	90
A. Orszag-Tang vortex.....	90
B. Magnetohydrodynamic natural convection in a differentially heated shallow cavity with transverse magnetic field (numerical results) .....	94
C. Two dimensional magnetohydrodynamic natural convection flow in an internally heated shallow cavity (comparison of the analytical and numerical results) .....	98
CURRICULUM VITAE.....	108

## List of Figures

<b>Fig. 1.1</b> A sufficiently high kinetic energy of the nuclei is needed to overcome the Coulomb force	3
<b>Fig. 1.2</b> Magnetic mirror plasma confinement configuration	5
<b>Fig. 1.3</b> Z-Pinch configuration	5
<b>Fig. 1.4</b> Stellarator configuration	6
<b>Fig. 1.5</b> Tokamak configuration	6
<b>Fig. 1.6</b> Vacuum vessel	7
<b>Fig. 1.7</b> Magnets: (a) toroidal field system, (b) poloidal field system and (c) central solenoid	8
<b>Fig. 1.8</b> Blanket	8
<b>Fig. 1.9</b> Divertor	8
<b>Fig. 1.10</b> Cryostat	9
<b>Fig. 1.11</b> Diagnostics	9
<b>Fig. 1.12</b> (a) Neutral beam heating and (b) radio-frequency heating	10
<b>Fig. 1.13</b> (a) High efficiency plasma lighting and (b) robotically controlled plasma spraying of high-temperature shielding tiles	11
<b>Fig. 2.1</b> Computing the magnetic flux through a volume element swept out by a surface moving with the fluid	21
<b>Fig. 2.2</b> Magnetic reconnection in a slab plasma	25
<b>Fig. 2.3</b> Flow pattern in the vicinity of a magnetic island	25
<b>Fig. 2.4</b> Measurement of a fluctuating velocity field	27
<b>Fig. 2.5</b> Illustration of the cascade of energy from large to small wavelength as a result of nonlinear mode coupling	28
<b>Fig. 2.6</b> In MHD turbulence, eddies tend to be elongated in the direction of the magnetic field	29
<b>Fig. 2.7</b> The spatial structure at small scales in intermittent turbulence	30
<b>Fig. 2.8</b> Spectrum of fluctuations in the magnetic energy in a region of the earth's magnetosphere as measured by the CLUSTER mission	31
<b>Fig. 3.1:</b> File structure of an ordinary OpenFOAM case	36
<b>Fig. 4.1.</b> The Orszag-Tang problem: Plot of the energy dissipation rate $\epsilon(t)$ of the 2-D MHD flow. (a) $\nu=\eta= 0.08$ ( $Ra=36$ ), $\nu=\eta= 0.04$ ( $Ra=92$ ), $\nu=\eta= 0.02$ ( $Ra=232$ ), $\nu=\eta= 0.01$ ( $Ra=585$ ), $\nu=\eta= 0.005$ ( $Ra=1474$ )	49
<b>Fig. 4.2</b> The Orszag-Tang problem. Distributions of energy (kinetic( $E_K$ ), magnetic ( $E_M$ ) and their sum $E_T$ ) together with the cross helicity ( $H_c$ ), normalized by $8\pi^2$ , for the run with $\nu=\eta= 0$ on a 512x512 grid	49
<b>Fig. 4.3</b> Initial distribution of the Orszag-Tang problem using a 512x512 grid: (a) Velocity and (b) Magnetic field	90

<b>Fig. 4.4</b> Distributions of the Orszag-Tang problem at $t=1$ using a $512 \times 512$ grid: (a) Velocity field, (b) Magnetic field, (c), Current density and (d) Vorticity	90
<b>Fig. 4.5a</b> Distributions of the Orszag-Tang problem at $t=1$ using a $512 \times 512$ grid: (a) Velocity field, (b) Magnetic field, (c) Current density and (d) Vorticity from 0 to 1 with a 0.2 time step	91
<b>Fig. 4.5b</b> Distributions of the Orszag-Tang problem at $t=1$ using a $512 \times 512$ grid: (a) Velocity field, (b) Magnetic field, (c) Current density and (d) Vorticity from 1.2 to 2 with a 0.2 time step	92
<b>Fig.4.6</b> Evolution of kinetic, magnetic and total energy for $\eta=\nu=0.02$ using a $512 \times 512$ grid	93
<b>Fig. 5.1</b> Flow configuration and boundary conditions	59
<b>Fig. 5.2</b> Flow configuration of Al-Najem et al (1998)	70
<b>Fig. 5.3</b> Flow configuration and boundary conditions of the present model	72
<b>Fig. 5.4</b> Profiles of the streamfunction field for various values of $Ha$ and $Gr=10^6$ . OpenFOAM`s profiles represent the streamfunction in the middle area of the cavity	94
<b>Fig. 5.5</b> Comparison between the isotherms conducted by Al-Najem et al (1998) and OpenFOAM for various values of $Ha$ at $Gr=10^6$	95
<b>Fig. 5.6</b> Comparison of the midsection velocity between the present low- $R_m$ model and Al-Najem et. Al (1998) at $Ha=10$ and $Gr=10^4$	96
<b>Fig. 5.7</b> Comparison of the midsection velocity between the present full MHD model and Sarris et. al at $Ha=10$ and $Gr=10^4$	96
<b>Fig. 5.8</b> Comparison of the midsection velocity between the low- $R_m$ and full MHD models applied in OpenFOAM at $Ha=10$ and $Gr=10^4$	96
<b>Fig. 5.9</b> Velocity profiles at the midsection of the cavity for different values of $Ha$ at $Gr=10^4$ with the low- $R_m$ model applied in OpenFOAM	97
<b>Fig. 5.10</b> Temperature profiles at the midsection of the cavity for different values of $Ha$ at $Gr=10^4$ with the low- $R_m$ model applied in OpenFOAM	97
<b>Fig. 5.11</b> One fourth of the grid used for the 2-D MHD natural convection flow	76
<b>Fig. 5.12</b> Temperature profiles obtained by the low- $R_m$ numerical model for $Pr=0.0321$ , 0.7 and 7, and $R_s=3000$ : (a) $Ha=5$ , (b) $Ha=15$ , (c) $Ha=50$	99
<b>Fig. 5.13</b> Core temperature profiles for various values of $R_s$ : (a) $Ha=0$ , (b) $Ha=5$ , (c) $Ha=15$ , (d) $Ha=30$ , (e) $Ha=50$	99
<b>Fig. 5.14</b> Core temperature profiles for various values of $Ha$ : (a) $R_s=200$ , (b) $R_s=1000$ , (c) $R_s=3000$ , (d) $R_s=5000$	100
<b>Fig. 5.15</b> Variation of the average Nusselt number with (a) $R_s$ and (b) $Ha$	100
<b>Fig. 5.16</b> Distribution of the local Nusselt number for various values $R_s$ : (a) $Ha=0$ , (b) $Ha=5$ , (c) $Ha=15$ , (d) $Ha=30$ , (e) $Ha=50$	101
<b>Fig. 5.17</b> Distribution of the local Nusselt number for various values of $Ha$ : (a) $R_s=200$ , (b) $R_s=1000$ , (c) $R_s=3000$ , (d) $R_s=5000$	102
<b>Fig. 5.18</b> Distribution of the core streamfunction $\psi_0$ at mid-cavity height ( $z=0$ ) for various values of	103

$R_s$ : (a)  $Ha=0$ , (b)  $Ha=5$ , (c)  $Ha=15$ , (d)  $Ha=30$ , (e)  $Ha=50$

**Fig. 5.19** Distribution of the core streamfunction  $\psi_0$  at mid-cavity height ( $z=0$ ) for various values of  $Ha$ : (a)  $R_s=200$ , (b)  $R_s=1000$ , (c)  $R_s=3000$ , (d)  $R_s=5000$  104

**Fig. 5.20** Distribution of the maximum analytical core streamfunction  $\psi_0$  for various values of (a)  $R_s$  and (b)  $Ha$  104

**Fig. 5.21** Distribution of the vertical velocity at mid-cavity height ( $z=0$ ) for various values of  $R_s$ : (a)  $Ha=0$ , (b)  $Ha=5$ , (c)  $Ha=15$ , (d)  $Ha=30$ , (e)  $Ha=50$  105

**Fig. 5.22** Distribution of the vertical velocity at mid-cavity height ( $z=0$ ) for various values of  $Ha$ : (a)  $R_s=200$ , (b)  $R_s=1000$ , (c)  $R_s=3000$ , (d)  $R_s=5000$  106

**Fig. 5.23** Temperature and streamlines contours for  $Ha=5$  and  $R_s=200, 3000$  and  $5000$  107

**Fig. 5.24** Temperature and streamlines contours for  $R_s=3000$  and  $Ha=5, 15$  and  $50$  107

### **List of Tables**

**Table 1.1** Comparison chart between nuclear fusion and nuclear fission 13

**Table 3.1** Solver descriptions 33

**Table 3.2** Main keywords used in fvSchemes 38

**Table 3.3** Interpolation schemes 38

**Table 3.4** Discretization schemes available in gradSchemes 39

**Table 3.5** Discretization schemes available in ddtSchemes 39

**Table 3.6** Edge types available in the blockMeshDict dictionary 40

**Table 3.7** Linear solvers (\*PCG for symmetric matrices, PBiCG for asymmetric) 42

**Table 3.8** Preconditioner options 43

**Table 5.1** Comparison of the present low- $R_m$  model calculations with those of Al-Najem et al. (1998) for the case of  $Pr=0.733$ ,  $Gr = 10^4$  and  $Ha=10$  74

**Table 5.2** Comparison of the present full MHD model calculations with those of Sarris et al. (2006) for the case of  $Pr=0.733$ ,  $Gr = 10^4$  and  $Ha=10$  74

**Table 5.3** Comparison of the full MHD calculations with those of low- $R_m$  applied in OpenFOAM for the case of  $Pr=0.733$ ,  $Gr = 10^4$  and  $Ha=10$  75

**Table 5.4** Values of both analytical and numerical temperatures at  $\xi=1/2$  and  $z=0$ , for various combinations of  $Ha$  and  $R_s$  and  $Pr$  80



## Nomenclature

a	Thermal diffusivity	M	Mass of the individual positively charged particles
<b>B</b>	Magnetic field	$n_0$	Average number density of positive and negative charges
C	Speed of light	P	Pressure
$c_p$	Specific heat at constant pressure	P(V)	Probability distribution function (PDF)
$d_i$	Ion skin depth	Q	Volumetric heat generation rate
<b>E</b>	Electric field	$S_\phi$	Source term
$E_K$	Kinetic energy	t	Time
$E_M$	Magnetic energy	T	Fluid temperature
$E_T$	Total energy	U	Potential energy
h	Cavity height	u, w	Velocity components in x and z directions, respectively
$H_c$	Cross-helicity	$V_A$	Alfven velocity
J	Electric current density	$w_{an}$	Analytical vertical velocity
k	Wave number	x, y, z	Spatial coordinates
<b>Greek symbols</b>			
B	Volumetric expansion coefficient	$\rho$	Number density
$\Gamma_\phi$	Diffusivity	$\rho_q$	Electric charge density
$\varepsilon(t)$	Energy dissipation rate	$\tau$	Viscous stress tensor
$\varepsilon_0$	Permittivity of free space	$\tau_A$	Alfven time
$\eta$	Electrical resistivity	$\tau_R$	Resistive diffusion time
$\Theta$	Dimensionless fluid temperature	$\Phi$	Flow quantity
$\lambda_D$	Debye length	$\phi$	Electrostatic potential
M	Dynamic viscosity	$\psi$	Stream function
$\mu_0$	Permeability of free space	$\Omega$	Ion gyro-frequency
$\nu$	Kinematic viscosity	$\omega_{pi}$	Plasma frequency
<b>Dimensionless numbers</b>			
Ra	Rayleigh number	Re	Reynolds number
$R_s$	Scaled Rayleigh number	$R_m$	Magnetic Reynolds number
Gr	Grashof number	Pr	Prandtl number
Ha	Hartmann number	Co	Courant number
S	Lundquist number		

## ***Outline of the Thesis***

*Chapter 1* presents the basic principles of Controlled Thermonuclear Fusion, and the approaches to achieve nuclear fusion on Earth. Furthermore, the basic components of the Tokamak, the reactor which will house the fusion reaction, are analyzed. Finally, the chapter ends with a discussion on how the present thesis is related to the Controlled Thermonuclear Fusion. *Chapter 2* introduces briefly the basic concepts of the Electromagnetic and Magnetohydrodynamic theories as well as MHD turbulence. *Chapter 3* presents a first glance in OpenFOAM CFD library. *Chapter 4* introduces the Orszag-Tang vortex flow, which is a benchmark test case for MHD numerical models. Also, the results obtained by the model developed in this thesis are presented and discussed. *Chapter 5 describes* an analytical solution method for the MHD natural convection in an internally heated horizontal shallow cavity. Also, a finite volume numerical model is presented for solving the aforementioned problem and properly validated. The results of the numerical model are compared with the analytical solutions for a range of Rayleigh and Hartmann numbers. Finally, conclusions based on this work are drawn and recommendations for future work are made.

## ***Contribution and novelties of the Thesis***

First of all, useful information about Controlled Thermonuclear Fusion and the ways that scientists use in order to achieve it for the purpose of producing energy are analyzed. In addition, the basic principles of MHD are comprehensively presented.

The contribution of the present Master thesis, however, is to create numerical models in order to simulate MHD natural convection problems in a user-friendly environment that will be easily manipulated considering both low- $R_m$  and full MHD models. Besides, to create an analytical solution for a simple geometry that can be used as a benchmark test in order to validate a low- $R_m$  MHD model.

## CHAPTER 1: CONTROLLED THERMONUCLEAR FUSION

In this chapter, the basic principles of fusion physics are presented since this master thesis deals mainly with the simulation of flows and heat transfer in the blankets of tokamaks.

It is widely known that the world economy runs on fossil fuel. It heats our houses, it moves our cars and produces electricity. However, the world resources of oil, coal and gas are diminishing. If no action is taken, an energy crisis is imminent in the next couple of centuries, maybe decades. Apart from the inevitable fact that we will run out of fuel, the burning coal, oil and gas also has an impact on the environment. The signs of global warming due to carbon dioxide and the accompanying climate change become increasingly more alarming.

Nevertheless, mankind will not give up the present standard of living, so the energy consumption is not expected to be reduced, it will rather be increased. Sources of energy, other than fossils, are therefore needed. Those that are presently available, however, are of very low energy density (solar, wind and bio-energy) or produce long term radioactive waste (nuclear fission). Thermonuclear fusion holds the promise of an abundant supply of energy, without affecting the climate and with minimal short-term radioactive waste.

### 1.1 What is Fusion?

Nuclear fusion is the reaction in which two or more nuclei combine together in order to form a new element with higher atomic number (more protons in the nucleus). The energy released in fusion is related to  $E=mc^2$  (Einstein's famous energy-mass equation). On Earth, the most likely fusion reaction is Deuterium–Tritium reaction. Deuterium and Tritium are both isotopes of Hydrogen.



In this reaction two Hydrogen isotopes, Deuterium and Tritium, fuse resulting in a Helium nucleus and a neutron. The produced energy is divided over the fusion products: the neutron receives kinetic energy of 14.1 MeV, the helium nucleus (also called  $\alpha$ -particle) has energy of 3.5 MeV. Deuterium is largely available in the oceans of the Earth. Tritium is not freely available, but can be produced by a nuclear reaction of Lithium – also widely available – and an energetic neutron. The ‘waste’ of this fusion reaction is Helium: a non-toxic, non-radioactive gas.

### 1.1.1 Fusion on the Earth

In order to achieve fusion on the Earth, we must take into account some serious matters. First of all, the nuclei of Deuterium and Tritium do not fuse spontaneously. Since they both have a positive charge, the repelling Coulomb force prevents their fusion. A sufficiently high kinetic energy of the nuclei is needed to overcome the Coulomb force, see Fig. 1.1. This high kinetic energy is achieved in a gas with temperature  $T$  of about 100 million degrees centigrade. At this level of temperature gases are ionized. We do no longer call them gas, but “*plasma*”. It is common to express temperatures in a plasma with eV, where  $1 \text{ eV} = 12000^\circ\text{C}$ .

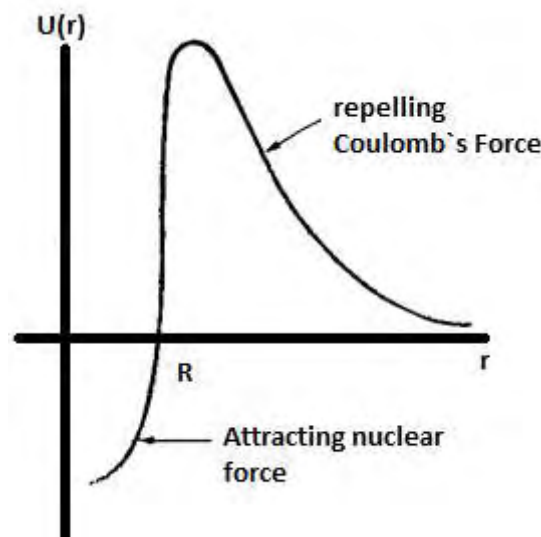


**Fig. 1.1** A sufficiently high kinetic energy of the nuclei is needed to overcome the Coulomb force

Unfortunately, a high temperature is not all that is needed to achieve the fusion of nuclei. In order to have enough collisions between the highly energetic nuclei, the density  $n$  of the particles must be also high enough. A third important parameter is the energy loss. If fusion plasma loses its energy to the outside world faster than it can gain energy from fusion reactions and/or from external heating, then the process will die out. The rate at which plasma loses its energy is given by  $1/\tau_E$ , where  $\tau_E$  is the energy confinement time. A fusion reaction will be self-sustained if the product of the above three parameters – temperature  $T$ , density  $n$  and confinement time  $\tau_E$  is sufficiently high. For the Deuterium – Tritium fusion reaction the following relationship has been proposed:

$$n T \tau_E > 5 \times 10^{21} \text{ keVs/m}^3 \quad (1.2)$$

The above inequality is the so-called *Lawson criterion*. The triple product  $nT\tau_E$  is a figure-of-merit for a fusion reactor: the higher it is the better.

## 1.2 Approaches to Fusion

It has been already mentioned that in order to have a fusion reaction, the charged particles involved must have very large energies and velocities. This leads to the fact that these particles cannot be contained in an ordinary vessel but for a very small amount of time. There are two different lines of research that deal with this problem.

One is based on the rapid compression and heating of a solid fuel pellet through the use of laser or particle beams. In this approach one tries to obtain a sufficient amount of fusion reactions before the material flies apart, hence the name, inertial confinement fusion (ICF).

The other approach, known as magnetic confinement, uses a magnetic field to confine the plasma (see for example Peeters (2008)). Some commonly studied configurations for magnetic confinement are the magnetic mirror, the z-pinch, the stellarator, and the Tokamak.

### 1.2.1 Magnetic Mirror

The magnetic mirror was one of the first confinement devices envisioned. Fig. 1.2 shows the magnetic field geometry of a basic magnetic mirror. The main idea is that the magnetic field is weak at the center and strong at either end. If the electric field is zero, then the kinetic energy of the plasma particles is conserved since the magnetic field does no work. Thus, as the particle moves into a region of stronger magnetic field, the parallel velocity decreases as the perpendicular velocity accounts for more of the particle kinetic energy. In the transition region from the weaker to stronger magnetic field, the magnetic field acquires a radial component. This radial component of the field interacts with the perpendicular velocity of the particle and produces a force that directs the particle back into the region of low field strength. Since the field is “pinched” at both ends, the particle will bounce between the regions of increasing field strength, hence the name “magnetic mirror”.

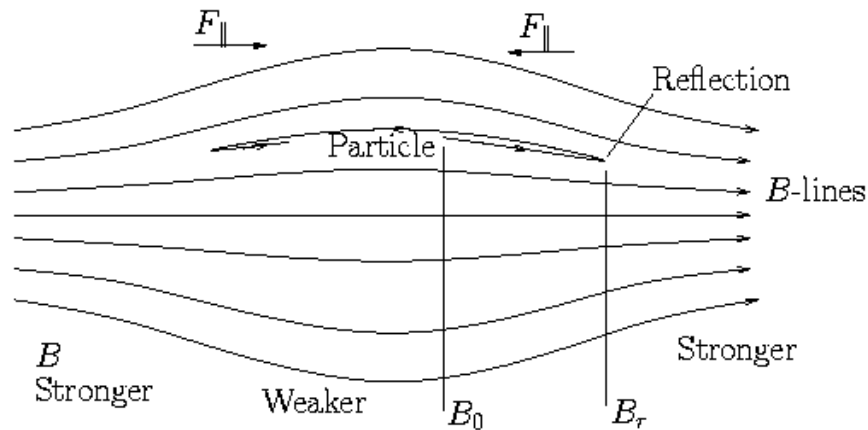


Fig. 1.2 Magnetic mirror plasma confinement configuration (Pasko (2009))

### 1.2.2 Z-Pinch

This configuration relies on the interaction of a current-carrying plasma with the magnetic field it creates. Firstly, there is a current flow through the plasma from the cathode to the anode. The Lorentz force accelerates the plasma along the z-axis and compresses it onto the z-axis in B and C. Because of the acceleration experienced, the plasma has a large particle velocity in addition to current. This creates a more stable z-pinch in D than one without particle flow.

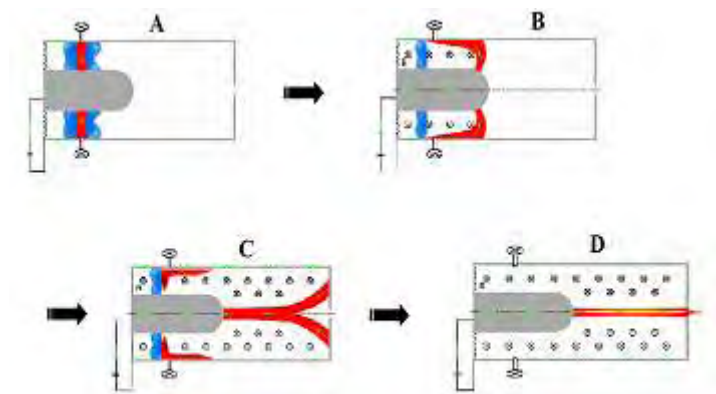
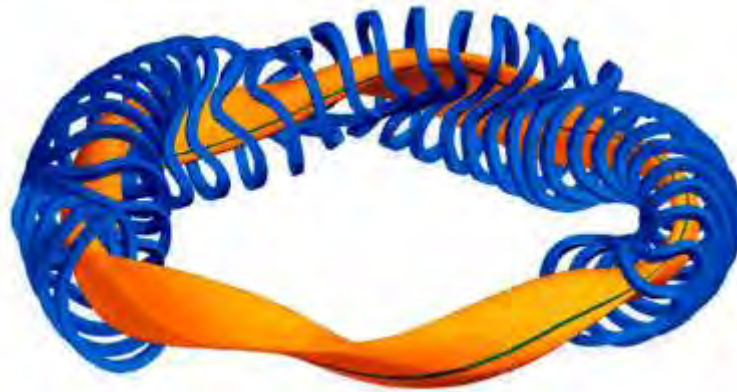


Fig. 1.3 Z-Pinch configuration (Pasko (2009))

### 1.2.3 Stellarator

A stellarator is another promising plasma confinement configuration. It uses toroidal field magnets that are twisted to create the necessary poloidal field without needing plasma current. Fig. 1.4 shows an example of the complex magnet coil structure and the twisting of the toroidal field. The rotational transform angle  $\epsilon$  is, therefore, provided by the externally applied fields. Today, an advanced stellarator

(Wendelstein 7-X) is under construction in Greifswald, Germany in the framework of the European Fusion program. Its magnetic coils are engineering masterpieces, twisted intricately to create the required magnetic field. They are superconducting devices in order to achieve strong magnetic fields that are required to confine the plasma.



*Fig. 1.4 Stellarator configuration (Pasko (2009))*

### 1.2.4 Tokamak

The Tokamak is the most widely studied magnetic confinement configuration. For toroidal plasma confinement, both poloidal ( $B_\theta$ ) and toroidal ( $B_\phi$ ) fields are necessary. The Tokamak is a toroidal configuration with a poloidal field provided by external coils and the plasma current. Fig. 1.5 shows the basic principles of magnetic confinement in a tokamak.

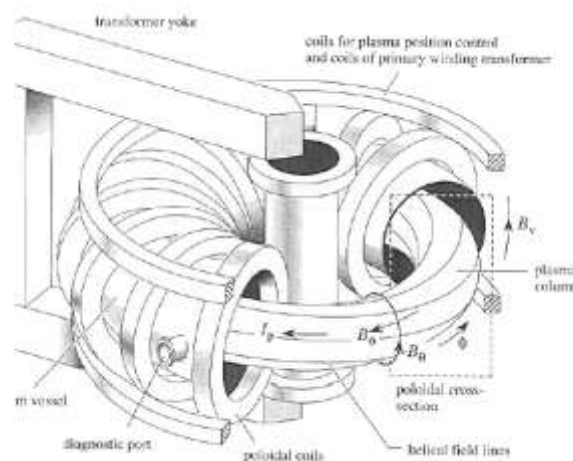


*Fig. 1.5 Tokamak configuration (Pasko (2009))*

The movement of a charged particle parallel to the magnetic field is not restricted. Therefore, in order to confine plasma effectively, the field lines should close in themselves and, hence, they form a toroidal geometry. However, just a torus shaped

vacuum vessel with a toroidal magnetic field is insufficient to confine the plasma. The curvature of the magnetic field causes electrons and ions to drift to the bottom and top of the torus, respectively, resulting in an electric field. This electric field in its turn leads to an outward drift of all particles and, thus, to a loss of confinement. To neutralize this electric field, particles that drifted to the top of the machine should be brought to the bottom and vice versa. This can be achieved by adding a poloidal component to the magnetic field. In a tokamak configuration the poloidal magnetic field is generated by toroidal plasma current. This plasma current is induced by a transformer, using the plasma as the secondary winding. On top of these poloidal and toroidal field components radial and vertical components are added to the magnetic field by external positioning and shaping coils.

### 1.2.5 Basic components of the Tokamak

**Vacuum vessel:** The plasma is contained in a *vacuum vessel*, Fig. 1.6, with vacuum maintained by external pumps. The plasma is created by introducing a small amount of gas, which is then heated by driving a current through it.

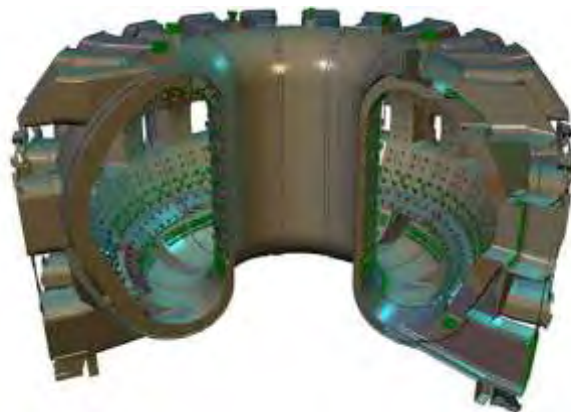


*Fig. 1.6 Vacuum vessel (Diagnostics ITER (2010))*

**Magnets:** The hot plasma is contained by *magnetic fields*, Fig. 1.7, which keep it away from the machine walls. The combination of two sets of magnetic coils – known as toroidal and poloidal field coils – creates a field in both vertical and horizontal directions, acting as a magnetic ‘cage’ to hold and shape the plasma.



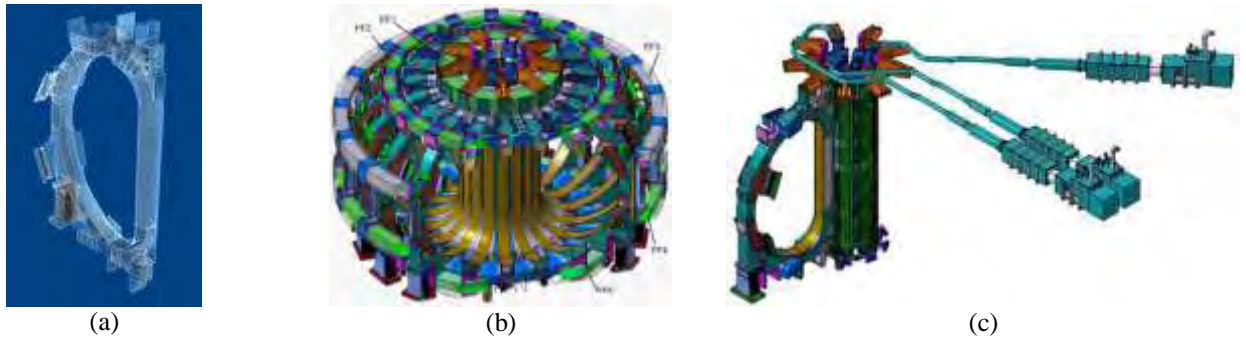


**Fig. 1.7** Magnet systems: a) toroidal field, b) poloidal field, c) central solenoid (Diagnostics ITER (2010))

**Blanket:** A *blanket*, Fig. 1.8, is placed around the fusion plasma (for a review on blanket designs see Ihli et al. (2008)) in the vacuum vessel, surrounding the fusion plasma like a blanket. Within the blanket, the fusion-produced neutrons are slowed down, heat is transferred to a primary coolant, and Tritium is bred from Lithium.

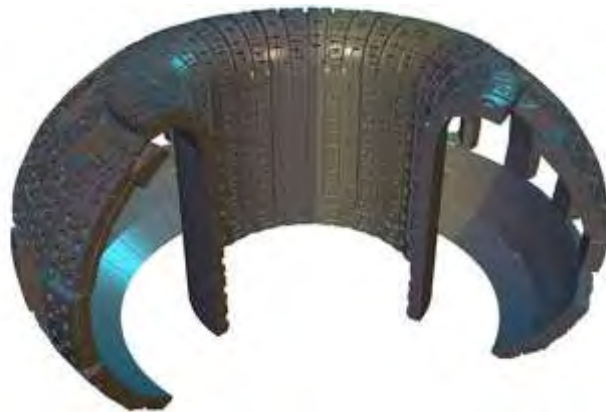


**Fig. 1.8** Blanket (Diagnostics ITER (2010))

**Divertor:** The *divertor*, Fig. 1.9, reduces the impurities in the plasma, removes alpha particle power and Helium ash.

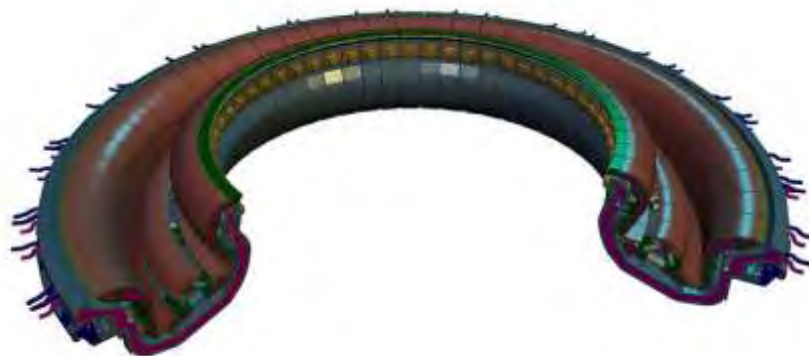


**Fig. 1.9** Divertor (Diagnostics ITER (2010))

**Cryostat:** The *cryostat*, Fig. 1.10, is a single wall cylindrical vessel. It provides the vacuum environment to thermally insulate the superconducting magnets and cold structures.

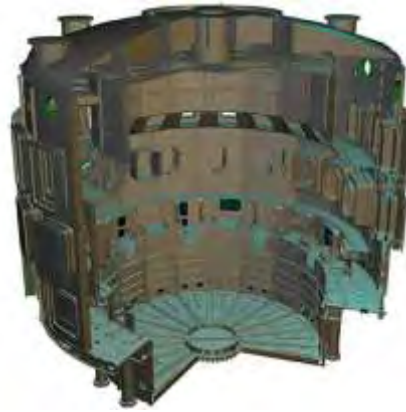


*Fig. 1.10 Cryostat (Diagnostics ITER (2010))*

**Diagnostics:** About fifty (50) individual measuring systems drawn from the full range of modern plasma diagnostic techniques, Fig. 1.11, will be installed on the ITER machine to provide the measurements necessary to control, to evaluate and optimize the plasma performance in ITER and to extend the understanding of plasma physics.

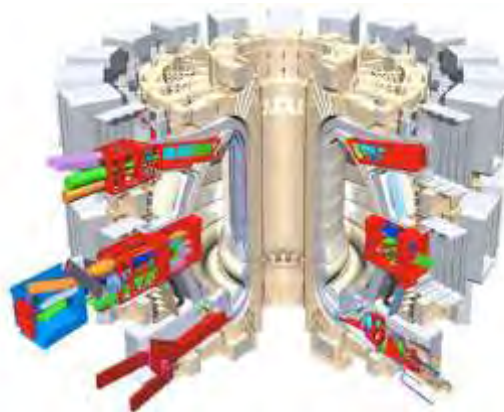


*Fig. 1.11 Diagnostics (Diagnostics ITER (2010))*

### **1.3 Plasma Heating**

In order to create *plasma* for fusion, heating of the fuels to 100-200 million degrees Celsius is required. In the case of JET, this entails putting tens of millions of watts of power – equivalent to about 10,000 fan heaters – into a mere couple of grams of fuel. Analytically, the external heating systems which are currently used and will be applied to ITER are the following ones:

#### **1.3.1 Ohmic Heating or Current Drive**

The coils around the central pole of the torus act as the primary coil for a huge transformer. The plasma itself is the secondary loop and, thus, it has a large current induced in it. This plasma current produces heat, just as a wire warms up when an electric current flows through it. Tokamaks largely rely on plasma current not only for

heating, but also for the poloidal magnetic field. At JET, approximately 1 MW of power is supplied by ohmic heating, which creates plasma currents of up to  $5 \times 10^6$  Amperes.

### 1.3.2 Neutral Beam Heating

High energy particle beams, injected into the plasma, transfer their energy as they collide with the plasma ions, Fig. 1.12a. A particle beam is generated by accelerating ions with high voltage. Since the charged particles cannot penetrate the magnetic field around the plasma, they are turned into neutral atoms just before injection. At JET, about 35 MW of energy (equivalent to 200 Porsche 944 turbos) can be provided by this system.

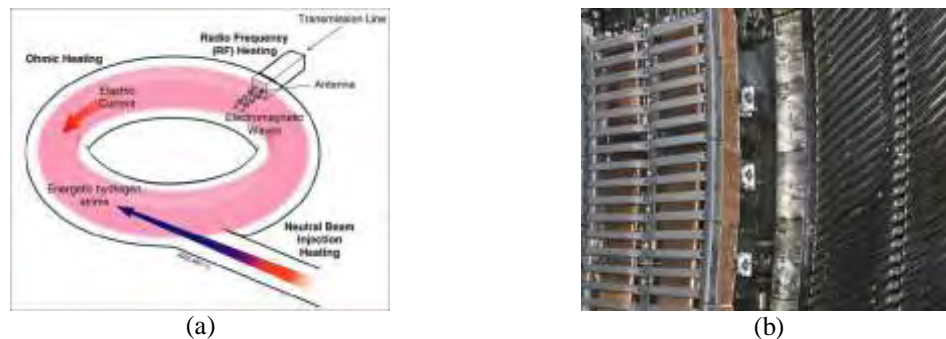


*Fig. 1.12 (a) Neutral beam heating and (b) radio-frequency heating (Diagnostics ITER (2010))*

### 1.3.3 Radio-Frequency Heating

The moving plasma particles spiral along the magnetic field lines with frequencies, typically in the radio-frequency (RF) region of the electromagnetic spectrum. Hence, if one can inject radio waves into the plasma at exactly the right frequency, they will resonate with this rotation, and transfer their energy to the plasma particles, Fig. 1.12b. The plasma particles have different resonance frequencies, depending on their mass and charge and the magnetic field strength at their location. Therefore, the heating can be applied selectively to a predefined group of particles in a selected location in the plasma, by injecting radiation at just the right frequency. This is known as Ion-Cyclotron Resonance Heating (ICRH). JET has a number of ICRH antennae in the vessel wall, which can supply up to 20 MW of power when combined.

### 1.3.4 Lower Hybrid Current Drive

A second RF heating method is called Lower Hybrid Current Drive (LHCD). This involves sending microwaves around the vessel at just the right frequencies that “push” electrons travelling in one particular speed and direction. This effect is used to

add to the plasma current. In JET, the LHCD system generates 10 MW, creating plasma currents of up to  $3 \times 10^6$  Amperes.

## 1.4 The Case of Fusion

A secure and sustainable energy is required in order to maintain our standard of living. Researchers from all over the world are developing a range of environmentally acceptable energy technologies; nuclear fusion being the most promising of them. Our Sun has shown to us a “*new and clear*” energy that must be deeply investigated. In the long term, fusion will provide an option for a large-scale energy that has a low impact on the environment, is safe and with vast and widely distributed fuel resources.

The knowledge that will be gained, as far as the physics of plasmas is concerned, will be beneficial to a wide variety of engineering applications such as high efficiency lighting, manufacturing of semiconductors for home computers, TVs and electronics, flat-panel displays and surface treatment of synthetic cloth for dye adhesion. In particular, plasma is used for surface cleaning, processing of plastics, gas treatment, spraying of materials, microwave generated plasma around a catalyst for removal of  $\text{NO}_x$  and CO from engine exhausts, sterilization of medical tools and spacecrafts (NASA tests of electrostatic ion thruster in large vacuum chamber). Fig. 1.13 illustrates two examples of technological applications of plasma.

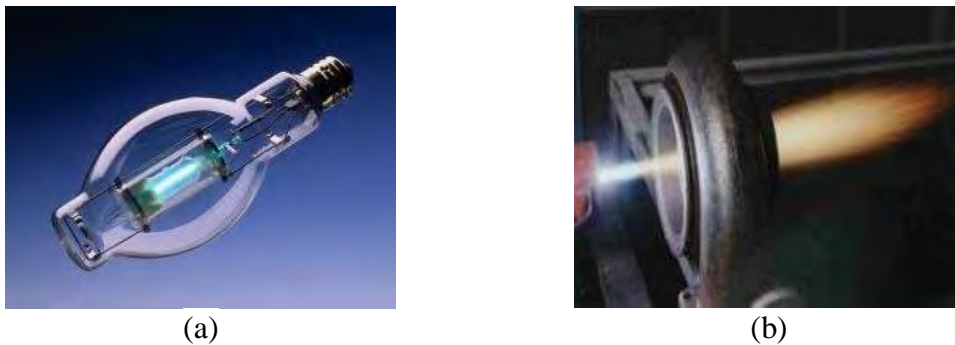


**Fig. 1.13** (a) High efficiency plasma lighting and (b) robotically controlled plasma spraying of high-temperature shielding tiles (Miyamoto (2004))

Furthermore, the research on the materials needed to withstand such high temperatures will be useful in several industrial applications. The vacuum technology will also take advantage from the studies related to rarefied gases which are implemented in the Tokamak vacuum vessel. Moreover, crystal growth techniques and geophysical applications which include magnetohydrodynamic phenomena will profit

from the studies which deal with convection generated by internal heat or by temperature differences of the walls surrounding the electrical conductive fluids.

In conclusion, understanding the physics of the fourth state of matter (i.e. plasma) will help to comprehend matters that are related to Tokamak such as magnetic islands and resistive instabilities. This knowledge will lead to the understanding of space phenomena such as solar flares, the continual steaming of plasma from the Sun surface, known as solar wind and MHD waves. Finally, the use of plasmas as sources for energy-efficient lighting and their role in surface engineering through high speed deposition and etching may seem simple by comparison with fusion and space science. However, these and other commercial applications have laid firm foundations for new plasma technologies.

Regardless of the success or not of the International Thermonuclear Experimental Reactor (ITER) which is being built in Cadarache of France, a promising message is the awareness of the huge ecological damage that has been done to our planet. In order to resolve the current environmental issues, cooperation is needed in both scientific and administrative level.

## 1.5 Fusion versus Fission

Nuclear fusion and nuclear fission are two different types of energy releasing reactions in which energy is produced from high-powered atomic bonds between the particles within the nucleus. The main difference between these two processes is that fission is the splitting of an atom into two or more smaller ones while fusion is the fusing of two or more smaller atoms into a larger one. A comparison between fusion and fission is presented in Table 1.1.

*Table. 1.1 Comparison chart between nuclear fusion and nuclear fission*

	<b>Nuclear Fission</b>	<b>Nuclear Fusion</b>
<b>Definition:</b>	Fission is the splitting of a large atom into two or more smaller ones.	Fusion is the fusing of two or more lighter atoms into a larger one.
<b>Conditions:</b>	Critical mass of the substance and high-speed neutrons are required.	High density, high temperature environment is required.
<b>Energy requirement:</b>	Takes little energy to split two atoms in a fission reaction.	Extremely high energy required to bring two or more protons close enough that nuclear forces overcome their electrostatic repulsion.
<b>Natural occurrence of process:</b>	Fission reaction does not normally occur in nature.	Fusion occurs in stars, such as the sun.
<b>Byproducts of reaction:</b>	Fission produces many highly radioactive particles.	Few radioactive particles are produced by fusion reaction, but if a fission "trigger" is used, radioactive particles will result.
<b>Energy Ratios:</b>	The energy released by fission is a million times greater than in chemical reactions; but lower than by fusion.	The energy released by fusion is three to four times greater than the energy released by fission.
<b>Nuclear weapon:</b>	One class of nuclear weapon is a fission bomb, known as atomic or atom bomb.	One class of nuclear weapon is the hydrogen bomb, using fission to "trigger" fusion.

## 1.6 Relation of Present Work to Controlled Thermonuclear Fusion

The heat which is produced inside the plasma by the exothermal nuclear reactions or by Joule heating or by other mechanisms of plasma heating increases the temperature of the Tokamak walls. Thus, there are temperature differences between the interior hot walls and the colder sidewalls of the blanket which contains liquid metals. These temperature differences can later act as a driving force of natural convection flow of the liquid metal. In this way, apart from conduction, heat transfer occurs via natural convection mechanisms. As a consequence, the energy that can be taken away from the blanket in order to heat the steam cycle of an electricity generating power plant is increased.

In addition, the penetration and absorption of neutrons by the fluid contained in the blanket is a significant problem in fusion Tokamak devices. Therefore, the choice of the fluid is an important issue in the fusion technology. Liquid metals are the dominant

fluids in order to achieve good operation fusion blankets. The free neutrons cause an almost uniform distribution of the internal energy of the liquid metal and consequently a raise of its temperature. The solution of the energy equation demonstrates a temperature distribution with lower values near the walls and higher values in the core region of the blanket. Thus, the increase of the neutrons energy causes the split of the vortices formed when a temperature difference exists between the two walls, into smaller vortices.

The liquid metals surround the Tokamak core and experience electromagnetic forces. The usage of liquid metals as fluids for the heat removal for the Tokamak blanket results in interaction with these forces due to their electrical conductivity. The electromagnetic forces which are produced by the strong magnets of the Tokamak decelerate the liquid which is already weak in the case of natural convection. The impact of the magnetic field on the energy absorption by the blanket is a technological issue with great interest for many researchers in nuclear fusion science and technology.

Summarizing, the magnetic field has a significant impact on the heat transfer in the blankets of fusion reactors. Specifically, the fluid motion tends to be suppressed by the electromagnetic forces produced by the magnetic coils surrounding the Tokamak. Thus, the heat removal is reduced and consequently the energy transfer is decreased.

### 2.1 Introduction

Magnetohydrodynamics or MHD deals with the flow of electrically conducting fluids. The most important of these fluids occurring in both nature and the laboratory are ionized gases, called *plasmas*. These have the simultaneous properties of conducting electricity and being electrically charge-neutral on almost all length scales. The field of study of these gases is called *plasma physics*. MHD is the simplest theory of plasma dynamics. Nonetheless, MHD is an indispensable tool in all applications of plasma physics. Even the simplest experiment will not be built unless it has first been analyzed using MHD. The reason is that MHD deals with fundamental force balance concepts that are surprisingly subtle and complex. MHD also provides the vehicle for understanding the basic properties of global structure of magnetized plasmas, how they can sustain themselves, and why they share a number of global properties.

While MHD is the simplest mathematical model of plasma, it is difficult to justify as a valid description of any interesting plasma. Plasmas are made of individual ions and electrons (or separate ion and electron fluids) and are so hot that collisions between particles are relatively rare events. MHD completely ignores both of these issues. However, it is a fact that MHD provides a remarkably accurate description of the low-frequency, long-wavelength dynamics of real plasmas.

Generally speaking, MHD describes the dynamics of a continuum fluid that is capable of conducting an electric current, it can be characterized by a few parameters such as mass density, velocity and pressure, and that its material properties are independent of the physical size of the sample. Thus, plasma looks exactly the same no matter how finely it is subdivided, and the behavior arising from its atomic structure is not considered. This is precisely the approach taken in hydrodynamics, which is one of the most complex and difficult topics in classical physics. MHD is more complex, and even more difficult, primarily as a result of the spatial anisotropy introduced by the magnetic field.

One of the areas where MHD has been useful is in the design and analysis of toroidally confined plasmas, in particular the tokamak configuration. The theory of these toroidal plasmas is extremely well developed mathematically. It is unfortunate that this theory has led to deficiencies that are difficult to resolve while providing few



additional physical insights. One exception is the equilibrium of axially symmetric toroidal plasma, which provides an introduction to the necessary concepts.

## 2.2 Basic concepts on electromagnetic theory

The electromagnetic fields are the electric field,  $\mathbf{E}$ , and the magnetic flux density or magnetic field,  $\mathbf{B}$ . The sources of these fields are the electric charge density,  $\rho_q$ , and the electric current density,  $\mathbf{J}$ . These quantities must satisfy Maxwell's equations:

$$\textit{Faraday's law:} \quad \frac{\partial \mathbf{B}}{\partial t} = -\nabla \times \mathbf{E} \quad (2.1)$$

$$\textit{Ampere's law:} \quad \mu_0 \mathbf{J} = \nabla \times \mathbf{B} - \frac{1}{c^2} \frac{\partial \mathbf{E}}{\partial t} \quad (2.2)$$

$$\textit{Gauss' law:} \quad \nabla \cdot \mathbf{E} = \frac{\rho_q}{\epsilon_0} \quad (2.3)$$

$$\textit{No magnetic monopoles:} \quad \nabla \cdot \mathbf{B} = 0 \quad (2.4)$$

These equations are written in MKS units and this convention will be used throughout the text. In these units, the *square of the speed of light* is:

$$c^2 = \frac{1}{\epsilon_0 \mu_0} \quad (2.5)$$

where  $\epsilon_0$  is the *permittivity of free space* and  $\mu_0$  is the *permeability of free space*.

The dynamics of the electromagnetic fields and the fluid are coupled through *Ohm's law*,

$$\mathbf{E}' = \eta \mathbf{J} \quad (2.6)$$

where  $\eta$  is the *electrical resistivity*, which is considered a material property of the fluid, and  $\mathbf{E}'$  is the electric field as seen by a conductor moving with velocity  $\mathbf{V}$ . According to the theory of relativity, this is given by

$$\mathbf{E}' = (\mathbf{E} + \mathbf{V} \times \mathbf{B}) / \sqrt{1 - V^2 / c^2} \quad (2.7)$$

where  $\mathbf{E}$  is the electric field in the stationary frame.

Maxwell's equations and Ohm's law are Lorentz invariant, i.e. they are physically accurate to all orders of  $V^2/c^2$ . However, the fluid equations are Gallilean invariant; they are physically accurate only to  $O(V/c)$ . The two systems of equations are incompatible as presently formulated. Thus, we either need to make the fluid equations relativistic or need to render the Maxwell equations Gallilean invariant. In MHD we

consider only low frequencies, i.e.,  $V^2/c^2 = (\omega L/c)^2 \ll 1$ . Therefore, we seek a form of Maxwell's equations that is only accurate through  $O(V/c)$ .

From Eq. (2.7), when  $V^2/c^2 \ll 1$ , we can write the electric field in the moving frame as

$$\mathbf{E}' = \mathbf{E} + \mathbf{V} \times \mathbf{B} \left( 1 - \frac{1}{2} \frac{V^2}{c^2} + \dots \right) = \mathbf{E} + \mathbf{V} \times \mathbf{B} + O\left(\frac{V^2}{c^2}\right) \quad (2.8)$$

Ohm's law (equation 1.6) then becomes

$$\mathbf{E} + \mathbf{U} \times \mathbf{B} = \eta \mathbf{J} \quad (2.9)$$

which is the proper MHD form. It is sometimes called the *resistive Ohm's law*. When  $\eta = 0$ , it is called the *ideal MHD Ohm's law*. It should be noted that for the ideal MHD, the electric field scales like  $E_0 \sim V_0 B_0$  or  $V_0 \sim E_0/B_0$ .

Now consider Ampere's law expressed in equation (2.2). The ratio of the two terms on the right-hand side is, approximately,

$$\left| \frac{1}{c^2} \frac{\partial \mathbf{E}}{\partial t} \right| / \nabla \times \mathbf{B} \approx \frac{E_0 \omega / c^2}{B_0 / L} \approx \frac{V_0 \omega L}{c^2} \approx \frac{V_0^2}{c^2} \ll 1 \quad (2.10)$$

where we have set  $V_0 \sim \omega L$ . We can, therefore, ignore the second term (the displacement current) compared with the first, and the low-frequency version of Ampere's law becomes then

$$\mu_0 \mathbf{J} = \nabla \times \mathbf{B} \quad (2.11)$$

In Magnetohydrodynamics, this equation *defines* the current density.

Next, when Gauss' law in Eq. (2.3) is combined with the ideal MHD Ohm's law, we have

$$\rho_q = -\varepsilon_0 \nabla \cdot (\mathbf{V} \times \mathbf{B}) \quad (2.12)$$

so that MHD allows for a non-vanishing charge density. This net charge must arise from a difference  $\Delta n$  between the local number densities of positive and negative charges. Then, we can write  $\Delta n/n_0 \sim E_0 \varepsilon_0 / (n_0 L e) \sim \varepsilon_0 V_0 B_0 / (n_0 L e)$ , where  $n_0$  is the average number density of positive and negative charges. Thus, using equation (2.5) to eliminate  $\varepsilon_0$ , we find  $\Delta n$

$$\frac{\Delta n}{n_0} \approx \frac{V_0}{c^2} \frac{B_0^2}{\mu_0 n_0 M} \frac{M}{e B_0} \frac{1}{L} \quad (2.13)$$

where  $M$  is the mass of the individual positively charged particles (ions). The quantity  $V_A = B_0^2 / \mu_0 n_0 M$  as the *Alfven velocity*, and  $\Omega = e B_0 / M$  is the ion gyro-frequency (i.e. the frequency at which the individual ions orbit the magnetic field lines). Then setting  $V_0 \sim V_A$ , we have

$$\frac{\Delta n}{n_0} \approx \frac{V_0^2}{c^2} \frac{V_0}{\omega L} \quad (2.14)$$

Finally, setting  $V_A / \omega L = d_i / L$  (where  $d_i = c / \omega_{pi}$  is the ion skin depth and  $\omega_{pi}^2 = n_0 e^2 / \epsilon_0 M$  is the square of the plasma frequency), we can estimate the size of the excess electric charge as

$$\frac{\Delta n}{n_0} \approx \frac{V_0^2}{c^2} \frac{d_i}{L} \quad (2.15)$$

which is  $\ll V_0^2 / c^2$  since  $d_i / L \ll 1$ . This result is called *quasi-neutrality* and it is a consequence of the low-frequency assumption.

However, the charge density cannot be ignored when  $\Delta n / n_0 \sim V_0 / c$ . This can occur if  $(d_i / L)(V_0 / c) \sim 1$  or, in length scales,  $L \sim (V_0 / c) d_i$ . If we estimate  $V \approx V_{thi} \approx (T / M)^{1/2}$ , then  $L \approx (\epsilon_0 T / n_0 e^2)^{1/2} = \lambda_D$ , the *Debye length*. Calculations using the Gauss law and the Boltzmann distribution law ( $n \sim \exp(-U / KT)$ ), where  $U$  is the potential energy) show that at large distances from the charge,  $q$ , the potential decreases exponentially and the electric field is high only in the sphere of radius of order  $\lambda_D$  around the charge  $q$ . This is assumed to be much smaller than any macroscopic scale length. Debye was the first to introduce this characteristic length in his study of strong electrolytes and later on this concept was applied to plasma physics.

The virtual vanishing of the electric charge density does not imply that the electrostatic field vanishes. In steady state ( $\partial / \partial t = 0$ ), Faraday's law requires  $\nabla \times \mathbf{E} = 0$  or  $\mathbf{E} = -\nabla \phi$ , and so the electric field is *completely electrostatic*, and can be large. Instead, regions of smooth field (where  $\nabla \cdot \mathbf{E} \approx 0$ ) are "patched together" across layers with finite charge density and thickness that is vanishingly small, i.e.  $O(\lambda_D)$ . This reminds of (although not completely analogous) the role of shock waves in hydrodynamics.

Finally, it can be shown that the ratio of the electric force to the Lorentz force is

$$\frac{\rho_q \mathbf{E}}{|\mathbf{J} \times \mathbf{B}|} = \frac{V^2}{c^2} \ll 1 \quad (2.16)$$

so that it can be dropped from the equation of motion. The charge density, therefore, never enters the MHD equations. However, if someone ever wants to know what it is, all they have to do is compute  $\rho_q = -\varepsilon_0 \nabla \cdot (\mathbf{V} \times \mathbf{B})$  at least in ideal MHD.

In Eulerian form, the final equations of the MHD model are

$$\text{Continuity equation:} \quad \frac{\partial \rho}{\partial t} + \nabla \rho \cdot \mathbf{V} = 0 \quad (2.17)$$

$$\text{Momentum equation} \quad \rho \left( \frac{\partial \mathbf{V}}{\partial t} + \mathbf{V} \cdot \nabla \mathbf{V} \right) = -\nabla p - \mathbf{J} \times \mathbf{B} + \mu \nabla^2 \mathbf{V} \quad (2.18)$$

*Energy balance:*

$$\underbrace{\rho C_p \left( \frac{\partial T}{\partial t} + \mathbf{V} \cdot \nabla T \right)}_{\text{Rate of change of internal energy}} = \underbrace{k \nabla^2 T}_{\text{Rate of change of heat conduction}} + \underbrace{\underbrace{\ddot{\tau} : \nabla \mathbf{V}}_{\text{Rate of change of work of viscous stresses (viscous dissipation)}}}_{\text{Rate of change of work of viscous stresses (viscous dissipation)}} - \underbrace{p \nabla \cdot \mathbf{V}}_{\text{Rate of compression work}} + \underbrace{\frac{J^2}{\sigma}}_{\text{Joule heating}} \quad (2.19)$$

Note that for incompressible fluids, the term corresponding to the compression work vanishes since velocity is considered to be solenoidal ( $\nabla \cdot \mathbf{V} = 0$ ).

Introducing the Fourier law of heat conduction:

$$\mathbf{q} = -k \nabla T \quad (2.20)$$

we get:

$$\rho \frac{De}{Dt} = k \nabla^2 T - p \nabla \cdot \mathbf{V} + \ddot{\tau} : \nabla \mathbf{V} + \frac{J^2}{\sigma} \quad (2.21)$$

Where  $D/Dt$  is the material derivative which is equal to  $\frac{\partial}{\partial t} + \mathbf{V} \cdot \nabla$

The equations for the electromagnetic fields are:

$$\frac{\partial \mathbf{B}}{\partial t} = -\nabla \times \mathbf{E} \quad (2.22)$$

$$\nabla \times \mathbf{B} = \mu_0 \mathbf{J} \quad (2.23)$$

Ohm's law, which couples the fluid and the electromagnetic fields:

$$\mathbf{E} + \mathbf{V} \times \mathbf{B} = \eta \mathbf{J} \quad (2.24)$$

The law of *conservation of energy* (h) is obtained by adding the rate of change of internal ( $\rho e$ ), kinetic ( $\frac{1}{2}\rho v^2$ ) and magnetic energy ( $\frac{B^2}{2\mu_0}$ ). Thus, we obtain:

$$\frac{\partial h}{\partial t} = -\nabla \cdot \left\{ \left[ \left( \rho e + \frac{1}{2}\rho v^2 \right) \mathbf{J} + \mathbf{P} \right] \cdot \mathbf{V} + \frac{1}{\mu_0} \mathbf{E} \times \mathbf{B} + q \right\} \quad (2.25)$$

where  $\rho$  is the number density,  $\mathbf{V}$  is the bulk velocity,  $\mathbf{B}$  is the magnetic field strength,  $\mathbf{E}$  is the electric field strength,  $p$  is the pressure,  $\mu$  is the viscosity,  $\eta = 1/\mu_0\sigma$  is the resistivity,  $\mu_0$  is the permeability,  $\sigma$  is the electrical conductivity and  $\mathbf{J}$  is the current density.

### 2.3 Ideal MHD

In ideal MHD, the medium is considered to be ideal with no thermal conductivity, and no viscosity. This is a highly idealized situation, not attainable in nature. However, it turns out that ideal MHD describes to a remarkably good approximation many of the dynamical properties of hot, strongly magnetized plasmas. This is primarily because most hot plasmas are excellent (although not perfect) conductors of electricity. Ideal MHD is thus of considerable interest.

When  $\mathbf{V} \times \mathbf{B}$  is greater than  $\eta \mathbf{J}$  or

$$R_m = \frac{vB}{\eta J} = \frac{\mu_0 v L}{\eta} \gg 1 \quad (2.26)$$

Ohm's law becomes

$$\mathbf{E} + \mathbf{V} \times \mathbf{B} = 0 \quad (2.27)$$

Here  $L$  is the characteristic length of the system and  $R_m$  is called the magnetic Reynolds number which is an analog to the Reynolds number  $R = uL/\nu$  (where  $\nu$  is the kinematic viscosity and  $u$  is the velocity) in neutral fluid dynamics. Usually,  $v = v_A$ , the Alfvén velocity which has already been mentioned. Then, by ignoring the viscous forces and the charge  $q$  and setting  $\eta = 0$  the model is simplified as follows:

$$\frac{\partial \rho}{\partial t} + \nabla \rho \cdot \mathbf{V} = 0 \quad (2.28)$$

$$\rho \left( \frac{\partial \mathbf{V}}{\partial t} + \mathbf{V} \cdot \nabla \mathbf{V} \right) = -\nabla p - \frac{1}{\mu_0} (\nabla \times \mathbf{B}) \times \mathbf{B} \quad (2.29)$$

$$\frac{\partial p}{\partial t} = -\mathbf{V} \cdot \nabla p - \Gamma p \nabla \cdot \mathbf{V} \quad (2.30)$$

$$\frac{\partial \mathbf{B}}{\partial t} = -\nabla \times (\mathbf{V} \times \mathbf{B}) \quad (2.31)$$

$$\mathbf{E} = -\mathbf{V} \times \mathbf{B} \quad (2.32)$$

Let us now derive the most important property of ideal MHD. Consider a closed curve  $C$  within the fluid, and let every point on the curve be moving with the local fluid velocity. We say that  $C$  is co-moving with the fluid, in the Lagrangian sense. Let  $S$  be a surface bounded by  $C$ . Then defining

$$\Psi = \int_S \mathbf{B} \cdot d\mathbf{S} \quad (2.33)$$

as the flux through  $S$ , we ask how  $\Psi$  changes as  $C$  moves with the fluid. The differential  $d\Psi$  consists of two parts:

1.  $d\Psi_1$ , due to the changes in  $\mathbf{B}$  with  $C$  (and  $S$ ) held fixed, i.e.,

$$\left( \frac{\partial \Psi}{\partial t} \right)_1 = \int_S \frac{\partial \mathbf{B}}{\partial t} \cdot d\mathbf{S} = -\int_S \nabla \times \mathbf{E} \cdot d\mathbf{S} = -\oint_C \mathbf{E} \cdot d\mathbf{l} \quad (2.34)$$

2.  $d\Psi_2$ , the amount of magnetic flux swept out by  $C$  as it moves with the fluid which is calculated as follows: As  $S$  moves about, each line element moves a distance  $\mathbf{V}dt$ , and sweeps out a lateral area  $d\mathbf{S} = \mathbf{V}dt \times d\mathbf{l}$ . This is shown in Fig. 2.1.

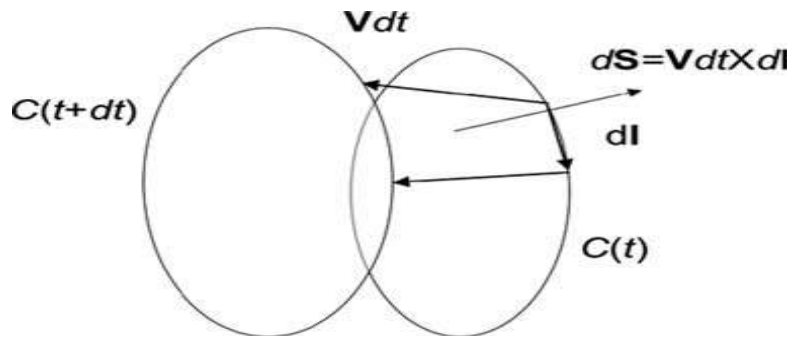


**Fig. 2.1** Computing the magnetic flux through a volume element swept out by a surface moving with the fluid (Schnack (2009))

The flux through this area is  $d\Psi_2 = \mathbf{B} \cdot d\mathbf{S} = \mathbf{B} \cdot \mathbf{V} \times d\mathbf{l}dt$ , so that

$$\left( \frac{\partial \Psi}{\partial t} \right)_2 = \oint_C \mathbf{B} \cdot \mathbf{V} \times d\mathbf{l} = -\oint_C \mathbf{V} \times \mathbf{B} \cdot d\mathbf{l} \quad (2.35)$$

The total rate of change of flux through  $C$  is then

$$\frac{\partial \Psi}{\partial t} = \left( \frac{\partial \Psi}{\partial t} \right)_1 + \left( \frac{\partial \Psi}{\partial t} \right)_2 = -\oint_C \mathbf{E} \cdot d\mathbf{l} - \oint_C \mathbf{V} \times \mathbf{B} \cdot d\mathbf{l} = -\oint_C (\mathbf{E} + \mathbf{V} \times \mathbf{B}) \cdot d\mathbf{l} \quad (2.36)$$

However, in ideal MHD,  $\mathbf{E} + \mathbf{V} \times \mathbf{B} = 0$ , so that  $d\Psi/dt = 0$ , and thus we conclude that in ideal MHD, *the magnetic flux through any co-moving closed circuit remains constant*. This important result is called the *frozen flux condition*. It means that the magnetic field lines can be thought of as being *attached* to the fluid (and *vice versa*); the fluid cannot move *across* the magnetic field. However, the fluid is free to slide *along*  $\mathbf{B}$ . A perpendicular velocity will induce an electric field through  $\mathbf{E} = -\mathbf{V} \times \mathbf{B}$ . This will cause a change in  $\mathbf{B}$  through Faraday's law that is sufficient to make the field lines appear to move with the fluid. If there are both electric and magnetic fields, there will be a perpendicular velocity, which is sometimes called the *MHD velocity*, given by

$$V_{\perp} = \frac{\mathbf{E} \times \mathbf{B}}{B^2} \quad (2.37)$$

## 2.4 Resistive MHD

We have proved above that the change in magnetic flux passing through a co-moving closed circuit is

$$\frac{\partial \Psi}{\partial t} = - \oint_c (\mathbf{E} + \mathbf{V} \times \mathbf{B}) \cdot d\mathbf{l} \quad (2.38)$$

Since in ideal MHD we have  $\mathbf{E} + \mathbf{V} \times \mathbf{B} = 0$ , it follows that  $d\Psi/dt = 0$ , and we say that the flux is “frozen in” the fluid. Nevertheless, in the more general MHD case when the fluid is no longer a perfect electrical conductor,  $\mathbf{E} + \mathbf{V} \times \mathbf{B} = \eta \mathbf{J}$  and

$$\frac{\partial \Psi}{\partial t} = \int_c \eta \mathbf{J} \cdot d\mathbf{l} \neq 0 \quad (2.39)$$

so that the frozen flux condition no longer applies in *resistive MHD*. In this case, the fluid can “move” separately from the field and the field lines can “slip across” the fluid. This can be an important effect, even when the resistivity is very small. In resistive MHD, the combination of Faraday's law and Ohm's law becomes

$$\frac{\partial \mathbf{B}}{\partial t} = \underbrace{\nabla \times (\mathbf{V} \times \mathbf{B})}_{\text{Ideal MHD}} - \underbrace{\nabla \times \left( \frac{\eta}{\mu_0} \nabla \times \mathbf{B} \right)}_{\text{Resistive modification}} \quad (2.40)$$

The first term is just ideal MHD. The second term is a modification introduced when the electrical conductivity  $\sigma = 1/\eta$  is finite (rather than infinite). When  $\eta$  is constant, the last term can be written as

$$\nabla \times \left( \frac{\eta}{\mu_0} \nabla \times \mathbf{B} \right) = \frac{\eta}{\mu_0} \nabla \times \nabla \times \mathbf{B} = \frac{\eta}{\mu_0} \left[ \nabla (\nabla \cdot \mathbf{B}) - \nabla^2 \mathbf{B} \right] = -\frac{\eta}{\mu_0} \nabla^2 \mathbf{B} \quad (2.41)$$

So that Eq. (2.36) becomes

$$\frac{\partial \mathbf{B}}{\partial t} = \nabla \times (\mathbf{V} \times \mathbf{B}) + \frac{\eta}{\mu_0} \nabla^2 \mathbf{B} \quad (2.42)$$

The effect of resistivity is to introduce *diffusion* of the magnetic field, with a diffusion coefficient  $D_\eta = \eta/\mu_0$  (m<sup>2</sup>/s in SI units). The characteristic time-scale for the diffusion of structures with length scale  $L$  is

$$\tau_R = L^2 / D_\eta = \frac{\mu_0 L^2}{\eta} \quad (1.43)$$

which is called the *resistive diffusion time*.

On the other hand, the characteristic time-scale associated with *ideal* ( $\eta = 0$ ) MHD processes is the *Alfven time*

$$\tau_A = L / V_A \quad (2.44)$$

The ratio of the resistive and ideal MHD time scales is called the *magnetic Reynolds number* or as it is usually referred to in plasma physics as the *Lundquist number*.

$$S = \tau_R / \tau_A \quad (2.45)$$

It turns out that for many (but not all) MHD situations,  $S \gg 1$ . The Lundquist number plays an important role in describing the dynamics of hot magnetized plasmas. For high temperature laboratory plasmas,  $S$  is typically  $10^6$  -  $10^8$  and several orders of magnitude greater still for astrophysical plasmas.

Although the plasma relevant to fusion can normally be treated as being collisionless, the collisional resistivity, however small, often plays a crucial role in the macroscopic processes of plasma. In fact, the convection term vanishes somewhere in the plasma and there will be a local region in which the diffusion term, however small, comes into play. Thus, the significance of large  $S$  is not that resistivity is entirely negligible but rather that, compared with  $L_H$  (the hydrodynamic length scale), the length scale of the region in which it need be considered is very small. In other words, although ideal MHD may be valid for most of the plasma, there can be narrow boundary layers such as *current sheets*, in which we must apply resistive MHD. Within such



regions *plasma relaxation* involves the *reconnection* of magnetic field lines, generally reducing a complex field topology to one with simpler connectivity, thereby enabling the system to arrive at a lower energy state. These topological changes in the magnetic field take place on a time-scale between  $\tau_A$  and  $\tau_R$ . Such fast reconnections taking place at current sheets are vital for violent events such as solar flares and major disruptions in tokamaks. Indeed, the resistivity causes a “*reconnection*” of different magnetic field lines, which never happens in an ideal MHD plasma because of the already mentioned “*frozen-in*” condition of the fluid.

To understand how magnetic field changes occur in real plasmas with small but finite resistivity let us consider the simplest model of a slab plasma, as in Fig. 2.2, whose magnetic field is slowly varying with  $y$ , decreasing in magnitude, reversing sign, and then increasing again. The plane ( $y=0$ ) in which  $\mathbf{B}=0$  is called the *neutral sheet*. If the field lines define the  $z$ -axis, the current  $\mathbf{j}$  is parallel to the  $x$ -axis and the Lorentz force  $\mathbf{j} \times \mathbf{B}$  acts downwards for  $y > 0$  and upwards for  $y < 0$ . In ideal MHD, either these forces are opposed by a plasma pressure gradient maintaining equilibrium or plasma and field lines will move together towards the  $y=0$  plane until these forces are in balance. However, with the introduction of finite resistivity, no matter how small, the field is no longer frozen into the plasma and slippage of field lines across the plasma allows breaking of the field lines with reconnection to line of opposite polarity as shown in Fig.2.2.

The above may happen at various points along the neutral lines (see Fig.2.3), giving rise to so-called *magnetic islands*, i.e. sets of nested magnetic surfaces each with its own magnetic axis. The dashed line in Fig. 2.3 is the *separatrix* marking the boundary between the regions of different field topology. The topological change takes place because the magnetic energy associated with the magnetic islands is less than that in the original, MHD configuration. We can readily imagine this if we think of the field lines as stretched strings; the tension in them has been reduced because breaking and reconnecting allows them to contract around the island axes. The stored energy (potential) in the final configuration is less than in the original one. The null points of the magnetic define O-points, at the axes of the magnetic islands, and X-points, at the intersections of the *separatrix*.

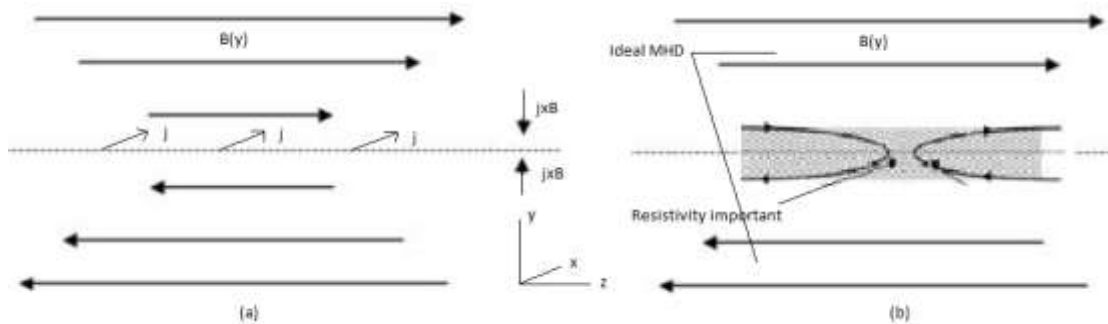


**Fig. 2.2** Magnetic reconnection in a slab plasma (Schnack (2009))

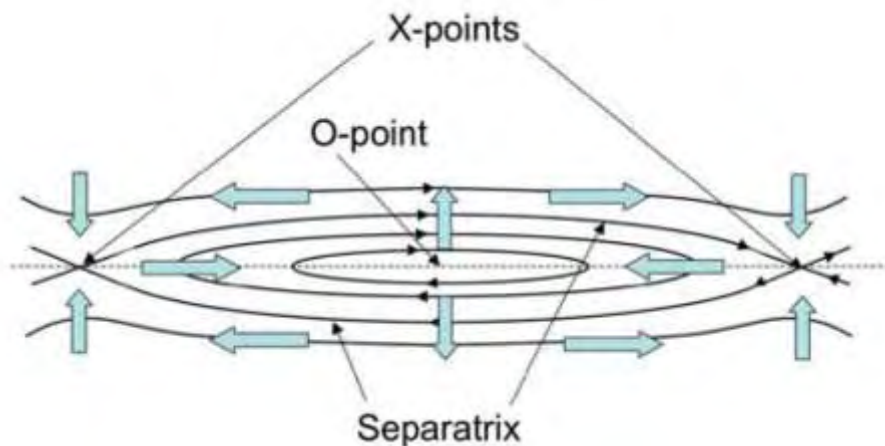


**Fig.2.3** Flow pattern in the vicinity of a magnetic island (Schnack (2009))

To sum up, the magnetic island has a *separatrix*, which separates field lines of different topologies (open outside and closed inside the island). The magnetic reconnection occurs at the *X-points*. The center of the island is called the *O-point*. All the above features are illustrated in Fig. 2.3.

Magnetic reconnection can occur as a *steady-state process* in which two opposite directed magnetic fields are pushed together by external means. The reconnection then occurs at a constant rate  $\gamma$ . Magnetic reconnection can also occur spontaneously as a *resistive instability*. The magnetic island then grows at a rate  $e^{\gamma t}$ .

Magnetic reconnection is an important phenomenon because ideal MHD constraints trap energy in the magnetic field. Resistive MHD relaxes those constraints and allows a new source of free energy to drive instabilities. Magnetic reconnection is thought by some to be responsible for “energizing the universe” by means of solar and stellar flares, heating of diffuse plasmas, the formation and evolution of astrophysical jets. Unfortunately, for most cases of interest  $S \gg 1$  (for a tokamak  $S \approx 10^{7-10}$ , and it is

even larger in astrophysical settings). Since  $\gamma \rightarrow 0$ , when  $\eta \rightarrow 0$ , we expect (and we find) that  $\gamma \approx S^{-\alpha}$  with  $0 \leq \alpha \leq 1$ .

It is difficult to account for the observed rate of energy release with these slow growth rates. The quest for a cause of “fast” magnetic reconnection has been alive for five decades, and it still goes on. Undoubtedly, it will continue for many more years in the future. Further analysis is beyond the scope of this thesis, but for a complete discussion on these phenomena the reader is referred to the work of Sweet and Parker (Sweet-Parker model for steady reconnection) and Petschek’s model (see at Schnack (2009)). Finally, the instabilities driven by resistivity can be found in any plasma physics book such as those by Boyd & Danderson (2003) and Schnack (2009).

Today, one still relies primarily on resistive MHD to study the global dynamics of plasmas, with appeals to artificially enhanced “anomalous” resistivity to obtain sufficient rates of reconnection.

## 2.5 MHD turbulence

Let us suppose that we set up an experiment in which we can control all the *mean* parameters. An example might be steady flow through a pipe, where we can control the mean velocity. Now insert a probe or some kind of measuring device, at a fixed location far from the boundaries and measure the flow velocity as a function of time. The result of this measurement might look something like Fig. 2.4. All measurements are taken under identical conditions. Nevertheless, the results of the measurements at different times are not the same. Instead, we find that the velocity takes on *random values*. Although the mean velocity is determined precisely by the controllable conditions, the random values are not. Fluctuating motions of this kind are said to be *turbulent*. The random fluctuations in  $V$  have a probability distribution with a mean value  $V_{av}$ , as shown in Fig. 2.4.

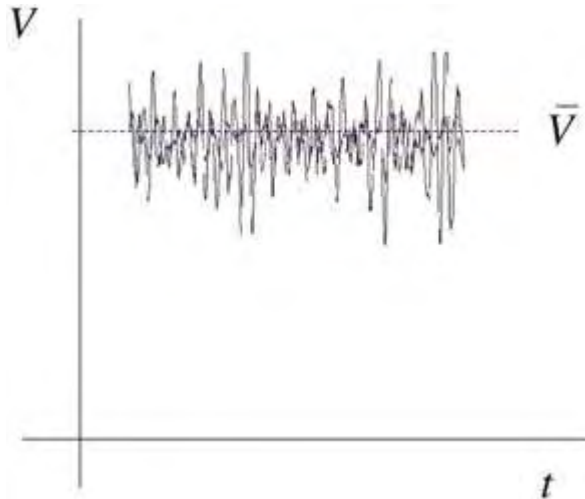


**Fig. 2.4** Measurement of a fluctuating velocity field (Schnack (2009))

The function  $P(V)$  is called the *probability distribution function* (PDF). If the fluctuations are truly random, the PDF is *Gaussian*. If the PDF and  $V_{av}$  are independent of the position, the turbulence is said to be *homogeneous*. If the PDF is independent of arbitrary rotations of the system, and of reflections about any plane, the turbulence is said to be *isotropic*. Isotropic turbulence has no preferred direction in space. If the random flow looks the same on all spatial scales, the turbulence is said to be *self-similar* (or *scale invariant*). A rigorous theoretical study of turbulence requires a statistical description.

Now, let us initialize the system with long wavelength, steady, smooth conditions. For example, consider the stirring of a perfect cup of coffee with a perfect spoon. The perfect cup is an infinitely long cylinder of radius,  $a$ , with no boundary perturbations, and the perfect spoon excites only a single circular eddy with velocity  $V_{stir}$  and radius  $a$ . The stirring is continued until the system reaches steady state. Then, the velocity is measured at the probe position. The result looks like in Fig. 2.4, with  $V_{av} = V_{stir}$ . The question is how did these small-scale random fluctuations come about if only the longest wavelength is excited by the stirring of the spoon? The answer is that the fluctuations arise because of the *non-linearities* in the fluid motion as reflected in the flow equations. In the absence of pressure forces, and with constant density, the evolution of the velocity is governed by the equation of motion

$$\frac{\partial \mathbf{V}}{\partial t} + \mathbf{V} \cdot \nabla \mathbf{V} = \nu \nabla^2 \mathbf{V} \quad (2.46)$$

The second term on the left-hand side is nonlinear, containing the product of the velocity and its derivative.

At each step, new eddies with shorter wavelength and smaller amplitude are generated. If continued indefinitely, eddies with arbitrarily small wavelengths (large wave numbers) will be generated. This is inevitable and accounts for the small-scale random velocities that occur in the measurements. Since the amplitude of the small eddies decreases with wave number  $k$ , a plot of  $\varepsilon(k)$ , the energy contained in an eddy with wave number  $k$ , versus  $k$  might look like in Fig. 2.5.

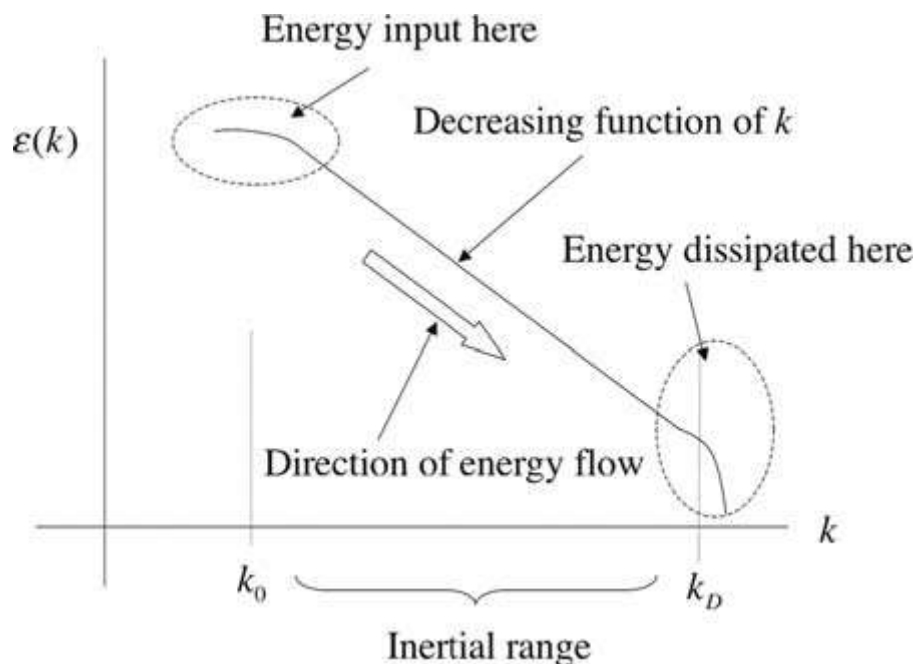


**Fig. 2.5** Illustration of the cascade of energy from large to small wavelength as a result of nonlinear mode coupling (Schnack (2009))

Kinetic energy is continually fed at a specific wave number  $k_0$ . It is continually spread to higher and higher  $k$  (smaller and smaller eddies) as a result of the nonlinear interactions described above, called a *cascade*. The cascade of energy to higher  $k$  will continue indefinitely unless other processes intervene. The cascade will be unable to continue when the magnitude of the viscous term becomes comparable with the nonlinear term.

The qualitative picture of steady-state turbulence is therefore as follows. Kinetic energy is continuously input at a small wave number,  $k_0$ . As a result of nonlinearities in the governing dynamical equations, this energy cascades to higher and higher wave number, producing eddies with smaller and smaller amplitude. The cascade will cease when  $k$  approaches  $k_D$ , where dissipation can compete with the nonlinearity. All the

energy that is input at  $k \approx k_0$  is dissipated near  $k \approx k_D$ ; this is called the *dissipation range*. The energy simply moves through the intervening wave numbers. The range  $k_0 < k < k_D$  is called the *inertial range*, for it is dominated by  $dV/dt \approx 0$  (the Lagrangian derivative) and dissipation plays no role. We may, therefore, expect the kinetic energy spectrum to look like as sketched in Fig. 2.5. This plot is said to display the *spectrum of turbulence*.

### 2.5.1 Relation of Turbulence to MHD

Now, how are all these related to MHD? There is no definitive answer, although there are many ideas. MHD turbulence certainly may have different properties than hydrodynamic turbulence. For one thing, the magnetic field provides a *preferred direction* in space, so the turbulence will no longer be isotropic. Motions, or eddies, tend to stretch out along field lines, so that  $k_{\perp} \gg k_{\parallel}$ , as sketched in Fig. 2.6.

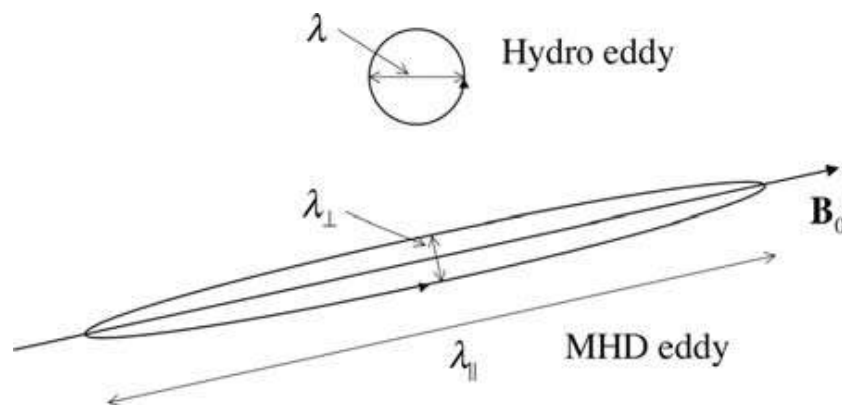


**Fig. 2.6** In MHD turbulence eddies tend to elongate along the magnetic field (Schnack (2009))

When the mean field is much larger than the fluctuating field, we might expect the turbulence to be approximately two-dimensional on the plane perpendicular to the vector  $\mathbf{B}$ . MHD turbulence does not appear to be self-similar. In MHD we know that eddies are stretched out along the magnetic field and that this anisotropy increases at smaller scales. Thus, the small scales are more “stretched” than the large scales, and the stretching changes with increasing wave number  $k$ . This is manifested in the structure of the current density  $\mathbf{J}$  at small scales. At these scales, the magnetic flux tends to get “squeezed” by eddies to form long thin current filaments. An example of filamentary spatial structures in MHD turbulence is illustrated in Fig. 2.7. We might expect the current filaments in MHD turbulence to look like in this figure. Furthermore, someone could distinguish the coherent structures.

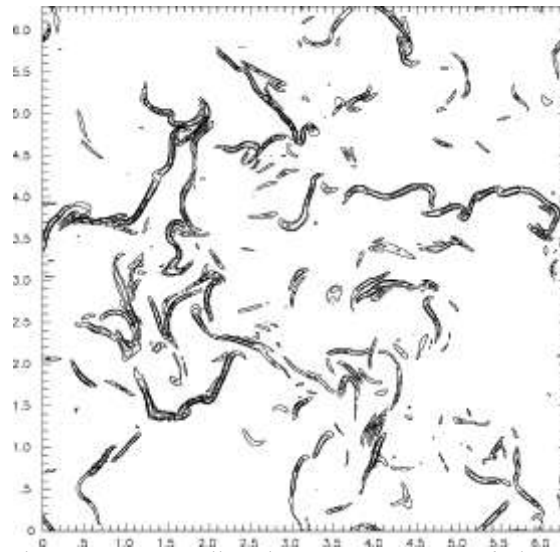


**Fig. 2.7** The spatial structure at small scales in intermittent turbulence (Schnack (2009))

For self-similar turbulence the variation would be random. However, in MHD the current appears as semi-discrete sheets or spikes. The energy is, therefore, dissipated in discrete reconnection events at small scales, rather than as a continuous process. The turbulence is said to be *intermittent*. The structures at small scales are not space filling, and the turbulence at this scale ceases to be self-similar.

Numerical simulations indicate that the MHD fluid tends to form into small regions where the velocity and the magnetic field are either positively or negatively aligned. The details of this state depend on the amount of energy and cross-helicity in the initial conditions (see at Schnack (2009)).

The approach in this section has been theoretical. It only becomes real physics when it is compared with what occurs in nature. This can be determined from experiment, as in the case of hydrodynamic flow in a pipe or a wind tunnel or from observations of astrophysical plasmas, such as the interstellar medium or the solar wind. The most striking thing about these data is that they display the general form of the Kolmogorov spectrum, i.e. an input range, an inertial range, and a dissipation range, as sketched in Fig. 2.6.

While the power law in the inertial range often appears to be close to the Kolmogorov value ( $-5/3$ ), closer examination of data for both hydrodynamic and MHD turbulence shows that small deviations from the value  $-5/3$  exist and are real. This deviation is often attributed to the intermittency or the lack of self-similarity at small scales, as discussed above. A clear example of this phenomenon in MHD turbulence is

demonstrated in Fig. 2.8, which shows the spectrum of the fluctuating magnetic energy in a region of the Earth's magnetosphere as measured in situ by a constellation of satellites. The horizontal axis is the wave number normalized to the ion Larmor radius. The separation between the satellites was about 100 km. The exponent for the power law in the inertial range is approximately  $-8/3$ , much steeper than Kolmogorov's.

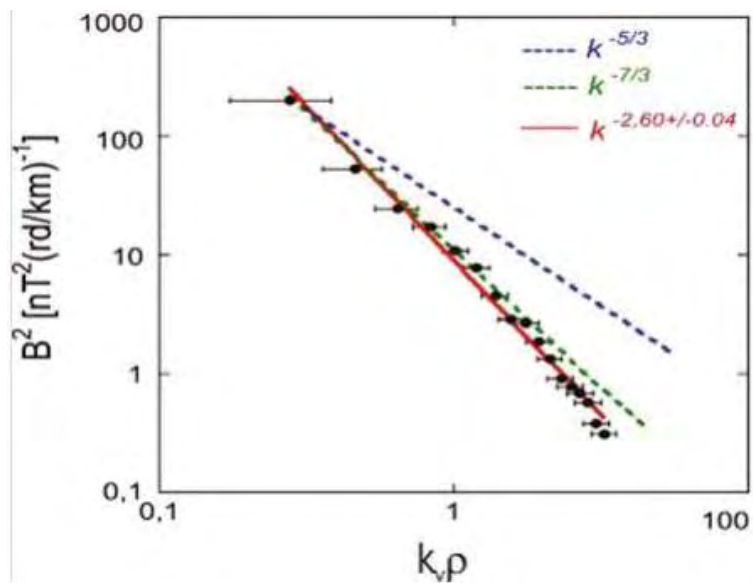


*Fig. 2.8 Spectrum of magnetic energy in a Earth's magnetosphere as measured by the CLUSTER mission (Schnack (2009))*

MHD turbulence is a fascinating physical phenomenon that has been attracting the interest of experimenters and theoreticians for many decades. Nevertheless, it still defies deep understanding in spite of considerable progress that has been made.



## CHAPTER 3: MAIN CHARACTERISTICS OF OPENFOAM

### 3.1 History

OpenFOAM (Open Field Operation And Manipulation, see Weller (2004a,b)) started as FOAM around 1993 at Imperial College, London, as a collaboration of Weller and Jasak, who started working on his PhD thesis at that time, Jasak (1996). The motivation to develop CFD software from scratch was mainly dissatisfaction with codes in FORTRAN and the goal to create something reusable by others. For a few years, FOAM was developed as closed-source commercial software, before becoming open source in December 2004 with OpenFOAM 1.0. Since then, six major releases were launched; the latest version is OpenFOAM 2.1.1 released in 2012. OpenFOAM is used by a lot of R&D teams in academic institutions and industry.

### 3.2 Features of OpenFOAM

The OpenFOAM CFD Toolbox is a free, open source CFD software package. OpenFOAM has an extensive range of features to solve anything from complex fluid flows involving chemical reactions, turbulence and heat transfer, to solid dynamics and electromagnetics. It includes tools for meshing, notably «snappyHexMesh», a parallelized mesher for complex CAD geometries, and for pre- and post-processing. Almost everything (including meshing, and pre- and post-processing) runs in parallel as standard, enabling users to take full advantage of available computer hardware.

OpenFOAM offers users complete freedom to customize and extend its existing functionality. It is highly modular code in which collections of functionality (e.g. numerical methods, meshing and physical models) are each compiled into their own shared library. Executable applications are then created that are simply linked to the library. OpenFOAM includes over 80 solver applications that simulate specific problems in engineering mechanics and over 170 utility applications that perform pre- and post-processing tasks such as, for example, meshing and data visualization.

### 3.3 Standard Solvers

OpenFOAM is fundamentally a tool for solving partial differential equations rather than a CFD package in the traditional sense. Table 3.1 presents a list of solvers that are available to users.

*Table 3.1: OpenFOAM solver descriptions*

<b>Precompiled solvers</b>	<b>Description</b>
icoFoam	Transient solver for incompressible, laminar flow of Newtonian fluids
laplacianFoam	Solves a simple Laplace equation, e.g. for thermal diffusion in a solid
SonicFoam	Transient solver for transonic/supersonic, laminar or turbulent flow of a compressible gas
bubbleFoam	Solver for a system of 2 incompressible fluid phases with one phase dispersed, e.g. gas bubbles in a liquid
dnsFoam	Direct numerical simulation solver for boxes of isotropic turbulence
nonNewtonianIcoFoam	Transient solver for incompressible, laminar flow of non-Newtonian fluids
reactingFoam	Solver for combustion with chemical reactions
buoyantBoussinesqPisoFoam	Transient solver for buoyant, turbulent flow of incompressible fluids
dsmcFoam	Direct simulation Monte Carlo (DSMC) solver for 3D, transient, multi-species flows
solidDisplacementFoam	Transient segregated finite-volume solver of linear-elastic, small-strain deformation of a solid body, with optional thermal diffusion and thermal stresses
financialFoam	Solves the Black-Scholes equation that governs the price of the option over time (1997 Nobel Prize in Economics)
mhdFoam	Solver for magnetohydrodynamics (MHD): incompressible, laminar flow of a conducting fluid under the influence of a magnetic field

### 3.4 Creating Solvers

The success of verbal language and mathematics is based on efficiency, especially in expressing abstract concepts. For example, in fluid flow, OpenFOAM uses the term “velocity field”, which has meaning without any reference to the nature of the flow or any specific velocity data. The term encapsulates the idea of movement with direction and magnitude and relates to other physical properties. In mathematics, we can represent velocity field by a single symbol, e.g.  $\mathbf{U}$ , and express certain concepts using symbols, e.g. “the field of velocity magnitude” by  $|\mathbf{U}|$ . The advantage of mathematics over verbal language is its greater efficiency, making it possible to express complex concepts with extreme clarity.

The problems that OpenFoam wants to solve in continuum mechanics are usually presented first in verbal language, then as partial differential equations in three dimensions of space and time. The equations contain the following concepts: scalars, vectors, tensors, and fields; tensor algebra; tensor calculus; dimensional units. The solution to these equations involves discretization procedures, matrices, solvers, and solution algorithms.

Programming languages that are object-oriented such as C<sup>++</sup> provide the mechanism (classes) to declare types and associated operations that are part of the verbal and mathematical languages used in science and engineering. For example, the velocity field introduced earlier can be represented in programming code by the symbol  $U$  and “the field of velocity magnitude” can be  $mag(U)$ . The velocity is a vector field for which there should exist, in an object-oriented code, a «vectorField» class. The velocity field  $U$  would then be an instance or object of the «vectorField» class; hence the term object-oriented.

The clarity of having objects in programming that represent physical objects and abstract entities should not be underestimated. The class structure concentrates development to contained regions of the code, i.e. the classes themselves, thereby making the code easier to manage. New classes can be derived or inherit properties from other classes, e.g. the «vectorField» can be derived from a vector class and a Field class. C<sup>++</sup> provides the mechanism of template classes such that the template class  $Field<Type>$  can represent a field of any  $<Type>$ , e.g. scalar, vector, tensor. The general features of the template class are passed on to any class created from the template. Templating and inheritance reduce duplication of code and create class hierarchies that impose an overall structure on the code.

A central theme of the OpenFOAM design is that the solver applications, written by using the OpenFOAM classes, have a syntax that closely resembles the partial differential equations being solved. For example the equation:

$$\frac{\partial \rho \mathbf{U}}{\partial t} + \nabla \cdot \varphi \mathbf{U} - \nabla \cdot \mu \nabla \mathbf{U} = -\nabla p \quad (3.1)$$

is represented by the code:

```

solve
(
    fvm::ddt(rho, U)
  + fvm::div(phi, U)
  - fvm::laplacian(mu, U)
  ==
  - fvc::grad(p)
);

```

This makes OpenFOAM an excellent choice for customization, compared to closed source software. More specifically:

- ✓ Users have total freedom to create or modify a solver.

- ✓ Users can easily reuse functionality that is pre-compiled into shared libraries.
- ✓ Compiled solvers can be tailored by a user for a specific need rather than 'bolt-on' subroutines, making OpenFOAM ideal for research and development.
- ✓ All applications, including those for CFD simulation, pre-/post-processing and meshing are compiled using common functionality in the collection of libraries included in OpenFOAM. This ensures consistency across the whole of OpenFOAM, rather than having a suite of packages compiled from entirely separate source code.
- ✓ Transparent solution algorithms which can be viewed by the user, encouraging better understanding of the underlying physics.

The use of advanced level C<sup>++</sup> as core programming language brings major benefits to users:

- ✓ Advanced error-checking at both compile and run time.
- ✓ Extremely robust solver and utility executables.
- ✓ High speed calculation with efficient memory management and fast linear equation solvers.
- ✓ Parallel processing with linear speed up with number of processors.

In this way, the understanding of the actual algorithm, the implemented models and equations are supposed to be much more important than a deep knowledge of object orientation and C<sup>++</sup> programming.

### **3.5 File structure of OpenFOAM cases**

Every OpenFOAM case has a similar structure with slight differences stemming only from the particular choice of solver. The basic file structure corresponds to that of Fig. 3.1.

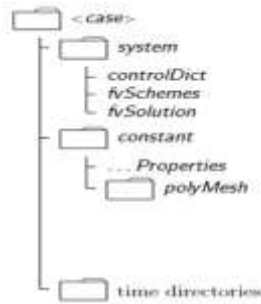


Fig. 3.1: File structure of an ordinary OpenFOAM case

The various steps to be undertaken when setting up a simulation in OpenFOAM are as follows: Boundary conditions have to be set, fluid properties must be selected, numerical schemes and algorithms for the solution of systems of equations must be chosen, and finally general simulations settings must be fixed. More specifically:

- «constant directory»: It contains a full description of the case mesh in a subdirectory «polyMesh» and files specifying physical properties for the application concerned, e.g. *transport Properties*.
- «system directory»: For setting parameters associated with the solution procedure itself. It contains at least the following three files:
  - «controlDict» where run control parameters are set including start/end time, time step and parameters for data output;
  - «fvSchemes» where discretization schemes used in the solution may be selected at run-time; and
  - «fvSolution» where the equation solvers, tolerances and other algorithm controls are set for the run.
- «time directories»: They contain individual files of data for particular fields. The data can be either initial or boundary values that the user must specify to define the problem or results written to file by OpenFOAM.

### 3.6 Numerical schemes

OpenFoam can support the following discretization methods of the governing equations:

- Second and fourth-order finite volume with mesh motion and topological changes
- Polyhedral Finite Element solver (mesh motion)
- Lagrangian particle tracking (discrete particle model); Diesel spray model
- Finite Area Method: FVM on a curved surface in 3-D
- A-posteriori error estimation

- Dynamic mesh handling and topology changes; automatic mesh motion

In this thesis, the solution of the equations was obtained using a Finite Volume discretization. Therefore, our analysis below is focused on the Finite Volume method of discretization (for further details and information see Weller (2004b)).

The «fvSchemes» dictionary in the system directory sets the numerical schemes for terms, such as derivatives in equations, which appear in specific applications. A brief description of how to specify the schemes in the «fvSchemes» dictionary follows. OpenFOAM offers complete freedom to choose from a wide selection of interpolation schemes for all terms.

The user first has a choice of discretization practice where standard Gaussian finite volume integration is the common choice. Gaussian integration is based on summing values on cell faces, which must be interpolated from cell centers. The user again has a completely free choice of interpolation scheme, with certain schemes being specifically designed for particular derivative terms, especially the convection divergence terms.

The set of terms, for which numerical schemes must be specified, are subdivided within the «fvSchemes» dictionary into the categories listed in Table 3.2. Each keyword in Table 3.2 is the name of a sub-dictionary which contains terms of a particular type, e.g. «gradSchemes» contains all the gradient derivative terms such as, for example,  $\text{grad}(p)$  which represents the gradient of  $p$ .

The «*interpolation Schemes*» sub-dictionary contains terms that are interpolations of values typically from cell centers to face centers. A selection of interpolation schemes in OpenFOAM are listed in Table 3.3.

The «*gradSchemes*» sub-dictionary contains gradient terms. The discretization scheme for each term can be selected from those listed in Table 3.4.

The «*divSchemes*» sub-dictionary contains divergence terms. For example, the syntax of the entry of a typical convection term found in fluid dynamics  $\nabla \cdot (\rho \mathbf{U} \mathbf{U})$ , in OpenFOAM applications is commonly given the identifier  $\text{div}(\text{phi}, \mathbf{U})$ , where  $\text{phi}$  refers to the momentum flux  $\phi = \rho \mathbf{U}$ .

The Gauss scheme is the only choice of discretization and requires a selection of the interpolation scheme for the dependent field, i.e.  $\mathbf{U}$  in our example. To summarize, the entries required are: Gauss «interpolationScheme».

The first time derivative ( $\partial/\partial t$ ) terms are specified in the «ddtSchemes» sub-dictionary. The discretization scheme for each term can be selected from those listed in Table 3.2.

There is also an off-centering coefficient  $\psi$  with the Crank-Nicholson scheme that blends it with the Euler scheme. A coefficient of  $\psi = 1$  corresponds to pure Crank-Nicholson and  $\psi = 0$  corresponds to pure Euler. The blending coefficient can help to improve stability in cases where pure Crank-Nicholson is unstable.

**Table 3.2: Main keywords used in «fvSchemes»**

<b>Keyword</b>	<b>Category of mathematical terms</b>
interpolationSchemes	Point-to-point interpolations of values
snGradSchemes	Component of gradient normal to a cell face
gradSchemes	Gradient $\nabla$
$\nabla \cdot$	$\nabla \cdot$
$\nabla^2$	$\nabla^2$
$\partial/\partial t, \partial^2/\partial t^2$	$\partial/\partial t, \partial^2/\partial t^2$
fluxRequired	Fields which require the generation of a flux

**Table 3.3: Interpolation schemes**

<b>Centred schemes</b>	
linear	Linear interpolation (central differencing)
cubicCorrection	Cubic scheme
midPoint	Linear interpolation with symmetric weighting
<b>Upwinded convection schemes</b>	
upwind	Upwind differencing
linearUpwind	Linear upwind differencing
skewLinear	Linear with skewness correction
filteredLinear2	Linear with filtering for high-frequency ringing
<b>TVD schemes</b>	
limitedLinear	limited linear differencing
vanLeer	van Leer limiter
MUSCL	MUSCL limiter
limitedCubic	Cubic limiter
<b>NVD schemes</b>	
SFCD	Self-filtered central differencing
Gamma $\psi$	Gamma differencing

**Table 3.4:** Discretization schemes available in «gradSchemes»

Discretisation scheme	Description
Gauss <interpolationScheme>	Second order, Gaussian integration
leastSquares	Second order, least squares
fourth	Fourth order, least squares
cellLimited <gradScheme>	Cell limited version of one of the above schemes
faceLimited <gradScheme>	Face limited version of one of the above schemes

**Table 3.5:** Discretization schemes available in «ddtSchemes»

Scheme	Description
Euler	First order, bounded, implicit
localEuler	Local-time step, first order, bounded, implicit
CrankNicholson $\psi$	Second order, bounded, implicit
backward	Second order, implicit
steadyState	Does not solve for time derivatives

### 3.7 Mesh generation with the blockMesh utility

This section describes the mesh generation utility «blockMesh» supplied with OpenFOAM. The «blockMesh» utility creates parametric meshes with grading and curved edges. The mesh is generated from a dictionary file named «blockMeshDict» located in the «constant/polyMesh» directory of a case. The utility «BlockMesh» reads this dictionary, generates the mesh and writes out the mesh data to points and faces, cells and boundary files in the same directory.

The principle behind «blockMesh» is to decompose the domain geometry into a set of one or more three dimensional, hexahedral blocks. Edges of the blocks can be straight lines, arcs or splines. The mesh is ostensibly specified as a number of cells in each direction of the block, sufficient information for «blockMesh» to generate the mesh data.

Each block of the geometry is defined by 8 vertices, one at each corner of a hexahedron. The vertices are written in a list so that each vertex can be accessed using its label, remembering that OpenFOAM always uses the C<sup>++</sup> convention that the first element of the list has label '0'. It is also possible to generate blocks with less than 8 vertices by collapsing one or more pairs of vertices on top of each other.

The «blockMeshDict» file is a dictionary using keywords described in Table 3.6. The «convertToMeters» keyword specifies a scaling factor by which all vertex coordinates in the mesh description are multiplied. For instance, «convertToMeters



0.001» means that all coordinates are multiplied by 0.001, i.e. the values quoted in the «blockMeshDict» file are in mm. The *vertices* of the blocks of the mesh are given as a standard list named *vertices*.

Each *edge* joining 2 vertex points is assumed to be straight by default. However any edge may be specified to be curved by entries in a list named «edges». The list is optional; if the geometry contains no curved edges, it may be omitted. Each entry for a curved edge begins with a keyword specifying the type of curve from those listed in Table 3.6. The keyword is then followed by the labels of the 2 vertices that the edge connects.

The *block* definitions are contained in a list named «blocks». Each block definition is a compound entry consisting of a list of vertex labels, a vector giving the number of cells required in each direction, the type and list of cell expansion ratio in each direction. Then the blocks are defined as follows for example:

```
blocks
(
  hex (0 1 2 3 4 5 6 7) // vertex numbers
  (10 10 10) // numbers of cells in each direction
  simpleGrading (1 2 3) // cell expansion ratios
);
```

**Table 3.6:** Edge types available in the *blockMeshDict* dictionary

Keyword selection	Description	Additional entries
arc	Circular arc	Single interpolation point
simpleSpline	Spline curve	List of interpolation points
polyLine	Set of lines	List of interpolation points
polySpline	Set of splines	List of interpolation points
line	Straight line	—

### 3.8 Linear solver control

The equation solvers, tolerances and algorithms are controlled from the «fvSolution» dictionary in the system directory. Below is an example of a set of entries from the «fvSolution» dictionary required for the «mhdFoam» solver that was used in this thesis.

```
solvers
{
  p
  {
    solver      PCG;
```

```

    preconditioner DIC;
    tolerance 1e-06;
    relTol 0;
}
U
{
    solver PBiCG;
    preconditioner DILU;
    tolerance 1e-05;
    relTol 0;
}
B
{
    solver PBiCG;
    preconditioner DILU;
    tolerance 1e-05;
    relTol 0;
}
pB
{
    solver PCG;
    preconditioner DIC;
    tolerance 1e-05;
    relTol 0;
}
}
PISO
{
    nCorrectors 3;
    nNonOrthogonalCorrectors 0;
}
BPISO
{
    nCorrectors 3;
}

```

The dictionary «FvSolution» contains a set of subdictionaries that are specific to the solver being run. However, there is a small set of standard subdictionaries that cover most of those used by the standard solvers. These subdictionaries include solvers, *relaxation Factors*, PISO and SIMPLE algorithms.

The first sub-dictionary in our example, and one that appears in all solver applications, is «solvers». It specifies each linear-solver that is used for each discretised equation. It should be noted that the term linear-solver refers to the method of number-crunching to solve the set of linear equations, as opposed to application solver which describes the set of equations and algorithms to solve a particular problem.

The syntax for each entry within «solvers» uses a keyword that is the word relating to the variable being solved in the particular equation. For example, «mhdFoam» solves equations for velocity  $U$ , magnetic field  $B$ , pressure  $p$  and a magnetic pressure  $p_B$ . The keyword is followed by a dictionary containing the type of solver and the parameters that the solver uses. The solver is selected through the «solver» keyword from the choice in OpenFOAM, listed in Table 3.7. The parameters, including tolerance,  $relTol$ , preconditioner, etc. are described in following sections.

**Table 3.7:** Linear solvers (\*PCG for symmetric, PBiCG for asymmetric matrices)

Solver	Keyword
Preconditioned (bi-)conjugate gradient	PGG/PBiCG*
Solver using a smoother	smoothSolver
Generalised geometric-algebraic multi-grid	GAMG

The sparse matrix solvers are iterative, i.e. they are based on reducing the equation residual over a succession of solutions. The residual is a measure of the error in the solution so that the smaller it is, the more accurate the solution. More precisely, the residual is evaluated by substituting the current solution into the equation and taking the magnitude of the difference between the left and right hand sides; it is also normalized in order to make it independent of the scale of problem being analyzed. Before solving an equation for a particular field, the initial residual is evaluated based on the current values of the field. The residual is re-evaluated after each iteration. The solver stops if either of the following conditions is reached:

- the residual falls below the solver tolerance, *tolerance*;
- the ratio of current to initial residuals falls below the relative tolerance, *relTol*;

The solver tolerance represents the level at which the residual is small enough that the solution can be considered sufficiently accurate. The solver relative tolerance limits the relative improvement from initial to final solution. Furthermore, there is a range of options for the preconditioning of matrices in the conjugate gradient solvers, represented by the «preconditioner» keyword in the solver dictionary. The preconditioners are listed in Table 3.8.

*Table 3.8: Preconditioner options*

<b>Preconditioner</b>	<b>Keyword</b>
Diagonal incomplete-Cholesky (symmetric)	DIC
Faster diagonal incomplete-Cholesky (DIC with caching)	FDIC
Diagonal incomplete-LU (asymmetric)	DILU
Diagonal	diagonal
Geometric-algebraic multi-grid	GAMG
No preconditioning	none

Finally, most fluid dynamics solver applications in OpenFOAM use the *pressure-implicit split operator* (PISO) or *semi-implicit method for pressure-linked equations* (SIMPLE) algorithms developed at Imperial College, London. These algorithms are iterative procedures for solving equations for velocity and pressure, PISO being used for transient problems and SIMPLE for steady-state. Both are based on evaluating some initial solutions and then correcting them. SIMPLE only makes one correction whereas PISO requires more than one, but typically not more than four.

### 3.9 Post-processing

OpenFOAM is supplied with a post-processing utility «paraFoam» that uses «ParaView», an open source visualization application. In addition, the other programs which are offered are «EnSight», «Fieldview» and post-processing supplied with the commercial CFD package «Fluent».

### Epilogue

The aim of OpenFOAM is to produce a C<sup>++</sup> class library in which it is easy to develop Computational Fluid Dynamics (CFD) codes in order to investigate modeling and simulation of fluid flows. In essence, OpenFOAM is a high-level meta-language, which closely parallels the mathematical description of continuum mechanics. As well as simplifying the implementation of new models, this makes checking the modeling more straightforward. This aspect is enhanced by the inclusion of features such as automatic dimension checking of operations. In addition to this, object-orientation techniques enable the creation of data types that closely mimic those of continuum mechanics, and the operator overloading possible in C<sup>++</sup> allows normal mathematical symbols to be used for the basic operations. Thus, the use of object-oriented programming (OOP) methodology has enabled the dissociation of different levels of the code. This minimizes unwanted interaction, and permitting research into the numerics (differencing schemes and matrix-inversion techniques) to be separated from modeling.

In conclusion, OpenFOAM demonstrates that it is possible to implement a mathematically oriented metalanguage. More information about object-oriented techniques and applications in OpenFOAM are referred in Weller et al. (1998).

4.1. Literature survey

In this chapter a brief literature review about the *Orszag-Tang* vortex and its modeling is presented. The cited references are often quoted by other authors who are working on this problem.

The Orszag-Tang vortex is a well-known test for magnetohydrodynamic (MHD) numerical models which was first studied by Orszag & Tang (1979). In their work, they investigated the formation of singularities in two-dimensional MHD flow by direct numerical simulations (DNS). In brief, the Orszag-Tang vortex flow is an initial value MHD problem occurring in a square box with periodic boundary conditions in both x and y directions. Its frequent use in many studies is because it contains many important features of MHD turbulence.

The governing equations of the present incompressible, constant property fluid flow are:

Mass continuity:  $\nabla \cdot \mathbf{v} = 0$  (4.1)

Momentum:  $\rho \left( \frac{\partial \mathbf{v}}{\partial t} + \mathbf{v} \nabla \mathbf{v} \right) = -\nabla p + \mathbf{J} \times \mathbf{B} + \mu \nabla^2 \mathbf{v}$  (4.2)

Maxwell equations:  $\nabla \cdot \mathbf{B} = 0$  (4.3)

$$\nabla \times \mathbf{B} = \mu_0 \mathbf{J} + \frac{\partial \mathbf{D}}{\partial t} \approx \mu_0 \mathbf{J}$$
 (4.4)

Assuming  $\frac{\partial \mathbf{D}}{\partial t} \ll \mathbf{J}$  (4.5)

$$\nabla \times \mathbf{E} = -\frac{\partial \mathbf{B}}{\partial t}$$
 (4.6)

Charge continuity:  $\nabla \cdot \mathbf{J} = 0$  (4.7)

Ohm's law:  $\mathbf{J} = \sigma (\mathbf{E} + \mathbf{v} \times \mathbf{B})$  (4.8)

Combining the Equations (4.4), (4.6) and (4.8) and taking the curl, the following equation is derived

$$\frac{\partial \mathbf{B}}{\partial t} = \nabla \times (\mathbf{v} \times \mathbf{B}) + \frac{\eta}{\mu_0} \nabla^2 \mathbf{B}$$
 (4.9)

where,  $\rho$  is the number density,  $\mathbf{v}$  is the fluid velocity,  $\mathbf{B}$  is the magnetic field strength,  $\mathbf{E}$  is the electric field strength,  $p$ ,  $\mu$ ,  $\eta = 1/\mu_0\sigma$ ,  $\mu_0$ ,  $\sigma$ , are the fluid pressure, viscosity, resistivity, magnetic permeability, and electric conductivity, respectively,  $\mathbf{J}$  is the current density and  $\mathbf{D}$  the electric flux density.

The first term on the right hand side of Eq. (4.9) is the convective term and the second is the diffusion term. The relationship between these two terms allows to obtain the magnetic Reynolds number,  $R_m = \mu_0 \sigma L u$ , where  $L$  and  $u$  are the characteristic length and velocity, respectively. This is a parameter that must be considered in the modeling assumptions for MHD flows. In the case of  $R_m \leq 1$  the electromagnetic forces are ruled by the flow field and the convective and dissipative terms must be retained in the induction equation. In the case of a high magnetic Reynolds number,  $R_m \gg 1$ , we may neglect the diffusion term, but we end up with a strong coupling, so the momentum, Ohm's law, energy equation and induction equation cannot be treated independently. For the case of a low magnetic Reynolds number,  $R_m \ll 1$ , we may neglect the convective term and we can treat each equation separately introducing the contributions of the magnetic field only as a source term.

The flow domain is specified as:  $0 \leq x \leq 2\pi$ ,  $0 \leq y \leq 2\pi$  with periodic boundary conditions in both  $x$  and  $y$  directions. Moreover, non-random initial conditions are imposed at  $t=0$ , as follows:

$$\mathbf{v} = -2\sin y \mathbf{e}_x + 2\sin x \mathbf{e}_y \quad (4.10)$$

$$\mathbf{B} = -2\sin y \mathbf{e}_x + 2\sin 2x \mathbf{e}_y \quad (4.11)$$

As time increases, the MHD flow with the initial conditions (4.10, 4.11) becomes increasingly complicated due to the nonlinear interaction of the governing equations. Thus, an analytical solution does not seem possible. Orszag & Tang (1979) solved equations (4.1) to (4.9) using a pseudospectral method with a truncated Fourier series expansion of the flow variables. Their computer code was a modification of the KILOBOX code used for high resolution two-dimensional turbulence calculations Orszag (1976). Furthermore, they showed that two-dimensional (2-D) MHD turbulence is not as singular as three-dimensional (3-D) hydrodynamic one, but it is more singular than 2-D hydrodynamic turbulence. In fact, as Pouquet (1978) suggested, 2-D MHD turbulence is dynamically very similar to 3-D hydrodynamic turbulence. He also proposed that the flow singularities, which appear in 2-D MHD turbulence, imply that the small scale structures are more intermittent than the small-scale structure of 2-D hydrodynamic flow.

The behavior occurring in 2-D MHD flow is quite different from that in 2-D hydrodynamic flow. In 2-D hydrodynamic flow, nonlinear interaction conserves mean-square vorticity (enstrophy), so that the dissipation rate in free dissipation turbulence

satisfies that  $\varepsilon(t) \leq \varepsilon(0)$  for  $t \geq 0$ . In contrast,  $\varepsilon(t) / \varepsilon(0)$  can achieve values much larger than one in MHD flow. In Fig. 4.1, the total energy dissipation  $\varepsilon(t)$  is plotted versus  $t$  for  $\nu=\eta=0.08, 0.04, 0.02, 0.01$  and  $0.005$ . When  $\nu=\eta$  is halved, the peak of energy dissipation rate is decreased by about 20 %.

Moreover, according to Orszag & Tang (1979),  $\nu=\eta=0$  is the limit where three invariants of motion exist: total energy (Eq. 4.12), mean-square magnetic vector potential (Eq. 4.13) and cross helicity (Eq. 4.14). Cross helicity measures the degree of correlation between velocity and magnetic fluctuations in the turbulent state. Together with energy, cross-helicity undergoes a turbulent cascade from large to small scales.

$$E = \left(\frac{1}{2\pi}\right)^2 \cdot \frac{1}{2} \cdot \int_0^{2\pi} \int_0^{2\pi} |v^2| + |B^2| dx dy \quad (4.12)$$

$$\bar{A} = \left(\frac{1}{2\pi}\right)^2 \cdot \int_0^{2\pi} \int_0^{2\pi} A^2 dx dy \quad (4.13)$$

$$H_c = \left(\frac{1}{2\pi}\right)^2 \cdot \int_0^{2\pi} \int_0^{2\pi} \mathbf{v} \cdot \mathbf{B} dx dy \quad (4.14)$$

When  $\nu>0$  or  $\eta>0$ , the rate of total energy dissipation is given by Eq. 4.15

$$\varepsilon(t) = -\frac{dE}{dt} = \left(\frac{1}{2\pi}\right)^2 \left[ \nu \int_0^{2\pi} \int_0^{2\pi} \omega^2 dx dy + \eta \int_0^{2\pi} \int_0^{2\pi} j^2 dx dy \right] \quad (4.15)$$

In fact, the initial vortex, which rapidly evolves into fully developed highly nonlinear turbulence, can be used as a test case for the problem of dissipation in collisionless plasmas (Parashar, 2009). Although Tokamak plasmas are compressible, they can be represented in terms of incompressible MHD turbulence for Mach numbers less than unity (Biskamp & Welter, 1989). Thus, an incompressible flow model has been implemented which illustrates the emergence of small scale structures through magnetic reconnection and current sheet formation.

The Orszag-Tang vortex has been extensively studied by Biskamp & Welter (1989) and by Friedel et al. (1997). The compressible MHD version has also been studied by Dahlburg & Picone (1989, 1991). It has been used as a numerical test problem for test for a numerous magnetohydrodynamic (MHD) numerical models such as by Wu (2007). Wu (2007) performed the calculations using a high order accurate



weighted essentially non-oscillatory (WENO) finite difference scheme for solving the equations of incompressible fluid dynamics and magnetohydrodynamics.

As  $\nu$  and  $\eta$  are reduced, the current strength increases as does the intensity of the vorticity. These indicate the convergence of the results with respect to the spatial resolution. They also show that the convergence depends strongly on the spatial location. In regions around  $0 < x < 0.5\pi$  and  $1.5\pi < x < 2\pi$ , the solution converges quickly, while in the region around  $0.5\pi < x < 1.5\pi$ , a high spatial resolution is required for convergence. This is because a strong current sheet forms near the  $0.5\pi < x < 1.5\pi$  region. Fig. 4.2 shows the energy distributions up to  $t=4$  for the case with  $\omega=\eta=0$ . Although kinetic energy ( $E_K$ ) and magnetic energy ( $E_B$ ) are equal initially,  $E_B$  becomes much larger than  $E_K$  at later times.

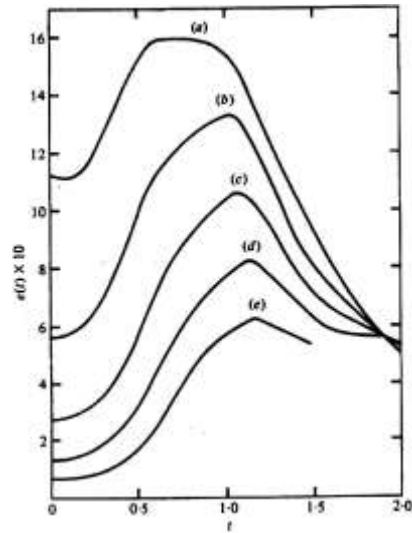


**Fig. 4.1.** The Orszag-Tang problem: Plot of energy dissipation rate  $\varepsilon(t)$  of 2-D MHD flow.  
 (a)  $\nu=\eta=0.08$  ( $Ra=36$ ),  $\nu=\eta=0.04$  ( $Ra=92$ ),  $\nu=\eta=0.02$  ( $Ra=232$ ),  $\nu=\eta=0.01$  ( $Ra=585$ ),  
 (b)  $\nu=\eta=0.005$  ( $Ra=1474$ ), (Orszag & Tang (1979))

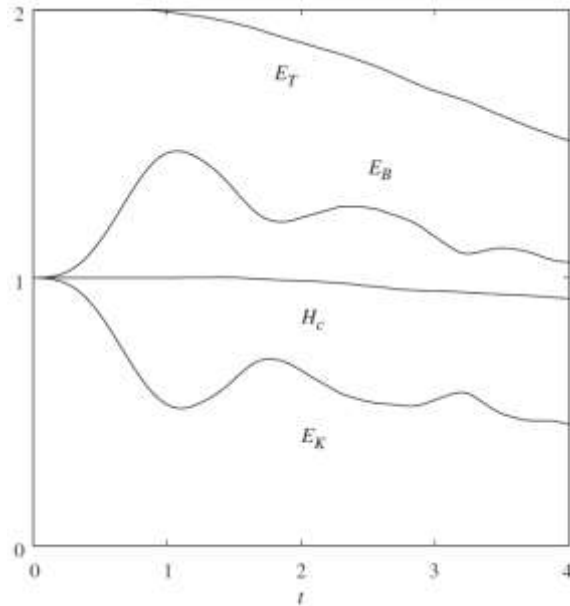


**Fig. 4.2** The Orszag-Tang problem. Distributions of energy (kinetic ( $E_K$ ), magnetic ( $E_M$ ), their sum  $E_T$ ) and cross helicity ( $H_c$ ), normalized by  $8\pi^2$ , for  $\nu=\eta=0$  with  $1024 \times 1024$  grid, (Orszag & Tang (1979))

## 4.2. Orszag-Tang vortex modeling in the OpenFoam CFD library

Generally, fluid flow is mathematically described by the conservation of mass and momentum. The general form of a conservation equation for a flow quantity  $\varphi$  is

$$\frac{\partial \rho \varphi}{\partial t} + \nabla \cdot (\rho \mathbf{v} \varphi) - \nabla \cdot (\rho \Gamma_{\varphi} \nabla \varphi) = S_{\varphi} \quad (4.16)$$

where  $\rho$  is fluid density,  $\mathbf{v}$  its velocity,  $\Gamma_{\varphi}$  its diffusivity,  $t$  is time, and  $S_{\varphi}$  a source term.

The transport equation for the conservation of mass (continuity equation) is derived by setting  $\varphi=1$  in Eq. 4.16 and not having mass source terms. This leads to

$$\frac{\partial \rho}{\partial t} + \nabla \cdot (\rho \mathbf{v}) = 0 \quad (4.17)$$

The momentum equation, neglecting gravitational effects, according to Bird et al. (2002) is

$$\frac{\partial (\rho \mathbf{v})}{\partial t} + \nabla \cdot (\rho \mathbf{v} \mathbf{v}) - \nabla \cdot \boldsymbol{\tau} = -\nabla p \quad (4.18)$$

where  $\boldsymbol{\tau}$  is viscous stress tensor given by

$$\boldsymbol{\tau} = -\mu \left( \nabla \mathbf{v} + (\nabla \mathbf{v})^T \right) + \mu \frac{2}{3} \mathbf{I} \nabla \cdot \mathbf{v} \quad (4.19)$$

where  $\mu$  is the viscosity of a Newtonian fluid.

All calculations were performed within the OpenFOAM package which employs the finite volume method. The finite volume method subdivides the flow domain into a finite number of smaller non-overlapping control volumes. The transport equations are then integrated over each these control volumes by approximating the variation of flow properties between mesh points with differencing schemes. This section gives only a brief overview on the FVM. For a complete discussion on the FVM the reader is referred to Versteeg & Malalasekera (1995).

### 4.2.1 Discretization of the Solution Domain

The desired solution domain is broken up, discretised, into a number of cells, or control volumes. These cells do not overlap one another and completely fill the computational domain. Generally variables are stored at the cell centroid, although they may be stored on faces or vertices. A cell is bounded by a set of flat faces with no limitation on the number of faces or their alignment, which can be called arbitrarily unstructured. Two neighboring cells must only share one face, which is then called an

internal face. A face belonging only to one cell is called a “boundary face”. The minimum information required to define a mesh consists of:

Points which are defined by their position in three-dimensional space

Faces which are defined by a list of points

Cells which are defined by a list of faces and

Boundary patches which are defined by a list of boundary faces, with each face being a member of only one boundary patch. The boundary patches have to contain all boundary faces.

#### 4.2.1.1 Discretization of the equations

The partial differential equation (4.16) is transformed into an algebraic equation, which can be expressed as

$$\mathbf{M}\mathbf{x} = \mathbf{b} \quad (4.20)$$

where  $\mathbf{M}$  is a square matrix,  $\mathbf{x}$  the vector of the dependent variable and  $\mathbf{b}$  is the source vector. Finite Volume (FV) discretization of each term is formulated by first integrating the term over a cell volume. Most spatial derivatives are converted to integrals over the cell surface  $S$  bounding the volume using Gauss’s theorem

$$\int_V \nabla \phi dV = \int_S \phi d\mathbf{S} \quad (4.21)$$

where  $\mathbf{S}$  is the surface area vector and  $\phi$  can represent any variable. Implicit terms constitute the matrix  $\mathbf{M}$ , explicit terms constitute the source vector  $\mathbf{b}$ .

#### 4.2.1.2 The Diffusion Term

The diffusion term in Eq. 4.16 is integrated over a control volume and linearised as follows:

$$\int_V \nabla \cdot (\Gamma \nabla \phi) dV = \int_S (\Gamma \nabla \phi) d\mathbf{S} = \sum_f \Gamma_f \mathbf{S}_f \cdot (\nabla \phi)_f \quad (4.22)$$

This can be discretized when the length vector  $d$  between the centre of the cell of interest  $P$  and the centre of a neighboring cell  $N$  is orthogonal to the face:

$$\mathbf{S}_f \cdot (\nabla \phi)_f = \mathbf{S}_f \cdot \frac{\phi_N - \phi_P}{|d|} \quad (4.23)$$

#### 4.2.1.3 The Convection Term

The convection term is integrated over a control volume and linearised as follows:

$$\int_V \nabla \cdot (\rho \mathbf{v} \phi) dV = \int_S (\rho \mathbf{v} \phi) dS = \sum_f S_f (\rho \mathbf{v})_f \phi_f \quad (4.24)$$

The face field value,  $\phi_f$ , can be evaluated using a variety of schemes, as follows: Central differencing which is used in the present work is second-order accurate but unbounded, meaning that the error of discretization reduces with the square of the grid spacing and that the limits of  $\phi$  are not necessarily preserved. One of the major inadequates of the central differencing scheme is its inability to identify flow direction. The value property  $\phi$  at a cell face is always influenced by both surrounding values in central differencing. In a strongly convective flow the above treatment is unsuitable because the upstream value should have stronger influence on the node P. The upwind differencing takes into account the flow direction when determining the value at a cell face: the convected value of  $\phi$  at a cell face is taken to be equal to the value at the upstream node. These two schemes can be blended in order to preserve boundedness with reasonable accuracy and there are many more schemes implemented which might be investigated.

#### 4.2.1.4 The Gradient Term

The gradient term described here is an explicit one. Usually it is evaluated using the Gauss integration by applying the Gauss theorem to the volume integral:

$$\int_V \nabla \phi dV = \int_S \phi d\mathbf{S} = \sum_f \mathbf{S}_f \phi_f \quad (4.25)$$

There are more ways to evaluate the gradient term which can be found in the Programmer's Guide of OpenFOAM (Weller, 2004b).

#### 4.2.1.5 The Time Derivative

The time derivative  $\frac{\partial}{\partial t}$  is integrated over a control volume as follows:

$$\frac{\partial}{\partial t} \int_V \rho \phi dV$$

This is discretised by using the following methods:

new values,  $\varphi^n \equiv \varphi(t=\Delta t)$  at the time stem being solved for,  
old values  $\varphi^0 \equiv \varphi(t)$  that were stored from the previous time step, or  
Euler implicit which is first order accurate in time, meaning that the discretization error reduces with smaller time steps.

Thus, the time derivative is discretised as follows

$$\frac{\partial}{\partial t} \int_V \rho \varphi dV = \frac{(\rho_P \varphi_P V)^n - (\rho_P \varphi_P V)^0}{\Delta t} \quad (4.27)$$

Again, more ways to evaluate the time term are in the Programmer's Guide (Weller, 2004b).

#### 4.2.1.6 Temporal Discretization

The treatment of time derivatives was explained in the previous section. However, the spatial derivatives in a transient problem also need some consideration as  $\varphi$  is a function of space and time and the spatial derivatives are averaged over one or more time steps. If all spatial terms are denoted as  $A\varphi$ , where  $A$  is any spatial operator, e.g. Laplacian, then a transient partial differential equation (PDE) can be expressed as

$$\int_t^{t+\Delta t} \left[ \frac{\partial}{\partial t} \int_V \rho \varphi dV + A\varphi dV \right] dt = 0 \quad (4.28)$$

Using the Euler implicit method of eq. 4.27, the first term can be expressed as

$$\int_t^{t+\Delta t} \left[ \frac{\partial}{\partial t} \int_V \rho \varphi dV \right] dt = \frac{(\rho_P \varphi_P V)^n - (\rho_P \varphi_P V)^0}{\Delta t} \Delta t \quad (4.29)$$

The second term of equation 4.28 can be expressed as

$$\int_t^{t+\Delta t} [A\varphi dV] dt = \int_t^{t+\Delta t} A^* \varphi dt \quad (4.30)$$

where  $A^*$  represents the spatial discretization of  $A$ . That integral can be discretised as:

Euler implicit taking only current values  $\varphi^n$ , is first order accurate in time, guarantees boundedness and is unconditionally stable.

$$\int_t^{t+\Delta t} A^* \varphi dt = A^* \varphi^n \Delta t \quad (4.31)$$

Explicit taking only values  $\varphi_0$  from the previous timestep, guarantees boundedness and is first order accurate in time.

$$\int_t^{t+\Delta t} A^* \varphi dt = A^* \varphi^0 \Delta t \quad (4.32)$$

It is unstable if the Courant number  $Co$  is greater than one. The Courant number is defined as

$$Co = \frac{\mathbf{v}_f \cdot \mathbf{d}}{|\mathbf{d}|^2} \Delta t \quad (4.33)$$

where  $\mathbf{v}_f$  is the velocity of the flow or velocity of a wave front for the acoustic Courant number and  $\mathbf{d}$  is the length vector between two neighboring cell centers.

Crank Nicholson taking a mean of current values  $\varphi_n$  and old values  $\varphi_0$ . It is second order accurate in time, unconditionally stable, but does not guarantee boundedness.

$$\int_t^{t+\Delta t} A^* \varphi dt = A^* \left( \frac{\varphi^n + \varphi^0}{2} \right) \Delta t \quad (4.34)$$

## 4.2.2 Numerical Setup

For the present calculations, the «mhdFoam» solver (Weller, 2004b) of the OpenFOAM package was used, which is a solver for the flow of an incompressible electrically-conducting liquid with constant properties in a magnetic field and it is governed by the Navier–Stokes equations together with Maxwell’s equations and Ohm’s law (eq. 4.1-4.9 ). Assuming that  $\frac{\partial \mathbf{D}}{\partial t}$  is negligible for non-relativistic plasma computations, then

$$\mathbf{J} \times \mathbf{B} = \frac{1}{\mu_0} (\nabla \times \mathbf{B}) \times \mathbf{B} = -\nabla \frac{B^2}{2\mu_0} + \frac{1}{\mu_0} \mathbf{B} \nabla \mathbf{B} \quad (4.35)$$

so the momentum equation (4.2) takes the form

$$\frac{\partial \mathbf{v}}{\partial t} + \mathbf{v} \nabla \mathbf{v} = -\nabla \left( p + \frac{B^2}{2\mu_0} \right) + \nabla \cdot \left( \frac{\mathbf{B}\mathbf{B}}{\mu_0} \right) + \nu \nabla^2 \mathbf{v} \quad (4.36)$$

The overall pressure is given by  $P_{\text{total}} = p + B^2/2\mu_0$ , in which the second contribution corresponds to the magnetic pressure. The latter acts like a pressure in the direction transverse to the magnetic field, the magnetic field resists to compressibility

just like the fluid pressure. The term  $B\mathbf{B}/\mu_0$  in equation (4.36) is called the hoop stress and acts like a tension along the lines of magnetic force, bearing some similarity with the viscous stresses. It represents tension along field lines when they are curved, similar to the force exerted by a stretched elastic band.

As far as the induction equation (4.9) is concerned, we retained the diffusion and convective terms in the induction equation, thus solving for the more general case of a strong coupling between equations.

### 4.2.3 Results of the Orszag-Tang flow

As a next step, the incompressible Orszag-Tang vortex flow was simulated. The non-random initial conditions of the Orszag-Tang problem are illustrated in Fig. 4.3.

Concerning the numerical process, Eqs. (4.1) and (4.2) together with the initial conditions (Eqs. 4.10 and 4.11), are solved by using a finite volume technique based on the transient pressure-velocity coupling algorithm PISO, Issa (1986). PISO relies on the splitting of the solution process into a series of steps where operations on pressure are decoupled from those on velocity at each step. Furthermore, a fictitious magnetic-flux pressure is introduced into the magnetic-field equation, Eq. (4.9), to facilitate the obedience of the divergence-free constraint on  $\mathbf{B}$  (Eq. (4.3)) in the same manner as the pressure equation is used in PISO. The resulting field  $p_H$  has no physical meaning, Weller et al. (1998). The numerical schemes, which were used in the simulations, are the Crank-Nicolson scheme for the transient terms, central discretization for the laplacian and grad terms and gamma differencing for the convection terms, Jasac (1996). At each step, the solution is iterated until the residuals of the mass, momentum, and temperatures equations become smaller than  $10^{-7}$ . Finally, the MHD numerical model used the conjugate-gradient method, with incomplete Cholesky preconditioning (ICCG) (Jacobs (1980)), in order to solve the symmetric matrices and the Bi-CGSTAB method (Van der Vost (1992)) for the asymmetric matrices.

Solutions obtained at time  $t=1$  using a  $512 \times 512$  grid are presented in Fig. 4.4. Fig. 4.4a and 4.4b demonstrate that, over time, there occurs dynamic alignment of the velocity and magnetic fields. In addition, this two-dimensional MHD turbulence is to a great extent more intermittent than the hydrodynamic one, as indicated by the S-shaped structure in Fig. 4.4c. The results show that dissipation arises primarily in the regions of weak magnetic field, where large current densities can be generated. Such localized



dissipation of magnetic energy involves mass transport from outside regions (where the “frozen-in” condition is satisfied) into the dissipative region.

Furthermore, the results show that the region of large current density is highly correlated with the region of large vorticity (Fig. 4.4c and 4.4d). This occurs because large gradients in the flow and magnetic fields can take place only at the Alfvén wave fronts. A total view of the time evolution of the velocity field, the magnetic field, the current density and the vorticity can be seen in Fig. 4.5a and 4.5b. Note the dynamic alignment of the velocity and magnetic fields that has already been pointed out. Finally, in Fig. 4.6, the variation of kinetic, magnetic and total energy over time indicates that there is an important energy transfer between the kinetic and magnetic components.

A simple physical explanation for the production of small-scale motion by MHD flows may be as follows: When  $v$  and  $\mu_0$  are small, an initial weak magnetic field is stretched and convected by the velocity field and thus wrapped into tight “ropes” that follow closely the large-scale fluid flow. When neighboring lines of magnetic force are thus stretched close to each other, magnetic diffusion can break the lines of force and locally reconnect them. When the lines of force brake, their tension force reacts back on the flow field to reproduce small eddies on top of the larger ones convected, giving an enhanced cascade process. The above explanation was given by Orszag & Tang (1989) and it is adopted in this thesis. For further details the reader is referred to section 2.4 where an analysis on magnetic lines reconnection in resistive MHD is provided.

Finally, it should be noted that reconnection events may occur only in resistive MHD where the effect of resistivity is to diffuse the magnetic field. On the other hand, in ideal MHD, where the medium is considered to be a perfect electrical conductor, the magnetic field lines can be thought of as being attached to the fluid and vice versa. This so-called “frozen-in” condition was analyzed comprehensively in section 2.3. An extensive examination on the dynamics of decaying two-dimensional MHD turbulence is elaborated by Biskamp & Welter (1989).

Extension of this picture to three dimensions is more delicate. However, the most intense current structures might develop in the limit of high Reynolds numbers, which relates to the heating of the solar corona, or the dynamics of flux transfer events in the magnetospheric environment. Many articles refer to the 3D Orszag-Tang vortex such as Mininni et al. (2006), Grauer & Marliani (2000) and Politano et al. (1995). Work on 3D flows such as that of Greene (1988) showed that the topology of a reconnecting region is more complex than in 2D and can lead to more varied behavior.

It should be noted that many turbulent media, such as nonconducting neutral gases and tokamak plasmas, are compressible and the relevance of incompressible results is questionable. In the compressible Orszag-Tang vortex, the interaction of the non-linear terms leads to supersonic MHD turbulence, making this problem a good test of the algorithm's ability to handle such MHD turbulence and shock waves. Thus, the turbulence can produce acoustic and shock waves which interact with each other and with the turbulent field itself. As in the incompressible case, the magnetic field is still constrained to be solenoidal. In addition, the magnetic field can evolve differently in a compressible fluid; for example, magnetic flux can accumulate in compressed regions.

Since the current sheets dissipate magnetic energy at early times, the reconnection is weaker as the initial supersonic Mach number increases. Therefore, the evolution and structure of the "supersonic" Orszag-Tang flow differs significantly from those of its subsonic and incompressible counterparts as shown by Picone & Dahlburg (1989, 1991).

Magnetic fields play an important dynamical role in the solar wind, in stars, or the interstellar medium. The associated flows have large but finite Reynolds numbers, and nonlinear mode coupling leads to the formation of intermittent structures. Viscosity and magnetic diffusivity also play a role. Tearing mode behavior develops and reconnection takes place as has already been mentioned. Questions arise as to how rapidly dissipation occurs as the Reynolds numbers increase, what the origin of the intermittent structures is, and how fast they form.

For these long-standing problems, e.g. in the context of reconnection events in the magnetopause or in heating of stellar coronas, many other phenomena may play an important part, such as compressibility or ionization. These can lead to a more complex Ohm's law with, e.g. a Hall current, or to the inclusion of radioactive or gravitational processes.

### 5.1. Literature survey

In this chapter, the two-dimensional MHD natural convection flow of an electrically conductive fluid in an internally heated horizontal shallow cavity with electrically insulated walls is studied for the case where the horizontal walls are adiabatic and the vertical sidewalls are isothermal. An external uniform magnetic field is applied in the vertical direction of the cavity. The main feature of the present flow is a symmetric double-cell Hadley circulation with the fluid ascending in the centre of the cavity and descending near the end walls. The method of the matched asymptotic expansions is used to obtain solutions of the flow and heat transfer problem. This analysis which is valid for large cavity aspect ratios and for any magnetic field strength is particularly helpful for the determination of the flow field without expensive simulations. In addition to the analytical solution, the laminar flow is also studied numerically for a range of Hartmann, Prandtl and Rayleigh numbers in order to verify the analytical results, to calculate the constants which arise by the analytical approach and to study the non-linear regions of the flow.

Fluid convection generated by internal heat arises in a variety of technological and geophysical applications. Some of the most important fields are the Czochralski and the horizontal Bridgman crystal growth techniques (Hjellming (1990), Oreper and Szekely (1983), Miller and Pernell (1982)), the fusion liquid metal blanket (see, for example, Proust et al. (1993)), and the Earth dynamo convection magnetic fields (see, for example, Kuang et al. (1999)). The working fluids of most of these applications of MHD natural convection are electrically conductive liquid metals. The basic feature of liquid metal flows in cavities is the initialization of strong non-linear effects throughout the cavity that makes difficult any analytical approach of the flow above a critical Rayleigh number,  $Ra_{cr}$ . For Rayleigh numbers above  $Ra_{cr}$ , the basic double Hadley cell flow structure develops instabilities or stationary multicellular convective patterns. These effects have been studied primarily in laterally heated shallow cavities by, for example, Hart (1972, 1983) and Cormack et al. (1974). Garandet et al. (1992) solved analytically the MHD problem of the laterally heated rectangular cavity with a transverse magnetic field corresponding to the horizontal Bridgman technique. They showed that the core solution, dropping the nonlinear inertial term, was valid everywhere in the cavity except inside the boundary layer of thickness  $Ha^{-1/2}$  formed

along the cold wall. The flow recirculating region was studied separately by means of series expansions.

In the present work, the MHD natural convection flow in shallow cavities due to internal heating is studied analytically by means of matched asymptotic expansions and numerically by solving the full Navier-Stokes equations. The hydrodynamic part of the flow has already been solved by Daniels and Jones (1998), including the study of both conduction and convection heat transfer mechanisms. Their work is extended here for the case where the cavity contains an electrically conductive fluid which is subjected to a uniform transverse magnetic field. The geometry and the boundary conditions are similar to those of Daniels and Jones (1998). Thus, the shallow rectangular cavity consists of two adiabatic horizontal walls and two isothermal vertical walls, held at the same uniform temperature. The natural convection flow is driven by a uniform internal heating.

## 5.2 Geometry and mathematical formulation

Consider a shallow cavity of height  $h$  and large aspect ratio  $L$  where the flow is assumed to be steady, two-dimensional, subject to the Oberbeck-Boussinesq approximation for the fluid density variations due to temperature. The quasi-static (or low magnetic Reynolds number,  $R_m$ ) approximation is also assumed for the fluid magnetic induction-momentum connection. The magnetic Reynolds number ( $R_m = \mu \sigma L$ ) represents the ratio of advection to diffusion in the magnetic field. Sarris et al. (2006) have determined the limits of the validity of this approximation in natural convection flows. In laboratory MHD natural-convection flows, it is generally accepted that  $R_m \ll 1$ , which allows to ignore the solution of the magnetic induction equation. This results in a significant reduction of the equations to be solved and in reduction of the computational costs. Finally, Joule heating and viscous dissipation are also neglected. The flow configuration and boundary conditions are illustrated in Figure 5.1.

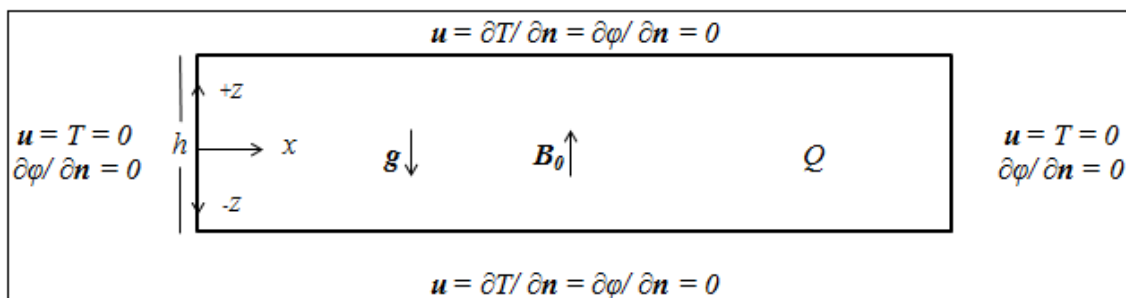


Fig. 5.1 Flow configuration and boundary conditions

Based on the above assumptions, the equations which describe the present 2-D steady-state, incompressible MHD flow ( $x, z$  are the Cartesian coordinates in the horizontal and vertical directions, respectively) are as follows:

$$\text{Mass continuity: } \frac{\partial u}{\partial x} + \frac{\partial w}{\partial z} = 0 \quad (5.1)$$

$$\text{x-Momentum: } \rho \left( u \frac{\partial u}{\partial x} + w \frac{\partial u}{\partial z} \right) = -\frac{\partial p}{\partial x} + \mu \left( \frac{\partial^2 u}{\partial x^2} + \frac{\partial^2 u}{\partial z^2} \right) - \sigma B_o^2 u \quad (5.2)$$

$$\text{z-Momentum: } \rho \left( u \frac{\partial w}{\partial x} + w \frac{\partial w}{\partial z} \right) = -\frac{\partial p}{\partial z} + \mu \left( \frac{\partial^2 w}{\partial x^2} + \frac{\partial^2 w}{\partial z^2} \right) + g\beta\rho\Delta T \quad (5.3)$$

$$\text{Energy equation: } \rho c_p \left( u \frac{\partial T}{\partial x} + w \frac{\partial T}{\partial z} \right) = k\nabla^2 T + Q \quad (5.4)$$

where,  $\rho$  is the mean density of the fluid,  $\mu$  its dynamic viscosity,  $c_p$  its specific heat at constant pressure,  $\beta$  its volumetric expansion coefficient,  $\sigma$  its electric conductivity, and  $Q$  is the constant volumetric heat generation rate.

By elimination of the pressure terms in equations 5.2 and 5.3, the vorticity and energy equations are derived. In fact, the streamfunction  $\psi$  describes the flow field. Taking the derivative of (5.2) and (5.3) with respect to  $z$  and  $x$ , respectively, the following equations are derived:

$$\frac{\partial u}{\partial z} \frac{\partial u}{\partial x} + u \frac{\partial^2 u}{\partial z \partial x} + \frac{\partial w}{\partial z} \frac{\partial u}{\partial z} + w \frac{\partial^2 u}{\partial z^2} = -\frac{1}{\rho} \frac{\partial^2 p}{\partial z \partial x} + \nu \frac{\partial^3 u}{\partial z \partial x^2} + \nu \frac{\partial^3 u}{\partial z^3} - \frac{\sigma B_o^2}{\rho} \frac{\partial u}{\partial z} \quad (5.5a)$$

$$\frac{\partial u}{\partial x} \frac{\partial w}{\partial x} + u \frac{\partial^2 w}{\partial x^2} + \frac{\partial w}{\partial x} \frac{\partial w}{\partial z} + w \frac{\partial^2 w}{\partial x \partial z} = -\frac{1}{\rho} \frac{\partial^2 p}{\partial x \partial z} + \nu \frac{\partial^3 w}{\partial x^3} + \nu \frac{\partial^3 w}{\partial x \partial z^2} + g\beta \frac{\partial T}{\partial x} \quad (5.6a)$$

$$(5.5a) \Rightarrow \underbrace{\frac{\partial u}{\partial z} \left( \frac{\partial u}{\partial x} + \frac{\partial w}{\partial z} \right)}_0 + u \frac{\partial^2 u}{\partial z \partial x} + w \frac{\partial^2 u}{\partial z^2} = -\frac{1}{\rho} \frac{\partial^2 p}{\partial z \partial x} + \nu \frac{\partial^3 u}{\partial z \partial x^2} + \nu \frac{\partial^3 u}{\partial z^3} - \frac{\sigma B_o^2}{\rho} \frac{\partial u}{\partial z} \Rightarrow$$

(continuity\_eq)

$$\Rightarrow u \frac{\partial^2 u}{\partial z \partial x} + w \frac{\partial^2 u}{\partial z^2} = -\frac{1}{\rho} \frac{\partial^2 p}{\partial z \partial x} + \nu \frac{\partial^3 u}{\partial z \partial x^2} + \nu \frac{\partial^3 u}{\partial z^3} - \frac{\sigma B_o^2}{\rho} \frac{\partial u}{\partial z} \quad (5.5b)$$

$$(5.6a) \Rightarrow \underbrace{\frac{\partial w}{\partial x} \left( \frac{\partial u}{\partial x} + \frac{\partial w}{\partial z} \right)}_0 + u \frac{\partial^2 w}{\partial x^2} + w \frac{\partial^2 w}{\partial x \partial z} = -\frac{1}{\rho} \frac{\partial^2 p}{\partial x \partial z} + \nu \frac{\partial^3 w}{\partial x^3} + \nu \frac{\partial^3 w}{\partial x \partial z^2} + g\beta \frac{\partial T}{\partial x} \Rightarrow$$

(continuity\_eq)

$$\Rightarrow u \frac{\partial^2 w}{\partial x^2} + w \frac{\partial^2 w}{\partial x \partial z} = -\frac{1}{\rho} \frac{\partial^2 p}{\partial x \partial z} + \nu \frac{\partial^3 w}{\partial x^3} + \nu \frac{\partial^3 w}{\partial x \partial z^2} + g\beta \frac{\partial T}{\partial x} \quad (5.6b)$$

Subtracting (5.6b) from (5.5b):

$$\begin{aligned}
u \left( \frac{\partial^2 u}{\partial z \partial x} - \frac{\partial^2 w}{\partial x^2} \right) + w \left( \frac{\partial^2 u}{\partial z^2} - \frac{\partial^2 w}{\partial x \partial z} \right) &= v \left( \frac{\partial^3 u}{\partial z \partial x^2} + \frac{\partial^3 u}{\partial z^3} - \frac{\partial^3 w}{\partial x^3} - \frac{\partial^3 w}{\partial x \partial z^2} \right) - \frac{\sigma B_o^2}{\rho} \frac{\partial u}{\partial z} - g\beta \frac{\partial T}{\partial x} \Rightarrow \\
u \frac{\partial}{\partial x} \left( \frac{\partial u}{\partial z} - \frac{\partial w}{\partial x} \right) + w \frac{\partial}{\partial z} \left( \frac{\partial u}{\partial z} - \frac{\partial w}{\partial x} \right) &= \\
v \left( \frac{\partial^3 u}{\partial x^2 \partial z} + \frac{\partial^3 u}{\partial z^3} - \frac{\partial^3 w}{\partial x^3} - \frac{\partial^3 w}{\partial z^2 \partial x} \right) - \frac{\sigma B_o^2}{\rho} \frac{\partial u}{\partial z} - g\beta \frac{\partial T}{\partial x} & \quad (5.7)
\end{aligned}$$

The streamfunction  $\psi(x,z)$  is related by definition to velocity components  $u$  and  $w$  through the following relationships:

$$u = \frac{\partial \psi}{\partial z} \quad \text{and} \quad w = -\frac{\partial \psi}{\partial x} \quad (5.8)$$

Substituting (5.8) in (5.7) it turns out that:

$$\begin{aligned}
\frac{\partial \psi}{\partial z} \frac{\partial}{\partial x} \left( \frac{\partial^2 \psi}{\partial z^2} + \frac{\partial^2 \psi}{\partial x^2} \right) - \frac{\partial \psi}{\partial x} \frac{\partial}{\partial z} \left( \frac{\partial^2 \psi}{\partial z^2} + \frac{\partial^2 \psi}{\partial x^2} \right) &= v \left( \frac{\partial^4 \psi}{\partial x^2 \partial z^2} + \frac{\partial^4 \psi}{\partial z^4} + \frac{\partial^4 \psi}{\partial x^4} + \frac{\partial^4 \psi}{\partial z^2 \partial x^2} \right) - \\
-\frac{\sigma B_o^2}{\rho} \frac{\partial^2 \psi}{\partial z^2} - g\beta \frac{\partial T}{\partial x} & \Rightarrow \\
\Rightarrow \frac{\partial \psi}{\partial z} \frac{\partial}{\partial x} \underbrace{\left( \frac{\partial^2 \psi}{\partial x^2} + \frac{\partial^2 \psi}{\partial z^2} \right)}_{\nabla^2 \psi} - \frac{\partial \psi}{\partial x} \frac{\partial}{\partial z} \underbrace{\left( \frac{\partial^2 \psi}{\partial x^2} + \frac{\partial^2 \psi}{\partial z^2} \right)}_{\nabla^2 \psi} &= v \underbrace{\left( \frac{\partial^4 \psi}{\partial x^4} + 2 \frac{\partial^4 \psi}{\partial x^2 \partial z^2} + \frac{\partial^4 \psi}{\partial z^4} \right)}_{\nabla^4 \psi} - \\
-\frac{\sigma B_o^2}{\rho} \frac{\partial^2 \psi}{\partial z^2} - g\beta \frac{\partial T}{\partial x} & \Rightarrow \\
\frac{\partial \psi}{\partial z} \frac{\partial (\nabla^2 \psi)}{\partial x} - \frac{\partial \psi}{\partial x} \frac{\partial (\nabla^2 \psi)}{\partial z} &= v \nabla^4 \psi - \frac{\sigma B_o^2}{\rho} \frac{\partial^2 \psi}{\partial z^2} - g\beta \frac{\partial T}{\partial x} \quad (5.9)
\end{aligned}$$

Substituting (5.8) in energy equation (5.4) it turns out that:

$$\frac{\partial \psi}{\partial z} \frac{\partial T}{\partial x} - \frac{\partial \psi}{\partial x} \frac{\partial T}{\partial z} = a \nabla^2 T + \frac{Q}{\rho c_p} \quad (5.10)$$

The streamfunction and energy equations can become dimensionless through the following dimensionless magnitudes:

$$X = \frac{x}{h}, \quad Z = \frac{z}{h}, \quad \Psi = \frac{\psi}{a}, \quad \Theta = \frac{T \rho c_p a}{h^2 Q} \quad (5.11)$$

Taking into account these dimensionless magnitudes it turns out that:

$$\begin{aligned}
(5.10) \Rightarrow \frac{ah^2 Q}{\rho c_p ah^2} \left( \frac{\partial \Psi}{\partial Z} \frac{\partial \Theta}{\partial X} \right) &= \frac{ah^2 Q}{\rho c_p ah^2} \nabla^2 \Theta + \frac{Q}{\rho c_p} \\
\Rightarrow \frac{\partial \Psi}{\partial Z} \frac{\partial \Theta}{\partial X} - \frac{\partial \Psi}{\partial X} \frac{\partial \Theta}{\partial Z} &= \nabla^2 \Theta + 1 \Rightarrow \boxed{\nabla^2 \Theta + 1 = \frac{\partial(\Theta, \Psi)}{\partial(X, Z)}} \quad (5.12)
\end{aligned}$$

$$\begin{aligned}
(5-9) &\Rightarrow \frac{a^2}{h^4} \left[ \frac{\partial \Psi}{\partial Z} \frac{\partial(\nabla^2 \Psi)}{\partial X} - \frac{\partial \Psi}{\partial X} \frac{\partial(\nabla^2 \Psi)}{\partial Z} \right] = \frac{va}{h^4} \nabla^4 \Psi - \frac{\sigma B_o^2 a}{\rho h^2} \frac{\partial^2 \Psi}{\partial Z^2} - g\beta \frac{h^2 Q}{\rho c_p a h} \frac{\partial \Theta}{\partial X} \Rightarrow \\
&\Rightarrow \left( \frac{a}{v} \right) \left[ \frac{\partial \Psi}{\partial Z} \frac{\partial(\nabla^2 \Psi)}{\partial X} - \frac{\partial \Psi}{\partial X} \frac{\partial(\nabla^2 \Psi)}{\partial Z} \right] = \nabla^4 \Psi - \underbrace{\left( \frac{\sigma B_o^2 h^2}{\rho v} \right)}_{Ha^2} \frac{\partial^2 \Psi}{\partial Z^2} - \underbrace{\left( \frac{g\beta Q h^5}{\rho c_p v a^2} \right)}_{Ra} \frac{\partial \Theta}{\partial X} \Rightarrow \\
&\quad \Rightarrow \text{Pr}^{-1} \frac{\partial(\nabla^2 \Psi, \Psi)}{\partial(X, Z)} = \nabla^4 \Psi - Ha^2 \frac{\partial^2 \Psi}{\partial Z^2} - Ra \frac{\partial \Theta}{\partial X} \Rightarrow \\
&\boxed{\nabla^4 \Psi = \text{Pr}^{-1} \frac{\partial(\nabla^2 \Psi, \Psi)}{\partial(X, Z)} + Ha^2 \frac{\partial^2 \Psi}{\partial Z^2} + Ra \frac{\partial \Theta}{\partial X}} \quad (5.13)
\end{aligned}$$

where  $\text{Pr} = \frac{\nu}{a}$  is the Prandtl number of the fluid,  $Ra = g\beta Q h^5 / \rho c_p v a^2$  is the Rayleigh number and  $Ha^2 = \sigma B_o^2 h^2 / \rho v$  is the Hartmann number. In fact, Pr is the ratio of momentum diffusivity to thermal diffusivity. Ra is a dimensionless number associated with buoyancy driven flow (also known as free or natural convection). When the Rayleigh number is below the critical value for a specific fluid, heat transfer is primarily in the form of conduction; when it exceeds the critical value, heat transfer is primarily in the form of convection. Furthermore, Ra is defined as the product of the Grashof number, Gr, describing the relationship between buoyancy and viscous forces in a fluid, and the Prandtl number of the fluid, i.e.  $Ra = Gr \text{Pr}$ . Hence, the Rayleigh number itself may also be viewed as the ratio of buoyancy and viscous forces times the ratio of momentum and thermal diffusivities. Finally, the Hartmann number (Ha) is the ratio of electromagnetic to viscous forces.

Symbolizing the dimensionless coordinates, the dimensionless streamfunction and the dimensionless temperature as  $x$ ,  $z$ ,  $\psi$  and  $T$ , respectively, the dimensionless equations (5.12) and (5.13) result in:

$$\boxed{\nabla^4 \psi = \text{Pr}^{-1} \frac{\partial(\nabla^2 \psi, \psi)}{\partial(x, z)} + Ha^2 \frac{\partial^2 \psi}{\partial z^2} + Ra \frac{\partial T}{\partial x}} \quad (5.14a)$$

Or

$$\frac{\partial^4 \psi}{\partial x^4} + 2 \frac{\partial^4 \psi}{\partial x^2 \partial z^2} + \frac{\partial^4 \psi}{\partial z^4} = \text{Pr}^{-1} \left[ \frac{\partial \psi}{\partial z} \frac{\partial(\nabla^2 \psi)}{\partial x} - \frac{\partial \psi}{\partial x} \frac{\partial(\nabla^2 \psi)}{\partial z} \right] + Ha^2 \frac{\partial^2 \psi}{\partial z^2} + Ra \frac{\partial T}{\partial x} \quad (5.14b)$$

$$\boxed{\nabla^2 T + 1 = \frac{\partial(T, \psi)}{\partial(x, z)}} \quad (5.15a)$$

$$\frac{\partial^2 T}{\partial x^2} + \frac{\partial^2 T}{\partial z^2} + 1 = \frac{\partial \psi}{\partial z} \frac{\partial T}{\partial x} - \frac{\partial \psi}{\partial x} \frac{\partial T}{\partial z} \quad (5.15b)$$

The boundary conditions at the horizontal walls are

$$\psi(x, 1/2) = \psi(x, -1/2) = 0 \quad (5.16)$$

$$\frac{\partial \psi}{\partial z}(x, 1/2) = \frac{\partial \psi}{\partial z}(x, -1/2) = 0 \quad (5.17)$$

$$\frac{\partial T}{\partial z}(x, 1/2) = \frac{\partial T}{\partial z}(x, -1/2) = 0 \quad (5.18)$$

On the other hand, the boundary conditions at the vertical walls are

$$\psi(0, z) = \psi(L, z) = 0 \quad (5.19)$$

$$\frac{\partial \psi}{\partial x}(0, z) = \frac{\partial \psi}{\partial x}(L, z) = 0 \quad (5.20)$$

$$T(0, z) = T(L, z) = 0 \quad (5.21)$$

The symmetric nature of the flow and temperature fields with respect to the middle plane of the cavity, which is not affected by the Lorentz force, can also be described by the relations:

$$\psi(x, z) = -\psi(L - x, z) \quad (5.22)$$

$$T(x, z) = T(L - x, z) \quad (5.23)$$

Daniels and Jones (1998) discussed successively the order of magnitude of the Rayleigh number above which convection effects are significant in this flow. They showed that when Ra is of order of  $L^{-1}$ , the temperature field due to conduction is

$$T = \frac{1}{2}x(L - x) \quad (5.24)$$

no longer is valid. They introduced the scaled Rayleigh number  $R_s = Ra \cdot L$ , which is of order of one as  $L \rightarrow \infty$ , a dimensionless parameter that is also used here. Moreover, from Eq. (5.14) follows that the magnitude of  $Ha^2$  is of order one, so that the magnetic field effects are competitive to the buoyancy effects.

### 5.3 Analytical solutions with matched asymptotic expansions

The main parameter of the present problem is  $\varepsilon \equiv L^{-1} \ll 1$ , where  $L$  is the aspect ratio of the cavity which is considered to be very large. The core flow covers most of the cavity and thus its solution depends on the length scales:

$$\xi = x/L, z = z \quad (5.25)$$

The streamfunction and the temperature fields can be expanded as  $L \rightarrow \infty$  with respect to  $\xi, z$  in the form:



$$\begin{aligned}\psi &= \varepsilon^0 \psi_0(\xi, z) + \varepsilon^1 \psi_1(\xi, z) + \varepsilon^2 \psi_2(\xi, z) + \dots \Rightarrow \\ \Rightarrow \psi &= \psi_0(\xi, z) + L^{-1} \psi_1(\xi, z) + L^{-2} \psi_2(\xi, z) + \dots\end{aligned}\quad (5.26)$$

$$\begin{aligned}T &= \varepsilon^{-2} T_0(\xi, z) + \varepsilon^{-1} T_1(\xi, z) + \varepsilon^0 T_2(\xi, z) + \varepsilon^1 T_3(\xi, z) + \dots \Rightarrow \\ T &= L^2 T_0(\xi, z) + L T_1(\xi, z) + T_2(\xi, z) + L^{-1} T_3(\xi, z) + \dots\end{aligned}\quad (5.27)$$

These expansions are substituted into the flow and energy equations (Eqs. 5.14a and 5.15a) and their boundary conditions (Eqs. 5.16 to 5.21) to obtain a system of coupled equations for the streamfunction and temperature for every order of magnitude of  $L$ . From the energy equation (5.15a) at order  $L^2$ ,  $L$  and  $1$  it is obtained, respectively:

$$\frac{\partial^2 T_0}{\partial z^2} = 0 \quad (5.28)$$

$$\frac{\partial^2 T_1}{\partial z^2} = \frac{\partial T_0}{\partial \xi} \frac{\partial \psi_0}{\partial z} \quad (5.29)$$

$$\frac{\partial^2 T_2}{\partial z^2} = -1 - \frac{\partial^2 T_0}{\partial \xi^2} + \frac{\partial T_1}{\partial \xi} \frac{\partial \psi_0}{\partial z} + \frac{\partial T_0}{\partial \xi} \frac{\partial \psi_1}{\partial z} - \frac{\partial T_1}{\partial z} \frac{\partial \psi_0}{\partial \xi} \quad (5.30)$$

From Eq. (5.14a) at order  $1$  and  $L^{-1}$  it is obtained, respectively:

$$\frac{\partial^4 \psi_0}{\partial z^4} - Ha^2 \frac{\partial^2 \psi_0}{\partial z^2} = R_s \frac{\partial T_0}{\partial \xi} \quad (5.31)$$

$$\frac{\partial^4 \psi_1}{\partial z^4} - Ha^2 \frac{\partial^2 \psi_1}{\partial z^2} = Pr^{-1} \left( \frac{\partial^3 \psi_0}{\partial \xi \partial z^2} \frac{\partial \psi_0}{\partial z} - \frac{\partial^3 \psi_0}{\partial z^3} \frac{\partial \psi_0}{\partial \xi} \right) + R_s \frac{\partial T_1}{\partial \xi} \quad (5.32)$$

The solution of Eq. (5.28) with the adiabatic boundary conditions  $\partial T_0 / \partial z = 0$  at  $z = \pm 0.5$  is:

$$T_0 = \theta_0(\xi) \quad (5.33)$$

where  $\theta_0$  is a function of  $\xi$ , independent of  $z$ . The solution of  $\psi_0$  can be calculated from Eq. (5.31) with the boundary conditions  $\partial \psi_0 / \partial z = 0$  at  $z = \pm 0.5$  as:

$$\psi_0 = \frac{R_s}{Ha^2} \theta_0' f(z) \quad (5.34)$$

where

$$f(z) = \frac{1}{2} \left( \frac{\cosh Haz}{Ha \sinh \frac{Ha}{2}} - \frac{\coth \frac{Ha}{2}}{Ha} + \frac{1}{4} - z^2 \right) \quad (5.35)$$

Based on  $\psi_0$  and  $T_0$ , the solution of Eq. (5.29) gives for  $T_1$ :

$$T_1(\xi, z) = \frac{R_s}{Ha^2} (\theta_0')^2 \frac{1}{2} \underbrace{\left( \frac{\sinh Haz}{Ha^2 \sinh \frac{Ha}{2}} - \frac{z \coth \frac{Ha}{2}}{Ha} + \frac{z}{4} - \frac{z^3}{3} \right)}_{g(z)} + \theta_1(\xi) \quad (5.36)$$

$$\text{where: } g(z) = \frac{1}{2} \left( \frac{\sinh Haz}{Ha^2 \sinh \frac{Ha}{2}} - \frac{z \coth \frac{Ha}{2}}{Ha} + \frac{z}{4} - \frac{z^3}{3} \right)$$

and  $\theta_1$  is an arbitrary function of  $\xi$  that must be determined.

From Eq. (5.32) with the boundary conditions  $\psi_1 = \frac{\partial \psi_1}{\partial z} = 0$  at  $z = \pm \frac{1}{2}$  and

$\psi_1 = \frac{\partial \psi_1}{\partial \xi} = 0$  at  $\xi = 0, 1$  the solution of  $\psi_1$  is

$$\psi_1 = \frac{R_s^2}{Ha^2} \theta_0' \theta_0'' (G_1 + \text{Pr}^{-1} Ha G_2) + \frac{R_s}{Ha^2} \theta_1' \quad (5.37)$$

where

$$G_1 = \frac{z^3}{3} - \frac{z}{4} + \frac{2z}{Ha^2} + \frac{z}{Ha} \coth \frac{Ha}{2} + \frac{z}{2Ha} \frac{\cosh(Haz)}{\sinh \left[ \frac{Ha}{2} \right]} - \frac{1}{4Ha^2} \frac{\sinh(Haz)}{\sinh \left[ \frac{Ha}{2} \right]} \quad (5.38)$$

$$G_2 = \left( \frac{z^3}{12} - \frac{z}{16} - \frac{5z}{8Ha^2} + \frac{z}{4Ha} \coth \frac{Ha}{2} \right) \frac{\cosh(Haz)}{\sinh \left[ \frac{Ha}{2} \right]} \cdot \left( \frac{z^2}{8Ha} + \frac{3}{16Ha^3} + \frac{1}{32Ha} - \frac{\coth \frac{Ha}{2}}{8Ha^2} \right) \frac{\sinh(Haz)}{\sinh \left[ \frac{Ha}{2} \right]} \quad (5.39)$$

From Eq. (5.30) for the energy at order one, integration in  $z$  and the use of boundary conditions  $\frac{\partial T_2}{\partial z} = 0$  at  $z = \pm \frac{1}{2}$  it appears that the only consistent solution has

to satisfy the following equation for  $\theta_0$ :

$$\theta_0'' + a_m R_1^2 (\theta_0')^2 \theta_0'' + 1 = 0 \quad (5.40)$$

where

$$\alpha_m = \frac{3}{Ha^4} \int_{-\frac{1}{2}}^{\frac{1}{2}} f(z)^2 dz \Rightarrow \alpha_m = \frac{3}{Ha^4} \int_{-\frac{1}{2}}^{\frac{1}{2}} \frac{1}{4} \left( \frac{\cosh Haz}{Ha \sinh \frac{Ha}{2}} - \frac{\coth \frac{Ha}{2}}{Ha} + \frac{1}{4} - z^2 \right)^2 dz \quad (5.41)$$

The limit of  $a_m$  when  $Ha \rightarrow 0$  is a good test in order to check the equivalence of the current solutions with those obtained by Daniels and Jones (1998), therefore

$$\lim_{Ha \rightarrow 0} a_m = \frac{1}{120960} \quad (5.42)$$

which is exactly the result without the magnetic field, as provided by Daniels and Jones (1998). For  $\theta_0$ , the end wall boundary conditions indicate that:

$$\theta_0 = 0 \text{ at } \xi = 0, 1 \quad (5.43)$$

The first integration of Eq. (5.40), taking into account the symmetry condition of the solution, gives:

$$\theta_0' = a_m^{-1/2} R_s^{-1} \left[ F_m^+(\xi) + F_m^-(\xi) \right] \quad (5.44)$$

where

$$F_m^\pm(\xi) = \left\{ \frac{3}{2} a_m^{1/2} R_s \left( \frac{1}{2} - \xi \right) \pm \left[ 1 + \frac{9}{4} a_m R_s^2 \left( \xi - \frac{1}{2} \right)^2 \right]^{1/2} \right\}^{1/3} \quad (5.45)$$

$$\text{Additionally, } \sinh y_m = \frac{3}{2} a_m^{1/2} R_s \left( \xi - \frac{1}{2} \right) \Leftrightarrow y_m = \sinh^{-1} \left[ \frac{3}{2} a_m^{1/2} R_s \left( \xi - \frac{1}{2} \right) \right].$$

Using the term  $y_m$ , with a further integration and using the boundary conditions of Eq. (5.44) gives:

$$\theta_0 = a_m^{-1} R_s^{-2} \left( \cosh \frac{2}{3} y_m - \frac{1}{2} \cosh \frac{4}{3} y_m - \cosh \frac{2}{3} y_{m,0} + \frac{1}{2} \cosh \frac{4}{3} y_{m,0} \right) \quad (5.46)$$

where

$$y_{m,0} = \sinh^{-1} \left( \frac{3}{4} a_m^{1/2} R_s \right) \quad (5.47)$$

From Eq. (5.31) the core streamfunction is given by

$$\psi_0 = -2 \frac{a_m^{-1/2} f(z)}{Ha^2} \sinh \frac{1}{3} y_m \quad (5.48)$$

and the vertical velocity in the core region is given by

$$w_{an} = -\frac{\partial \psi_0}{\partial \xi} = \frac{R_s f(z)}{Ha^2 \left(1 + 4 \sinh^2 \frac{1}{3} y_m\right)} \quad (5.49)$$

The core solution must be continued one stage further in order to determine the unknown function  $\theta_1(\xi)$  which arises in the solution of  $T_1$  and is needed also for the determination of  $\psi_1$ . Thus, the solution of Eq. (5.30) for  $T_2$  provides the way of determining  $\theta_1(\xi)$ . Solving for  $T_2$  and using the symmetry condition of Eqs. (5.22, 5.23), Daniels and Jones (1998), proved for the hydrodynamic case that the only possible solution is  $\theta_1(\xi) = C$ , where  $C$  is a constant related to the temperature of the end walls. Using the same type of analysis, one can prove that the same value for  $\theta_1(\xi)$  is not valid for the MHD case. Finally, the core solution for the flow and temperature fields has been obtained in the form

$$\begin{aligned} \psi &= \psi_0(\xi, z) + L^{-1} \psi_1(\xi, z) + L^{-2} \psi_2(\xi, z) + \dots \Rightarrow \\ \Rightarrow \psi &= \frac{R_s}{Ha^2} \theta_0' f + L^{-1} \left[ \frac{R_s^2}{Ha^4} \theta_0' \theta_0'' (G_1 + Pr^{-1} G_2) \right] + \dots \end{aligned} \quad (5.50)$$

$$\begin{aligned} T &= L^2 T_0(\xi, z) + L T_1(\xi, z) + T_2(\xi, z) + L^{-1} T_3(\xi, z) + \dots \Rightarrow \\ \Rightarrow T &= L^2 \theta_0 + L \left[ \frac{R_s}{Ha^2} (\theta_0')^2 g + C \right] + \dots \end{aligned} \quad (5.51)$$

Daniels and Jones (1998) concluded that for the hydrodynamic limit  $C$  is determined as  $C \approx 2.2 \times 10^{-7} R_s^2$ ,  $R_s \rightarrow 0$ . This approximation corresponds to the fact that the flow near the end walls is dominated by conduction.

The numerical simulations showed that the aforementioned function  $C$ , which serves in order to correct the core solution of the temperature field, must be revised in order to be also valid for larger Rayleigh number values. However, a relationship which describes the temperature field due to conduction, when  $R_s \rightarrow 0$ , already exists (Eq. 5.24). Thus, the usage of  $C$  according to Daniels and Jones (1998) is not adequate in the present analysis since it is valid only for  $R_s \rightarrow 0$ , i.e. for pure conduction heat transfer. Furthermore, concerning the magnetohydrodynamic case, the contribution of the Lorentz force in the value of  $C$  must be considered. Therefore, numerical simulations were performed in order to assess the value of  $C$  for a range of  $Ra$ ,  $Ha$  and  $Pr$  values.

## 5.4 Numerical simulation of MHD natural convection in an internally heated horizontal shallow cavity with OpenFOAM CFD library

Natural-convection heat transfer of electrically conducting fluids such as liquid metals in enclosures has been the subject of several works as already mentioned in section 5.1. The purpose of the numerical models used in the majority of the studies was to determine the influence of the Grashof, Reynolds, Prandtl or Hartmann numbers on the flow and heat transfer. A common simplification in all these studies was the use of the low- $R_m$  (or quasi-static) approximation (Moreau, 1990, Davidson, 2001) instead of the full magnetic induction equations. It is reminded that the dimensionless magnetic Reynolds number  $R_m$  of the flow represents the ratio of advection to diffusion in the magnetic field. At the limit when  $R_m \rightarrow 0$ , magnetic diffusion dominates over convection, thus the fluid motion has no influence on the magnetic field distribution. Then, the latter can be calculated as if the fluid were at rest and the Lorentz force of the magnetic field can be evaluated through a damping term, which includes only the velocity and the external magnetic field. The magnitude of  $R_m$  in laboratory-scale experiments (e.g. molten metals) does not exceed the value of  $10^{-2}$ , and in industrial applications the value of several tenths, Moreau (1990).

It is generally accepted in MHD natural-convection studies that  $R_m \ll 1$ , which allows overcoming the solution of the magnetic induction equation, thus resulting in a significant reduction of the equations to be solved and in reduction of the computational cost. Most works adopted the low magnetic Reynolds number approximation (low- $R_m$  model) for the simulations, without any further investigation of the validity of the model for the specific configuration and the range of operational parameters used. Sarris et al. (2006) have assessed the limits of validity of the low- $R_m$  model for natural convection flows in a square cavity.

Numerical simulations of buoyancy-driven flows in cubic enclosures subject to a static homogeneous magnetic field (Ozoe & Okada, 1989, Shigemitsu et al., 2003, Tagawa & Ozoe, 1997) have led to some interesting results. However, and despite their limited physical significance, investigations of two-dimensional flows, because of their simplicity, permit us to analyze in more detail the dependence of the flow on parameters of the problem which are varied in a relatively broad range.

### 5.4.1 The Low- $R_m$ Approximation

As it has already been mentioned, Ohm's law can determine the electric current density.

$$\mathbf{J} = \sigma(\mathbf{E} + \mathbf{U} \times \mathbf{B}) \quad (3.8)$$

Assuming negligible perturbations for the electric and magnetic fields, Eq. (3.8) can be written as

$$\mathbf{J} = \sigma(\mathbf{E}_0 + \mathbf{U} \times \mathbf{B}_0) \quad (5.52)$$

where  $\mathbf{E}_0$  and  $\mathbf{B}_0$  are the electric and magnetic fields, respectively, when the fluid is at rest. Moreover, due to the neglecting of displacement current, since  $\frac{\partial D}{\partial t} \ll \mathbf{J}$ , the electric charge conservation  $\nabla \cdot \mathbf{J} = 0$  implies that  $\mathbf{E}_0$  is irrotational. Therefore,  $\mathbf{E}_0$  can be expressed as  $-\nabla \cdot \phi$ , where  $\phi$  is the electrostatic potential. Thus, for a two-dimensional cavity without externally supplied electric field, the divergence of Ohm's law gives

$$\begin{aligned} \nabla \cdot \mathbf{J} &= \nabla \cdot [\sigma(\mathbf{E}_0 + \mathbf{U} \times \mathbf{B}_0)] \Rightarrow 0 = \nabla \cdot \mathbf{E}_0 + \nabla \cdot (\mathbf{U} \times \mathbf{B}_0) \Rightarrow \\ \Rightarrow \nabla^2 \phi &= \nabla \cdot (\mathbf{U} \times \mathbf{B}_0) = \mathbf{B}_0 \cdot \left( \frac{\partial \mathbf{v}_x}{\partial y} - \frac{\partial \mathbf{v}_y}{\partial x} \right) = 0 \end{aligned} \quad (5.53)$$

where  $\mathbf{v}_x$  and  $\mathbf{v}_y$  are the fluid velocities in the x- and y-directions, respectively.

As pointed out by Garandet et al. (1992), the harmonic equation for the electric potential ( $\nabla^2 \phi = 0$ ) in the case of enclosures with electrically insulating boundaries has a unique constant solution and thus the electric field vanishes everywhere. Then, the associated Lorentz force can be reduced to  $-\sigma \mathbf{B}_0^2 \mathbf{v}_\perp$ , where  $\mathbf{v}_\perp$  is the velocity component perpendicular to the direction of  $\mathbf{B}_0$ .

Considering the above, the momentum equation takes the following form:

$$\rho \left( \frac{\partial \mathbf{U}}{\partial t} + \mathbf{U} \cdot \nabla \mathbf{U} \right) = -\nabla p + \mu \nabla^2 \mathbf{U} - \rho \mathbf{g} \beta \Delta T - \sigma \mathbf{B}_0^2 \mathbf{v}_\perp \quad (5.54)$$

This form of the momentum equation, called *low- $R_m$  approximation*, is commonly used in MHD natural-convection problems. The advantage of using this reduced model instead of the full MHD equations is mainly the reduced number of

equations required to be solved, resulting in less computational cost. The errors in the predictions based on this model will be presented and discussed below.

#### 5.4.2 Validation of the low- $R_m$ and full MHD models applied in OpenFOAM

First of all, in order to validate the low- $R_m$  model applied in OpenFOAM, the results of Al-Najem et al. (1998) were compared with the present results by using OpenFOAM. Al-Najem et al. (1998) studied numerically the laminar natural convection in a tilted enclosure filled with an electrically conducting fluid. The horizontal walls of the cavity were perfectly insulated, while the vertical ones were isothermal with the left wall at high temperature  $T_H$  and the right one at low temperature  $T_C$ . The fluid was permeated by a uniform external magnetic field. The resulting convective flow is governed by the combined mechanism of the driving buoyancy forces and the electromagnetic retarding forces. The magnetic Reynolds number is assumed to be small so that the induced magnetic field produced by the motion of the electrically conducting fluid is negligible compared to the applied magnetic field  $B_0$ . The flow is considered laminar and incompressible, with constant physical properties. The density variation is implemented only in the buoyancy force term according to the Boussinesq approximation. Pressure work, Joule heating and viscous dissipation are considered negligible. The flow configuration is illustrated in Fig. 5.2.

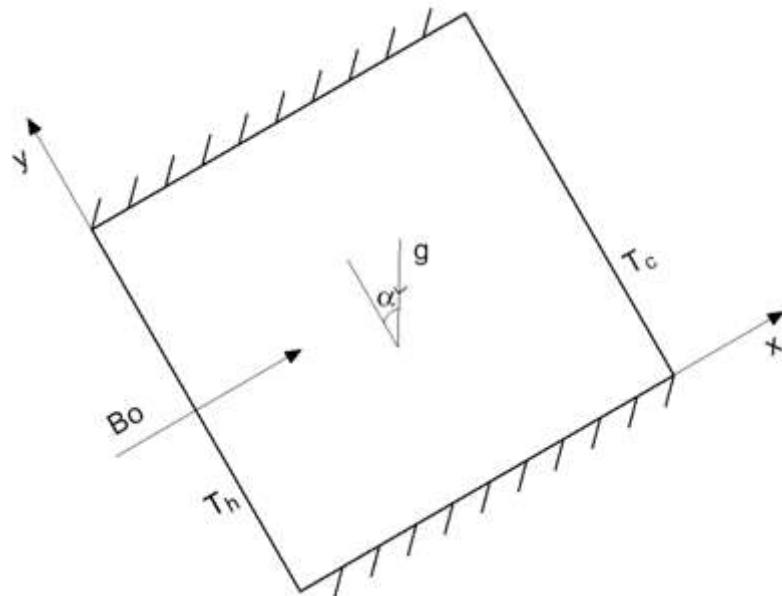


*Fig. 5.2 Flow configuration of Al-Najem et al (1998)*

The system of governing equations in dimensionless form is as follows:

$$\nabla \cdot \mathbf{U} = 0 \quad (5.55)$$

$$(\mathbf{U} \cdot \nabla) \mathbf{U} = -\nabla p + \nabla^2 \mathbf{U} + Gr \Theta + \frac{Ha^2}{R_m} (\mathbf{B} \cdot \nabla) \mathbf{B} \quad (5.56)$$

$$(\mathbf{U} \cdot \nabla) \Theta = \frac{1}{Pr} \nabla^2 \Theta \quad (5.57)$$

$$(\mathbf{U} \cdot \nabla) \mathbf{B} = \frac{1}{R_m} \nabla^2 \mathbf{B} + (\mathbf{B} \cdot \nabla) \mathbf{U} \quad (5.58)$$

$$\mathbf{J} = \nabla \times \mathbf{B} = R_m (\mathbf{U} \times \mathbf{B}) \quad (5.59)$$

$$\nabla \cdot \mathbf{B} = 0 \quad (5.60)$$

The dimensionless parameters of the problem are the Grashof number ( $Gr = g\beta\Delta Th^3/\nu^2$ ), the Prandtl number ( $Pr = \nu/a$ ), the magnetic Reynolds number ( $R_m = \sigma\mu\nu$ ) and the Hartmann number ( $Ha = B_0 h (\sigma/\rho\nu)^{-1/2}$ ).

In the case of the low- $R_m$  model, the magnetic induction equation (Eq.5.58) is dropped. Then, the momentum equation (5.56) may be written as

$$(\mathbf{U} \cdot \nabla) \mathbf{U} = -\nabla p + \nabla^2 \mathbf{U} + Gr \Theta - Ha^2 |\mathbf{B}|^2 \mathbf{U}_\perp \quad (5.61)$$

Furthermore, the current density is obtained from the modified Ohm's law

$$\mathbf{J} = \sigma(-\nabla\varphi + \mathbf{U} \times \mathbf{B}) \quad (5.62)$$

while the electrostatic potential is obtained from Eq. 5.63

$$\nabla^2 \varphi = \nabla \cdot (\mathbf{U} \times \mathbf{B}_0) \quad (5.63)$$

The non-dimensional quantities were derived using the enclosure height ( $h$ ) as reference length, and the quantity  $\nu/h$  as reference velocity:

$$\begin{aligned} \tilde{x} &= \frac{x}{h} & \tilde{y} &= \frac{y}{h} & \tilde{p} &= \frac{p_{tot} h^2}{\rho \nu^2} \\ \tilde{\mathbf{U}} &= \frac{\mathbf{U}}{\nu/h} & \tilde{\mathbf{B}} &= \frac{\mathbf{B}}{B_0} & \tilde{\mathbf{J}} &= \frac{\mu h}{B_0} \mathbf{J} \\ \Theta &= \frac{T - T_0}{\Delta T} & \tilde{\varphi} &= \frac{\varphi}{B_0 \nu} \end{aligned} \quad (5.64)$$

where  $p_{tot}$  is the total pressure which includes both the mechanical and magnetic pressure. Then, the circumflex is neglected in order to simplify our study.

The present OpenFOAM-based numerical model used the above low- $R_m$  model equations together with the corresponding boundary conditions and a finite volume method. Specifically, the coupling between the momentum (Eq. 5.56) and continuity (Eq. 5.55) equations was performed by using PISO (Weller, 2004a&b, Jasak, 1996,



Weller et al., 1998). The nonuniform grid of 41x41 was adequate in this study as shown by Al-Najem et al. (1998). Further increase in the number of grids produced essentially the same results. For the present validation only the case with an enclosure angle inclination equal to 0 was selected. The flow configuration and the boundary conditions of the problem are illustrated in Fig. 5.3.

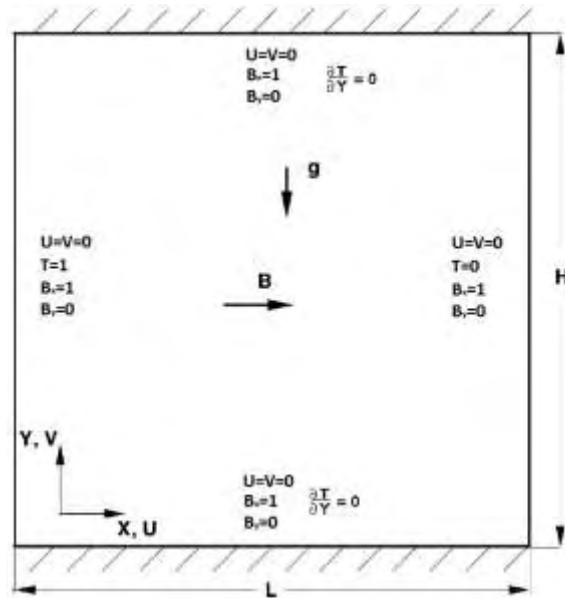


**Fig. 5.3** Flow configuration and boundary conditions of the present model

The energy equation (Eq. 5.57) was handled according to the instructions provided in the Internet ([http://openfoamwiki.net/index.php/How to add temperature to icoFoam](http://openfoamwiki.net/index.php/How_to_add_temperature_to_icoFoam)). Concerning the numerical schemes, which were used in the simulations, central discretization was used for the laplacian and grad terms and gamma differencing for the convection terms, Jasac (1996). A finer distribution for the grid nodes close to the walls was used in both directions in order to resolve better the flow and Hartmann boundary layers and to predict efficiently the heat transfer at the side walls. Convergence was established when the sum of the absolute relative errors for each solved quantity in the entire flow field was less than  $10^{-7}$ .

In general, the results of the present low- $R_m$  model were in good overall agreement with those of Al-Najem et al. (1998) and Sarris et al. (2006). Specifically, streamfunction contours and isotherms at the middle of a vertical cavity for a liquid with  $Pr = 0.733$ ,  $Gr = 10^6$  and for various values of Hartmann were compared in Figs. 5.4 and 5.5. The application of a transverse magnetic field results in a force opposing the fluid motion. This magnetic force becomes greater as the strength of the magnetic field

increases. Moreover, the conduction heat transfer mechanism becomes dominant as the Hartmann number is increased.

For a better comparison between the results of low- $R_m$  MHD model of Al-Najem et al. (1998) and those of the OpenFOAM CFD library, velocity profiles at the cavity mid-section for the case with  $Ha=10$  and  $Gr=10^4$  are shown in Fig. 5.6. The present results are in good agreement with those of the Al-Najem et al. (1998).

In addition, the same flow was computed applying the full MHD model with an  $R_m$  value equal to  $10^3$ . The results are compared with those of Sarris et al. (2006) in Fig.5.7 showing a good agreement. In Fig. 5.8, the comparison of the mid-section velocity profile between the low- $R_m$  and full MHD models applied in OpenFOAM at  $Ha = 10$  and  $Gr=10^4$  is shown. The full magnetic induction model with  $R_m = 10^3$  predicts approximately 12.8% higher mid-section maximum velocity at  $y=0.06$  where the maximum difference is located. Sarris et al. (2006) showed that there is an increasing difference between the solutions of the full MHD equations and low- $R_m$  approximation with increasing the Hartmann number. This difference decreases for higher Grashof numbers, while for low Prandtl numbers like those of liquid metals, the difference increases. Moreover, Figs. 5.9 and 5.10 present temperature and velocity profiles at the mid-section of the cavity for different values of  $Ha$  at  $Gr=10^6$ , using the low- $R_m$  model, showing the influence of the Lorentz forces on retarding the fluid flow.

Finally, in order to demonstrate the validity of the low- $R_m$  model, the values of the horizontal component of the dimensionless velocity  $U_c$  for both the model of Al-Najem et al. (1998) and that of the OpenFOAM library, for several values of  $y$ , are illustrated in Table 5.1. In addition,  $U_c$  values for both the full MHD model by Sarris et al (2006) and that of the OpenFOAM are presented in Table 5.2. As a last test, the effect of the choice of the magnetic induction model on fluid motion is demonstrated in Table 5.3. For all the above cases discussed in this paragraph, the case  $Pr = 0.733$ ,  $Gr = 10^4$  and  $Ha = 10$  was considered as a reference study. The last column in all Tables corresponds to the relative error between the two models studied in each Table. It is noticed that overall the error in all occasions is small.

**Table 5.1** Comparison of the present low- $R_m$  model calculations with those of Al-Najem et al. (1998) for the case of  $Pr=0.733$ ,  $Gr = 10^4$  and  $Ha=10$

y	Al-Najem et al. (1998)	low- $R_m$ (OpenFOAM)	$e = 100 \cdot \frac{U_c(Al - Najem) - U_c(OpenFOAM)}{U_c(Al - Najem)}$
0	0	0	0.000
0.06	-0.085	-0.086	1.176
0.11	-0.125	-0.122	2.400
0.175	-0.140	-0.135	3.571
0.25	-0.126	-0.121	3.968
0.325	-0.095	-0.098	3.158
0.412	-0.050	-0.048	4.000
0.56	0.034	0.033	2.941
0.63	0.075	0.074	1.333
0.72	0.110	0.110	0.000
0.83	0.135	0.135	0.000
0.92	0.105	0.104	0.952
1	0	0	0.000

**Table 5.2** Comparison of the present full MHD model calculations with those of Sarris et al. (2006) for the case of  $Pr=0.733$ ,  $Gr = 10^4$  and  $Ha=10$ .

y	Sarris et al. (2006)	full MHD (OpenFOAM)	$e = 100 \cdot \frac{U_c(Sarris) - U_c(OpenFOAM)}{U_c(Sarris)}$
0	0	0	0
0.06	-0.095	-0.097	2.105
0.11	-0.139	-0.137	1.439
0.175	-0.150	-0.151	0.667
0.25	-0.140	-0.135	3.571
0.325	-0.100	-0.099	1.000
0.412	-0.050	-0.048	4.000
0.56	0.037	0.036	2.703
0.63	0.078	0.077	1.282
0.72	0.127	0.123	3.150
0.83	0.155	0.151	2.581
0.92	0.115	0.116	0.870
1	0	0	0

**Table 5.3** Comparison of the full MHD calculations with those of low- $R_m$  applied in OpenFOAM for the case of  $Pr=0.733$ ,  $Gr = 10^4$  and  $Ha=10$ .

$y$	low- $R_m$ (OpenFOAM)	full MHD (OpenFOAM)	$e = \frac{ U_{c[low-R_m]} - U_{c[fullMHD]} }{U_{c[low-R_m]}} \times 100\%$
0	0	0	0
0.06	-0.086	-0.097	12.791
0.11	-0.122	-0.137	12.295
0.175	-0.135	-0.151	11.852
0.25	-0.121	-0.135	11.570
0.325	-0.098	-0.099	1.020
0.412	-0.048	-0.048	0.000
0.56	0.033	0.036	9.091
0.63	0.074	0.077	4.054
0.72	0.110	0.123	11.818
0.83	0.135	0.151	11.852
0.92	0.104	0.116	12.539
1	0	0	0

### 5.5.3 Numerical study of the two-dimensional MHD natural convection flow in an internally heated horizontal shallow cavity

The next step was to implement the low- $R_m$  model for the case of the two dimensional MHD natural convection flow in an internally heated horizontal shallow cavity which was analyzed in detail in the beginning of this chapter.

The flow configuration and the boundary conditions are shown in Fig. 5.1 while the grid which was used (one quarter because of symmetry) is shown in Fig. 5.11.

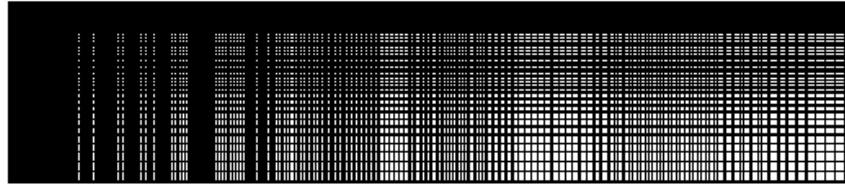


Fig. 5.11 One fourth of the grid used for the 2-D MHD natural convection flow

More specifically, the system of dimensionless governing equations is:

$$\nabla \cdot \mathbf{u} = 0 \quad (5.65a)$$

$$\frac{\partial \mathbf{u}}{\partial t} + (\mathbf{u} \cdot \nabla) \mathbf{u} = -\nabla p + \text{Pr} \nabla^2 \mathbf{u} + Ra \text{Pr} T + Ha^2 \text{Pr} \mathbf{J} \times \mathbf{B} \quad (5.66a)$$

$$\frac{\partial T}{\partial t} + (\mathbf{u} \cdot \nabla) T = \nabla^2 T + 1 \quad (5.67a)$$

$$\nabla^2 \phi = \nabla \cdot (\mathbf{u} \times \mathbf{B}) = \mathbf{B} \cdot \boldsymbol{\omega} = 0 \quad (5.68a)$$

$$\nabla \mathbf{J} = 0 \quad (5.69a)$$

$$\mathbf{J} = -\nabla \phi + \mathbf{u} \times \mathbf{B} \quad (5.70a)$$

The nondimensional quantities were derived using the enclosure height ( $h$ ) as reference length. Thus, the nondimensional quantities are the following:

$$\begin{aligned} \tilde{\nabla} &= \nabla h & \tilde{\nabla}^2 &= \nabla^2 h^2 & \tilde{p} &= p h^2 / \rho a^2 & \tilde{\varphi} &= \varphi / B_0 \alpha \\ \tilde{\mathbf{B}} &= \mathbf{B} / B_0 & \tilde{\mathbf{J}} &= h \mathbf{J} / \sigma B_0 \alpha & \Theta &= (T - T_0) / \Delta T \\ \Delta T &= Q h^2 / k & \tilde{\mathbf{U}} &= \mathbf{U} h / a & \tilde{t} &= t a / h^2 \end{aligned} \quad (5.71)$$

The procedure in order to make the governing equations dimensionless was as follows:

Continuity equation

$$\nabla \cdot \mathbf{U} = 0 \Rightarrow \frac{1}{h} \frac{\partial}{\partial t} \tilde{\nabla} \cdot \tilde{\mathbf{U}} = 0 \Rightarrow \tilde{\nabla} \cdot \tilde{\mathbf{U}} = 0 \quad (5.65b)$$

Momentum equation

$$\begin{aligned} \frac{\partial \mathbf{U}}{\partial t} + (\mathbf{U} \cdot \nabla) \mathbf{U} &= -\frac{1}{\rho} \nabla p + \nu \nabla^2 \mathbf{U} + g \beta (T - T_0) + \frac{1}{\rho} \mathbf{J} \times \mathbf{B} \Rightarrow \\ \Rightarrow \frac{a}{h^2} \frac{a}{h} \frac{\partial \tilde{\mathbf{U}}}{\partial \tilde{t}} + \frac{a^2}{h^2} \frac{1}{h} (\tilde{\mathbf{U}} \cdot \tilde{\nabla}) \tilde{\mathbf{U}} &= \\ -\frac{1}{\rho} \frac{\rho a^2}{h^2} \frac{1}{h} \tilde{\nabla} \tilde{p} + \nu \frac{1}{h^2} \frac{a}{h} \tilde{\nabla}^2 \tilde{\mathbf{U}} + g \beta \Theta \Delta T + \frac{1}{\rho} \frac{\sigma \mathbf{B}_0^2 a}{h} \tilde{\mathbf{J}} \times \tilde{\mathbf{B}} &\Rightarrow \\ \Rightarrow \frac{\partial \tilde{\mathbf{U}}}{\partial \tilde{t}} + (\tilde{\mathbf{U}} \cdot \tilde{\nabla}) \tilde{\mathbf{U}} = -\tilde{\nabla} \tilde{p} + \frac{\nu}{a} \tilde{\nabla}^2 \tilde{\mathbf{U}} + \frac{g \beta Q h^5}{a^2 k} \frac{\nu}{v} \Theta + \frac{\sigma \mathbf{B}_0^2 h^2}{\rho a} \frac{\nu}{v} \tilde{\mathbf{J}} \times \tilde{\mathbf{B}} &\Rightarrow \\ \Rightarrow \frac{\partial \tilde{\mathbf{U}}}{\partial \tilde{t}} + (\tilde{\mathbf{U}} \cdot \tilde{\nabla}) \tilde{\mathbf{U}} = -\tilde{\nabla} \tilde{p} + \frac{\nu}{a} \tilde{\nabla}^2 \tilde{\mathbf{U}} + \frac{g \beta Q h^5}{a^2 \rho C_p v} \frac{\nu}{a} \Theta + \frac{\sigma \mathbf{B}_0^2 h^2}{\rho v} \frac{\nu}{a} \tilde{\mathbf{J}} \times \tilde{\mathbf{B}} &\Rightarrow \\ \Rightarrow \frac{\partial \tilde{\mathbf{U}}}{\partial \tilde{t}} + (\tilde{\mathbf{U}} \cdot \tilde{\nabla}) \tilde{\mathbf{U}} = -\tilde{\nabla} \tilde{p} + \text{Pr} \tilde{\nabla}^2 \tilde{\mathbf{U}} + \text{Ra} \text{Pr} \Theta + \text{Ha}^2 \text{Pr} \tilde{\mathbf{J}} \times \tilde{\mathbf{B}} & \end{aligned} \quad (5.66b)$$

Energy equation

$$\begin{aligned} \frac{\partial T}{\partial t} + (\mathbf{U} \cdot \nabla) T &= a \nabla^2 T + \frac{Q}{\rho C_p} \Rightarrow \\ \Rightarrow \frac{Q h^2}{k} \frac{a}{h^2} \frac{\partial \Theta}{\partial t} + \frac{a}{h} \frac{1}{h} \frac{Q h^2}{k} (\tilde{\mathbf{U}} \cdot \tilde{\nabla}) \Theta &= a \frac{1}{h^2} \frac{Q h^2}{k} \tilde{\nabla}^2 \Theta + \frac{Q}{\rho C_p} \Rightarrow \\ \Rightarrow \frac{Q h^2}{k} \frac{a}{h^2} \frac{\partial \Theta}{\partial t} + \frac{a}{h} \frac{1}{h} \frac{Q h^2}{k} (\tilde{\mathbf{U}} \cdot \tilde{\nabla}) \Theta &= a \frac{1}{h^2} \frac{Q h^2}{k} \tilde{\nabla}^2 \Theta + \frac{Q}{\rho C_p} \Rightarrow \\ \Rightarrow \frac{a}{k} \frac{\partial \Theta}{\partial t} + \frac{a}{k} (\tilde{\mathbf{U}} \cdot \tilde{\nabla}) \Theta = \frac{a}{k} \tilde{\nabla}^2 \Theta + \frac{a}{k} &\Rightarrow \frac{\partial \Theta}{\partial t} + (\tilde{\mathbf{U}} \cdot \tilde{\nabla}) \Theta = \tilde{\nabla}^2 \Theta + 1 \end{aligned} \quad (5.67b)$$

Potential equation

$$\begin{aligned} \nabla^2 \phi = \nabla \cdot (\mathbf{u} \times \mathbf{B}) &\Rightarrow \frac{1}{h^2} \mathbf{B}_0 a \tilde{\nabla}^2 \tilde{\phi} = \frac{1}{h} \mathbf{B}_0 \frac{a}{h} \tilde{\nabla} \cdot (\tilde{\mathbf{u}} \times \mathbf{B}) \Rightarrow \\ \Rightarrow \tilde{\nabla}^2 \tilde{\phi} = \tilde{\nabla} \cdot (\tilde{\mathbf{u}} \times \mathbf{B}) &= 0 \end{aligned} \quad (5.68b)$$

$$\nabla \mathbf{j} = 0 \Rightarrow \frac{1}{h} \frac{\sigma \mathbf{B}_0 a}{h} \tilde{\nabla} \tilde{\mathbf{j}} = 0 \Rightarrow \tilde{\nabla} \tilde{\mathbf{j}} = 0 \quad (5.69b)$$

Ohm`s law:

$$\begin{aligned}
 \mathbf{J} &= \sigma(-\nabla\phi + \mathbf{u} \times \mathbf{B}) \Rightarrow \\
 \Rightarrow \frac{\phi \mathbf{B}_0 \alpha}{h} \tilde{\mathbf{J}} &= \frac{\phi \mathbf{B}_0 \alpha}{h} (-\tilde{\nabla} \tilde{\phi} + \tilde{\mathbf{u}} \times \tilde{\mathbf{B}}) \Rightarrow \\
 \Rightarrow \tilde{\mathbf{J}} &= -\tilde{\nabla} \tilde{\phi} + \tilde{\mathbf{u}} \times \tilde{\mathbf{B}}
 \end{aligned} \tag{5.70b}$$

Then, the circumflex is neglected for simplicity. Hence, the equations 5.65b to 5.70b reduce to equations 5.65a to 5.70a which are presented above.

As far as the numerical process is concerned, Eqs. (5.65)-(5.67) together with the boundary conditions, which are illustrated in Fig. 5.1, are solved by using a finite volume technique based on the transient pressure-velocity coupling algorithm PISO, Issa (1986). PISO relies on the splitting of the solution process into a series of steps where operations on pressure are decoupled from those on velocity at each step. Moreover, Gaussian integration was used in order to sum the values on cell faces. Concerning the numerical schemes which were used in the simulations, the Crank-Nicolson scheme was used for the transient terms, central discretization for the laplacian and grad terms and gamma differencing for the convection terms (see Jasac (1996)). At each step, the solution is iterated until the residuals of the mass, momentum, electrostatic potential and temperatures equations become smaller than  $10^{-7}$ . Finally, the in-house MHD numerical model used the conjugate-gradient method, with incomplete Cholensky preconditioning (ICCG) (Jacobs (1980)), in order to solve the symmetric matrices and the Bi-CGSTAB method (Van der Vost (1992)) for the asymmetric matrices.

A nonuniform and second order finite volume staggered grid of 400x80 lines in the horizontal and vertical directions, respectively, with a finer distribution of nodes close to the walls was considered adequate for the present study. Special attention to the distribution of grid lines was given because the Hartmann boundary layers are narrow and must be adequately covered by the numerical grid. A fruitful discussion for the thickness of Hartmann layers in buoyancy-driven convection flows could be found in Alboussiere et al. (1993). The simulations were carried out in the CFD library OpenFOAM and the solutions were compared with the analytical ones.

### 5.5.4 Comparison of the analytical and numerical solutions

In this section the core solutions which were obtained by using the method of the matched asymptotic expansions (subchapter 5.3) are compared with the numerical ones

which cover also the regions in the vicinity of the vertical walls. The comparisons are limited only for low scaled Rayleigh numbers and for the indicative values  $R_s=200$ , 3000 and 5000 and for a range of Hartmann numbers from 0 to 50. Finally, the cavity aspect ratio was equal to 5 similar to Daniels and Jones (1998) analysis.

Concerning, the numerical analysis, the differences in the temperature fields for the same  $Ha$  and  $R_s$  numbers are proven to be almost independent of the Prandtl number used for large  $Ha$  or small  $R_s$ . The maximum differences between the temperatures profiles of different  $Pr$  arise for convective flows, i.e. for small  $Ha$  and large  $R_s$ . However, these differences seem to diminish by increasing  $Ha$  (or decreasing  $R_s$ ) as indicated by the results of Figs. 5.12a to 5.12c where, for brevity, only temperature profiles for  $R_s=3000$  and  $Ha=5, 15$  and  $50$  are presented.

Thereon, only numerical results for  $Pr=0.7$  were selected to be compared with the analytical ones. In Figs. 5.13 and 5.14 the analytical temperature profiles  $\theta_0$  are shown for a range of different values of  $Ha$  and  $R_s$ . The maximum fluid temperature is located, as expected, in the middle of the cavity while both  $Ha$  and  $R_s$  can influence notably the heat transfer mechanism. More specifically, as  $Ha$  decreases, convection dominates and the upward motion in the double cell becomes stronger in the core region. On the contrary, when  $Ha$  increases (or  $R_s$  decreases) the profiles coincide, indicating that the dominant mechanism of heat transfer is conduction. The comparison of the analytical temperature profiles with those of the low- $R_m$  numerical model demonstrates the initial hypothesis that the method of the matched asymptotic expansions is valid only for low  $R_s$ .

Furthermore, the numerical results show that the function  $C$  in Eq. (5.51) depends on  $L$ ,  $R_s$  and  $Ha$ , as follows:

$$C \approx \frac{1}{L} \left\{ -3 \cdot 10^{-8} R_s^2 + 25 \cdot 10^{-5} R_s + 6 \cdot 10^{-4} \right\} e^{-0.1Ha} \quad (5.71)$$

Considering this approximating value of  $C$  for the core region of the flow the errors between the numerical and the analytical results become very small. Table 5.4 indicates that the values of  $T$  at  $\xi=1/2$  and  $z=0$  for  $Pr=0.0321$ ,  $Pr=0.7$  and  $Pr=7$  are the same for low  $R_s$ , while the error is larger for higher values of  $R_s$ , especially for  $Pr=0.0321$ . Thus, the initial assumption, that the temperature profiles are independent of the Prandtl number, seems not to be valid for convective flows. The error between the analytical and numerical results diminishes as  $Ha$  increases regardless the value of  $R_s$ .



The relative error for each case is defined as  $100 \times (T_{\text{OpenFOAM}} - T_{\text{Analytical}}) / T_{\text{OpenFOAM}}$ . Table 5.4 demonstrates again that the analytical solution for temperature is more accurate for combinations of low  $R_s$  and large  $Ha$  values.

**Table 5.4** Values of both analytical and numerical temperatures at  $\zeta=1/2$  and  $z=0$ , for various combinations of  $Ha$  and  $R_s$  and  $Pr$ .

$R_s$	$T_{\text{Analytical}}$	$T_{\text{OpenFOAM}}$					
		$Pr=0.0321$	<b>Error (%)</b>	$Pr=0.7$	<b>Error (%)</b>	$Pr=7$	<b>Error (%)</b>
<b>Ha=0</b>							
200	3.134	3.110	-0.77	3.110	-0.77	3.110	-0.77
3000	2.263	2.491	9.15	2.253	-0.44	2.252	-0.49
5000	1.905	2.262	15.78	1.909	0.21	1.908	0.16
<b>Ha=5</b>							
200	3.138	3.118	-0.64	3.118	-0.64	3.118	-0.64
3000	2.437	2.590	5.91	2.510	2.91	2.508	2.83
5000	2.052	2.326	11.78	2.172	5.52	2.170	5.44
<b>Ha=15</b>							
200	3.135	3.123	-0.38	3.123	-0.38	3.122	-0.42
3000	3.023	3.011	-0.40	3.009	-0.47	3.010	-0.43
5000	2.805	2.865	2.09	2.862	1.99	2.863	2.03
<b>Ha=30</b>							
200	3.127	3.123	-0.13	3.123	-0.13	3.122	-0.16
3000	3.124	3.111	-0.42	3.111	-0.42	3.010	-0.45
5000	3.085	3.088	0.10	3.088	0.10	2.863	-7.75
<b>Ha=50</b>							
200	3.125	3.125	-0.00	3.123	-0.06	3.123	-0.06
3000	3.124	3.120	-0.13	3.120	-0.13	3.120	-0.13
5000	3.118	3.119	0.03	3.116	-0.06	3.116	-0.06

According to Daniels and Jones (1998), an average Nusselt number for the system based on the heat transfer through the end wall at  $x=0$  relative to the maximum difference in the cavity can be estimated from:

$$Nu_{av} = \frac{1}{T\left(\frac{1}{2}L, \frac{1}{2}\right)} \int_{-1/2}^{1/2} \frac{\partial T}{\partial \xi}(0, z) dz = \frac{1}{2T\left(\frac{1}{2}L, \frac{1}{2}\right)} = \frac{1}{2L\theta_0\left(\frac{1}{2}\right)}, L \rightarrow \infty \quad (5.72)$$

The appropriateness of Eq. (5.72) was assessed by the present results showing that the analytical average Nusselt numbers,  $Nu_{av}$ , were in good agreement with the numerical ones. This is confirmed in Figs. 5.15a and 5.15b where the analytical and the numerical values of the average Nusselt numbers are compared. The differences in the analytical and numerical solutions are small especially for the smaller  $R_s$  and larger  $Ha$  numbers, where the values of the average Nusselt number were the smallest indicating

the domination of conduction heat transfer. The errors increase for bigger  $R_s$  and lower  $Ha$  number but in any case the differences are limited and not significant.

Figure 5.15a shows also that as  $Ha$  increases the average Nusselt number decreases exponentially approaching the limiting value 0.8 of heat conduction. This indicates again that the increase of Hartmann number reduces the contribution of convection heat transfer while the variation of  $R_s$  can also influence significantly the fluid heat transfer. Fig. 5.15b shows that as  $R_s$  increases,  $Nu_{av}$  also increases because convection heat transfer starts dominating. Conversely, when  $R_s$  diminishes  $Nu_{av}$  decreases indicating that heat conduction dominates.

The above relation of  $R_s$  and  $Ha$  to the dominant heat transfer process is also demonstrated in Figs. 5.16 and 5.17, where the local Nusselt,  $Nu_l = \int_{-1/2}^{1/2} \frac{\partial T}{\partial \xi}(0, z) dz$ , is presented. It is observed that heat conduction is predominant near the horizontal walls, while within the cavity there is no pure heat transfer mechanism. It is shown again that for large values of  $Ha$  (or small values of  $R_s$ ) heat conduction is dominant. As a consequence in these cases, the profiles are almost perpendicular to the horizontal adiabatic walls and near the axis  $z=0$ .

While the analytical solution of the streamfunction cannot be applied near the walls, it is in good agreement in the core region of the cavity as shown in Figs. 5.18 and 5.19. The numerical results also show that the symmetry boundary condition of Eq. 5.22 is valid for both hydrodynamic and magnetohydrodynamic flows. Furthermore, Figs. 5.20a and 5.20b show that the maximum value of the analytical core stream function,  $\psi_{0,max}$  increases with increasing  $R_s$ , whereas  $\psi_{0,max}$  decreases for stronger external magnetic field. This remark, however, has no physical meaning since the true value of maximum stream function at  $\xi=0, L$  is always equal to zero as the numerical results confirmed.

The analytical solutions of the velocity profiles seem to be valid for low  $R_s$  and large  $Ha$  values as can be seen in Figs. 5.21 and 5.22. However, the analytical solutions for the core velocity cannot approach, as expected, the negative values of the vertical velocity near the vertical walls which indicate the downward fluid motion in this region. Figs. 5.21 and 5.22 indicate again that convection becomes stronger as  $R_s$  increases or  $Ha$  decreases.

The deceleration of the fluid flow and the heat transfer process is clearly illustrated in Figs. 5.23 and 5.24 where the temperature and streamlines contours are shown. Fig. 5.23 shows the aforementioned contours for  $Ha = 5$  and for scaled Rayleigh numbers equal to 200, 3000 and 5000 whereas Fig. 5.24 shows the contours for  $R_s = 3000$  and for Hartmann numbers equal to 5, 15 and 50. A physical explanation of Figs. 5.23 and 5.24 has as follows.

Heat production generates temperature gradients in the cavity, thus it further increases the effect of buoyancy in the flow arrangement. As a consequence, as  $R_s$  increases the temperature isolines became curved upwards indicating the tendency of the hot material to occupy the upper portion of the cavity which is demonstrated also by the temperature field distribution which acquires its maximum value at  $\xi = 1/2$ ,  $z = -1/2$ . As the effect of the buoyancy diminishes, by increasing the external magnetic field or by decreasing the heat production, the temperature isolines become nearly parallel to the magnetic field and the temperature field distribution seems to be horizontally stratified indicating that conduction is the predominant heat transfer mechanism. In addition, the streamlines indicate that as the buoyancy is intensified the upward motion in the double cell becomes significantly stronger at the middle of the horizontal cavity. Also the value of the streamfunction is increased as convection dominates as it has already been mentioned.

The symmetric fluid circulation becomes complicated at large Rayleigh numbers. Moreover, instabilities are expected to arise at sufficiently large Rayleigh numbers similar to the analysis of Hart (1972) who investigated the instabilities in laterally heated cavities.

In brief, all the analytical results were in good agreement with the numerical ones for the range of  $R_s$ ,  $Pr$  and  $Ha$  numbers studied. The maximum errors arise for the convection dominated flows whereas for small Rayleigh numbers and large values of external magnetic field the errors are minimized. From the numerical simulations, the value of the constant  $C$  for the temperature core solutions was estimated, thus, improving the accuracy of the analytical results.

An important finding of the numerical results is the circulating fluid motion near the end walls. For the analytical solutions, the fluid motion at the end walls must be considered separately, and serves in order to determine the value of  $C$ . In the hydrodynamic limit, Wang and Daniels (1994) developed a methodology to deal with the end region flow based on the work of Cormack et al. (1974) for  $R_s \rightarrow 0$  and the works

of Pohlhausen (1921) and Ostrach (1952). The global expansions must be replaced by local expansions in those regions that describe the turning motion. The solution of the end wall regions was discussed separately by Daniels and Jones (1998) and their analysis was based on matching the global with the local expansions at the interface. It should be noted that although the nonlinear buoyancy effects are important at the end walls, the heat source term is too small to contribute and, thus, the flow is driven by the thermal gradient and the recirculating flow of the core.

### **5.5.5 Conclusions**

The method of the matched asymptotic expansions was used in order to study laminar steady two-dimensional MHD natural convection of an electrically conductive fluid in a horizontal internally heated shallow cavity for a range of Prandtl, Rayleigh and Hartmann numbers. This analysis is valid for large cavity aspect ratios and low Rayleigh numbers. In addition, numerical simulations were carried out by using in-house numerical models in order to verify the analytical core solutions and to characterize the fluid motion near the vertical walls.

The resulting flow consists of a symmetric double-cell Hadley circulation with the fluid ascending in the center of the cavity and descending in the regions near the vertical walls. For low Rayleigh numbers (i.e. low internal heating) or high Hartmann numbers (i.e. strong external magnetic fields), conduction heat transfer dominates resulting in a horizontally stratified flow. As the Rayleigh number increases and the Hartmann number decreases, non-linear convective effects become important and modify the stratification.

Both the analytical and numerical results demonstrate that the fluid is decelerated by the external magnetic field leading to the dominance of conduction over convection and, therefore, reducing the heat transfer. As a consequence, the fluid temperature is kept high and, thus, the vertical walls lose their ability to cool the enclosed fluid. While the core flow features remain the same, low magnetic fields lead to non-linear effects at higher Rayleigh numbers. The present study, however, is limited to laminar flows before any unstable convection or multicellular flow structures develop.

The comparison between the numerical and analytical results showed, as expected, that the latter are not accurate for convective flows. Nevertheless, they are in good agreement for combinations of low Rayleigh and large Hartmann numbers.

Finally, instabilities are expected to arise at sufficiently large Rayleigh numbers but it is not clear to what extent any instability will exist, since the present work deals only with low Rayleigh numbers ensuring laminar flow.

Although the present analysis is limited to two-dimensional flows and cannot also handle the downward fluid motion near the vertical walls, it permits a detailed assessment of the effect of Prandtl, Rayleigh and Hartmann numbers on the flow field.

## CLOSURE AND FUTURE WORK

The main objective of the present thesis, which was to study MHD natural convection flow in shallow cavities due to internal heat analytically by means of matched asymptotic expansions, was successfully fulfilled. Moreover, in the limits where the magnetic field vanishes, the results were the same as those of Daniels and Jones (1998). The present study was limited to laminar flows before any unstable convection or multicellular flow structures develop. It is hoped to investigate the stability properties of the internally heated system in future work.

The numerical simulations for the purpose of this thesis were carried out by using in-house numerical models within the OpenFOAM CFD library. The governing equations together with the boundary conditions were solved using the control volume method. Furthermore, a finer distribution of the grid nodes close to the walls was implemented in order to better resolve the flow inside the boundary layers.

Concerning the validation of the numerical models, the low- $R_m$  model, which ignores the induced magnetic field produced by the motion of the electrically conducting fluid, was successfully compared with the work of Al-Najem et al. (1998). Then, the full MHD model was at first validated using the work of Orszag and Tang (1989), and after adding the energy equation and the Boussinesq approximation, with Sarris et al. (2006).

The development of this validated full MHD numerical model, which is capable to deal with MHD natural convection flows, could be useful in order to compare a number of numerical simulations, which have been carried out in the past using the low- $R_m$  approximation, pointing out the errors and revealing some interesting physics.

Finally, the transition from laminar to turbulent flows of electrically conducting fluids in cylinder and toroidal geometries, for the purpose of simulating the transport phenomena within blankets, which are used in TOKAMAK fusion devices, is going to be the subject for the author's doctoral research. Except from the finite volumes method, which was analyzed in detail, other approaches will be used such as spectral methods for better accuracy of the numerical simulations.

Furthermore, cooling process of low-Pr fluids and how they are affected by a uniform magnetic field will be investigated. The above processes are of great interest, for example in the case of an accident in nuclear plants.

## References

- Al-Najem N., Khanafer K., and El-Rafae M., *Numerical Study of laminar Natural Convection in Tilted Enclosure with Transverse Magnetic Field*, Int. J. Numer. Meth. Heat Fluid Flow, Vol. 8, pp. 651–672, 1998.
- Blanket Technology, [http://www.naka.jaea.go.jp/english/kougaku-e/pfc&blk/BLK/BLK\\_P1.html](http://www.naka.jaea.go.jp/english/kougaku-e/pfc&blk/BLK/BLK_P1.html), 2010.
- Bird R., Stewart W., and Lightfoot E., *Transport Phenomena*, 2nd ed., J. Wiley, 2002.
- Biskamp D. and Welter H., *Dynamics of decaying two-dimensional magnetohydrodynamic turbulence*, Phys. Fluids B, Vol. 1, 1964 (1989).
- Boyd T. and Danderson J., *The Physics of Plasma*, Cambridge University Press, Cambridge, UK, 2003.
- Cormack D., Leal L. and Imberger J., *Natural convection in a shallow cavity with differentially heated end walls. Part 1. Asymptotic theory*. J. Fluid Mech., Vol. 65, pp. 209-229, 1974.
- Daniels P. and Jones O., *Convection in a shallow cavity due to internal heat generation*. Int. J. Heat Mass Transfer, Vol. 41, pp. 3979-3987, 1998.
- Davidson P., *An introduction to Magnetohydrodynamics*, Cambridge Univ. Press, Cambridge, UK, 2001.
- De Bock M., *Understanding and Controlling Plasma Rotation in Tokamaks*. PhD Thesis, Univ. of Eindhoven, the Netherlands, 2007.
- Diagnostics, ITER: The way to new energy, <http://www.iter.org/mach/diagnostics>, 2010.
- EFDA (European Fusion Development Agreement), <http://www.efda.org/>, 2010.
- Friedel H., Grauer R. and Marliani C., *Adaptive mesh refinement for singular current sheets in incompressible magnetohydrodynamic turbulence*. J. Comp. Phys., Vol. 134, pp. 190–198, 1997.
- Garandet J., Alboussiere T. and Moreau R., *Buoyancy driven convection in a rectangular enclosure with a transverse magnetic field*, Int. J. Heat Mass Transfer, Vol. 35, pp. 741-748, 1992.
- Grauer R., & Marliani, *Current-Sheet Formation in 3D Ideal Incompressible Magnetohydrodynamics*, Phys. Rev. Lett., Vol. 84, pp. 4850-4853, 2000.
- Greene J., *Journal of Geophysical Research (Space Physics)*, Vol. 93(A8), pp. 8583 - 8590, 1988.
- Hart J., *Stability of thin non-rotating Hadley circulation*. J. Atmos. Sci., Vol. 29, pp. 687-697, 1972.
- Hart J., *Low Prandtl number convection between differentially heated end walls*, Int. J. Heat Mass Transfer, Vol. 26, pp. 1069-1074, 1983.
- Hjellming L., *A thermal model for Czochralski silicon crystal growth with an axial magnetic field*. J. Crystal Growth, Vol. 104, pp. 327-344, 1990.

[http://openfoamwiki.net/index.php/How to add temperature to icoFoam](http://openfoamwiki.net/index.php/How_to_add_temperature_to_icoFoam), 2010

Ihli T., Basu T., Giancarli L., Konishi S., Malang S., Najmabad F., Nishio S., Raffray A., Rao C., Sagara A., Wu Y., *Review of blanket designs for advanced fusion reactors*, Fusion Engineering and Design, Vol. 83, pp.912–919, 2008.

Iatridis A., *Magnetohydrodynamic flow in fusion machine ducts: Transition from laminar to turbulent flow*, PhD Thesis, Univ. Thessaly, to be defended, July 2012.

Issa R., Solution of the implicitly discretised fluid flow equations by operator-splitting, *Comput. Phys.*, Vol. 62, pp. 40-65, 1986.

Jasak H., “*Error analysis and estimation for the finite volume method with applications to fluid flows*”. PhD thesis, Imperial College, London, 1996.

Miller D. and Pernell T., *Fluid flow patterns in a simulated garnet melt*. *J. Crystal Growth*, Vol. 57, pp. 253-260, 1982.

Mininni P., Pouquet A. and Montgomery D., *Small-scale structures in three-dimensional magnetohydrodynamic turbulence*, *Phys. Rev. Lett.* Vol. 97, pp. 244503, 2006.

Miyamoto K., *Plasma physics and Controlled Nuclear Fusion*, Springer, Tokyo, 2004.

Moreau R., *Magnetohydrodynamics*, Kluwer, London, 1990.

Oreper G. and Szekely J., *The effect of an external imposed magnetic field on buoyancy driven flow in a rectangular cavity*. *J. Crystal Growth*, Vol. 64, pp. 505-515, 1983.

Orszag S., *Design of large hydrodynamic codes*. In *Computer Science and Scientific Computing*, Academic Press, p. 191, 1976.

Orszag S. and Tang C., *Small-scale structure of two-dimensional magnetohydrodynamic turbulence*. *J. Fluid Mech.*, Vol. 90, pp. 129–143, 1979.

Ostrach S., *An analysis of laminar free convection flow and heat transfer about a flat plate parallel to the direction of the generating body force*, In NACA TN2635, Washington D.C., 1952.

Ozoe H. and Okada K., *The Effect of the Direction of the External Magnetic Field on the Three-Dimensional Natural Convection in a Cubical Enclosure*, *Int. J. Heat Mass Transfer*, Vol. 32, pp. 1939–1954, 1989.

Parashar T., Shay M., Cassak P. and Matthaeus W., *Kinetic dissipation and anisotropic heating in a turbulent collisionless plasma*, *Physics of Plasmas*, Vol. 16, 032310, 2009.

Pasko J., *Magnetic Confinement of Plasmas for Fusion*, 2009.

Peeters A., *The Physics of Fusion Power- Lecture notes*, Warwick Univ., 2008.



- Picone J., and Dahlburg R., *Evolution of the Orszag–Tang vortex system in a compressible medium I. Initial averages subsonic flow*. Phys. Fluids B, Vol. 1, pp. 2153-2171, 1989.
- Picone J., and Dahlburg R., *Evolution of the Orszag–Tang vortex system in a compressible medium II. Supersonic flow*. Phys. Fluids B, Vol. 3, pp. 29–44, 1991.
- Pohlhausen E., *Der Wärmeaustausch zwischen festen Körpern und flüssigkeiten mit kleiner Reibung und Wärmeleitung*. Z Angew. Math Mech., Vol. 1, pp. 115-121, 1921.
- Politano H. and Pouquet A., *Current and vorticity dynamics in three dimensional magnetohydrodynamic turbulence*, Phys. Plasmas, Vol. 2, pp. 2931-2939, 1995.
- Pouquet A., *On two–dimensional magnetohydrodynamic turbulence*, J. Fluid Mech., Vol. 88, p. 1, 1978.
- Proust E., Anzidei L., Casini G., Donne M., Giancarli L. and Malang S., *Breeding blancet for DEMO*. Fusion Engng and Design, Vol. 22, pp. 19-33, 1993.
- Sarris I., Zikos G., Grecos A. and Vlachos N., *on the limits of validity of the low magnetic Reynolds number approximation in MHD natural convection heat transfer*, Num. Heat Transfer, Part B, Vol. 35, pp. 741-748, 2006.
- Schnack D., *Lectures in Magnetohydrodynamics*, Springer, Berlin-Heidelberg, 2009.
- Shigemitsu R., Tagawa T., and Ozoe H., *Numerical Computation for Natural Convection of Air in a Cubic Enclosure under Combination of Magnetizing and Gravitational Forces*, Numer. Heat Transfer A, Vol. 43, pp. 449–463, 2003.
- Tagawa T. and Ozoe H., *Enhancement of Heat Transfer Rate by Application of a Static Magnetic Field during Natural Convection of Liquid Metal in a Cube*, ASME J. Heat Transfer, Vol. 119, pp. 265–271, 1997.
- The Tokamak*, CCFE, Fusion Energy, <http://www.ccf.ac.uk/Tokamak.aspx>, 2010.
- Van der Vorst H., *Bi-CGSTAB: A Fast and Smoothly Converging Variant of Bi-CG for the solution of Nonsymmetric Linear systems*, SIAM J. Sci. and Stat. Comput., Vol. 13, pp. 631-644, 1992.
- Versteeg H., Malalasekera W., *An introduction to Computational Fluid Dynamics: The Finite Fluid Method. 2nd ed.*, Longman, England, 1995.
- Wang P. and Daniels P., *Numerical solutions for the flow near the end of a shallow laterally heated cavity*. J. Engng Mathematics, vol. 28, pp. 211-226, 1994.
- Weller H., Jasak H. and Fureby C., *A tensorial approach to computational continuum mechanics using object-oriented techniques*, Computers in Physics, Vol. 12, pp. 620-631, 1998.
- Weller H., User Guide. OpenCFD Ltd., [www.opencfd.co.uk](http://www.opencfd.co.uk), 2004a.
- Weller H., OpenFOAM Programmer’s Guide, First edition, OpenCFD Ltd., [www.opencfd.co.uk](http://www.opencfd.co.uk), 2004b.

Wu C., *A high order WENO finite difference scheme for incompressible fluids and magnetohydrodynamics. I.* Geophys. Res., Vol. 101, pp. 37-61, 2007.

## Appendix

### A. Orszag-Tang vortex

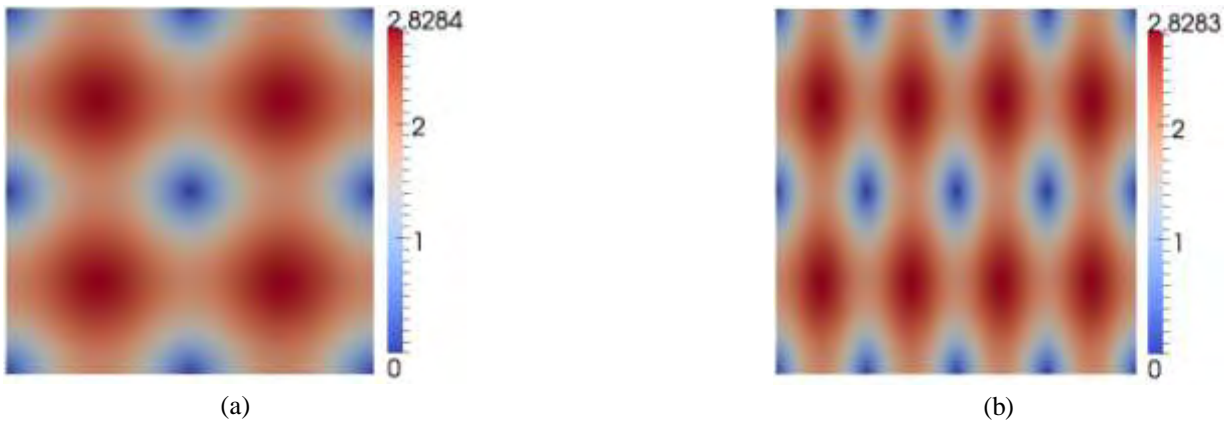


**Fig. 4.3** Initial distribution of the Orszag-Tang problem using a 512x512 grid: (a) Velocity and (b) Magnetic field

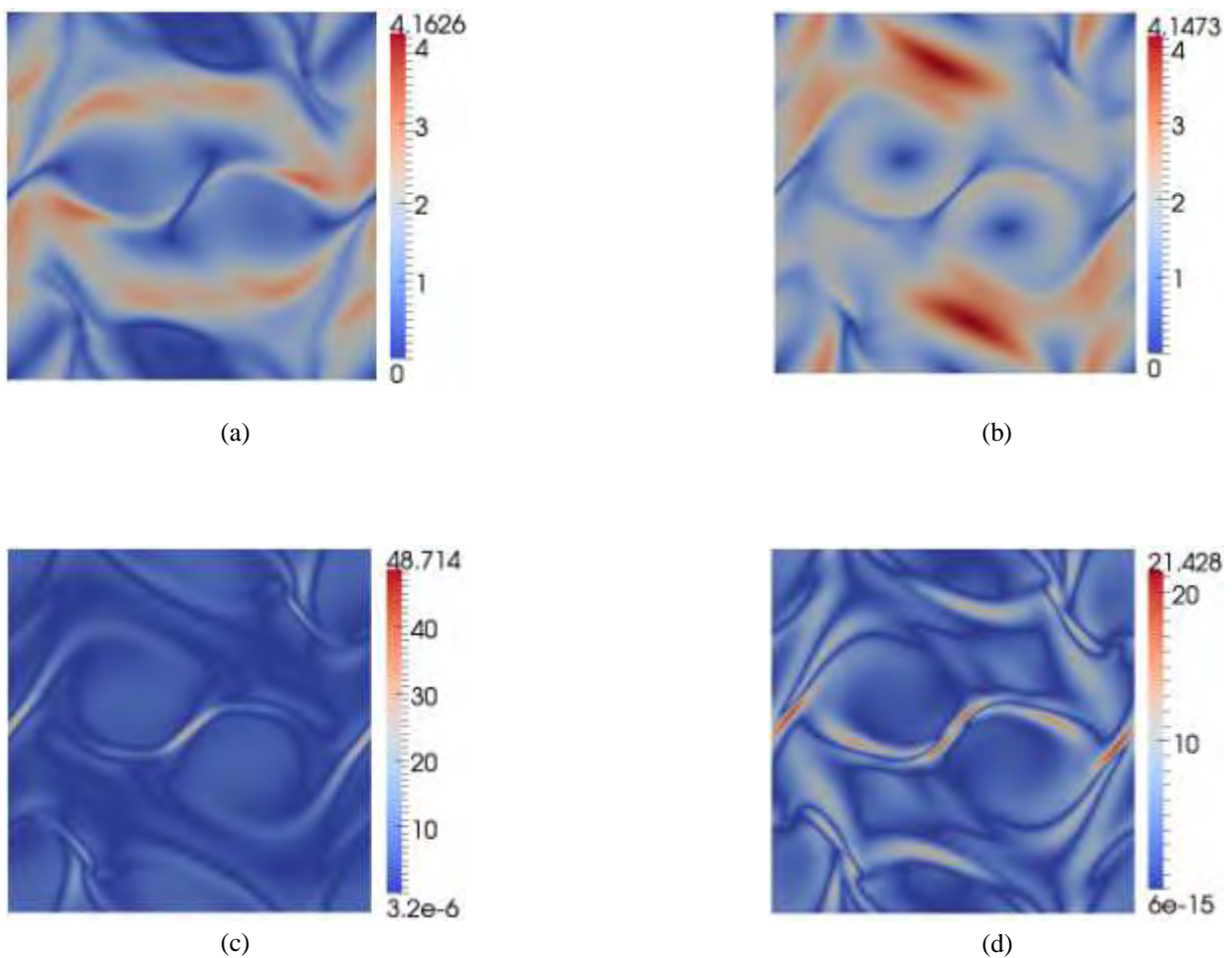


**Fig. 4.4** Distributions of the Orszag-Tang problem at  $t=1$  using a 512x512 grid: (a) Velocity field, (b) Magnetic field, (c) Current density and (d) Vorticity

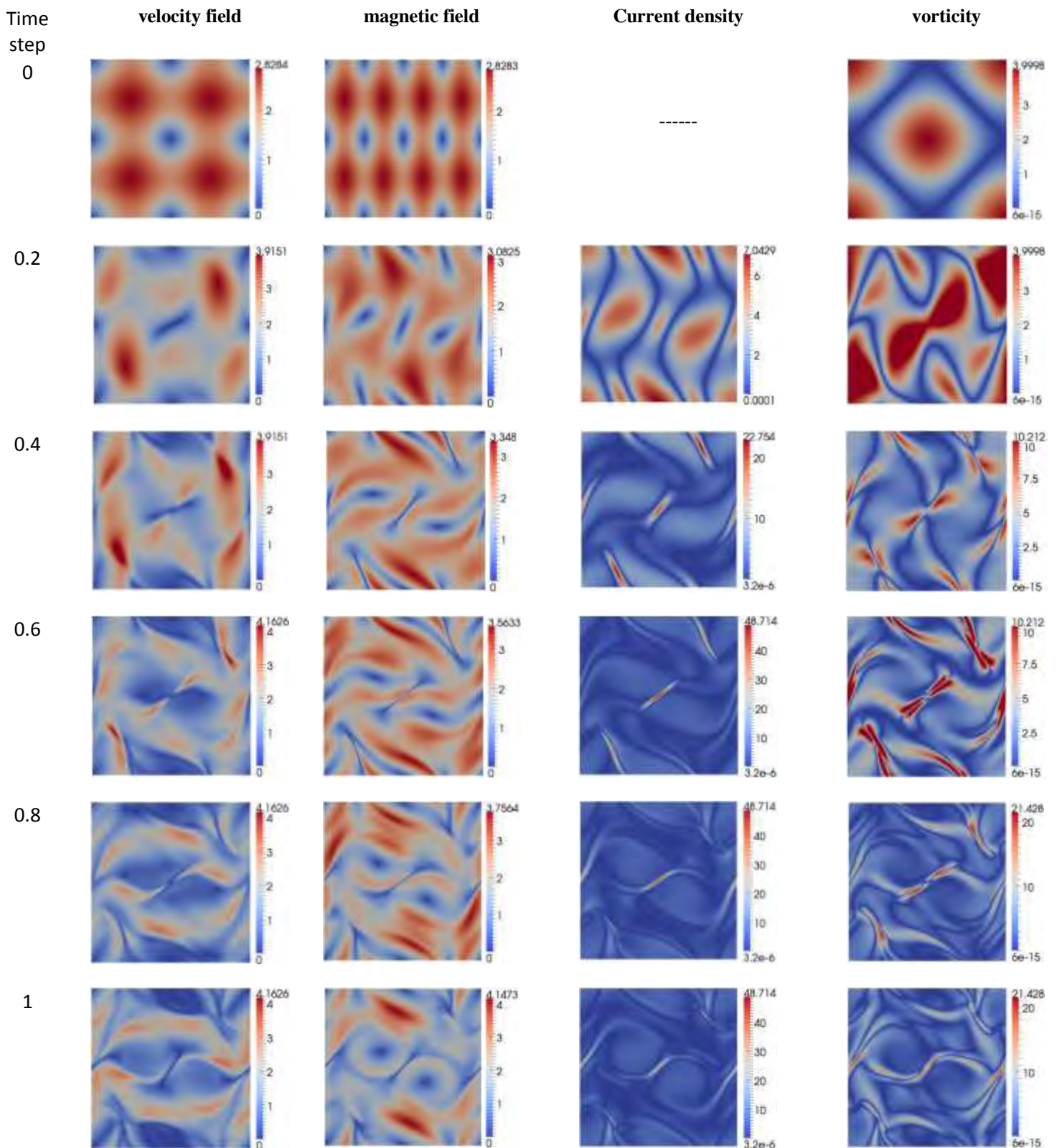


**Fig. 4.5a** Distributions of the Orszag-Tang problem at  $t=1$  using a  $512 \times 512$  grid: (a) Velocity field, (b) Magnetic field, (c) Current density and (d) Vorticity from 0 to 1 with a 0.2 time step

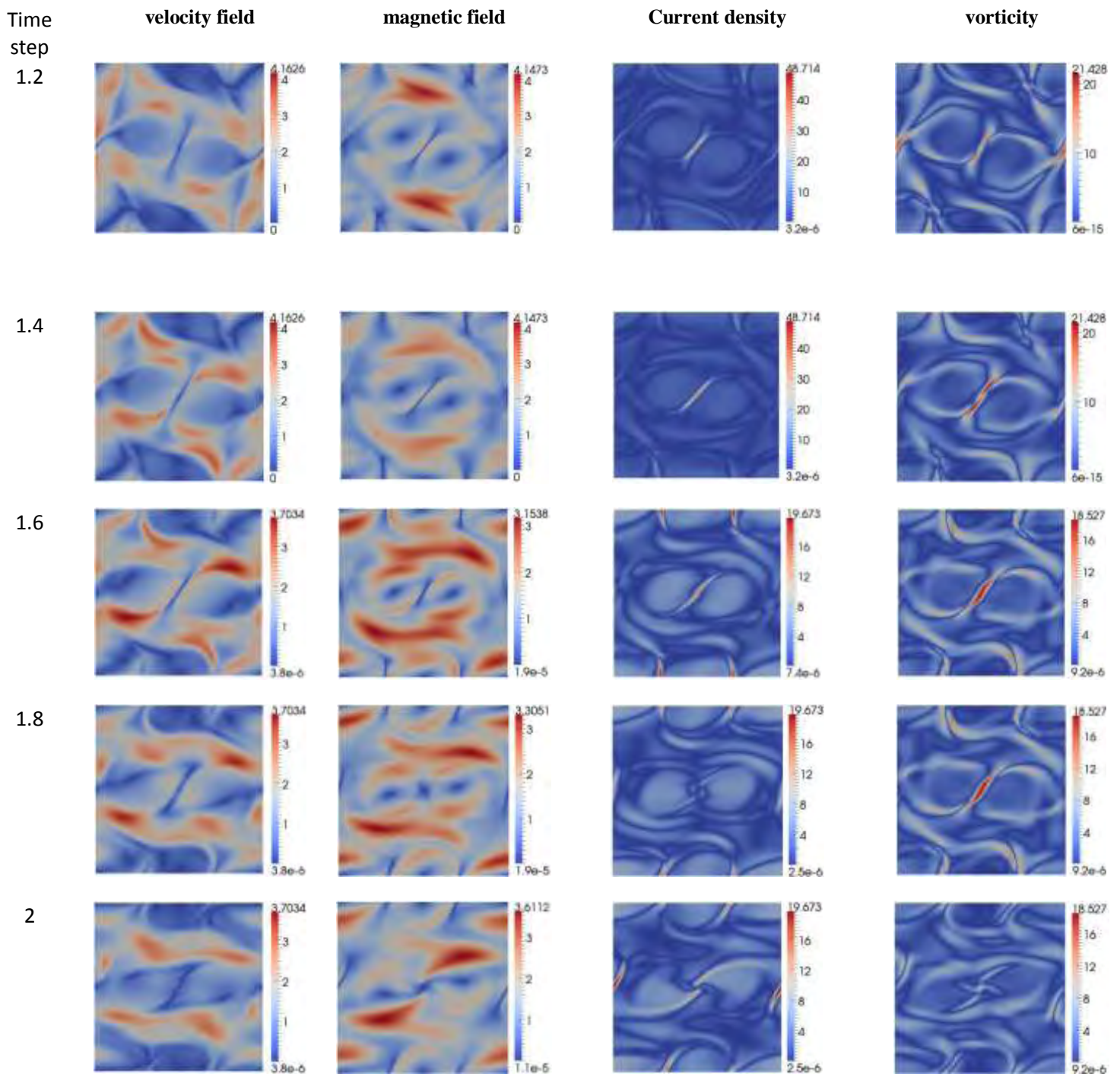


**Fig. 4.5b** Distributions of the Orszag-Tang problem at  $t=1$  using a  $512 \times 512$  grid: (a) Velocity field, (b) Magnetic field, (c) Current density and (d) Vorticity from 1.2 to 2 with a 0.2 time step

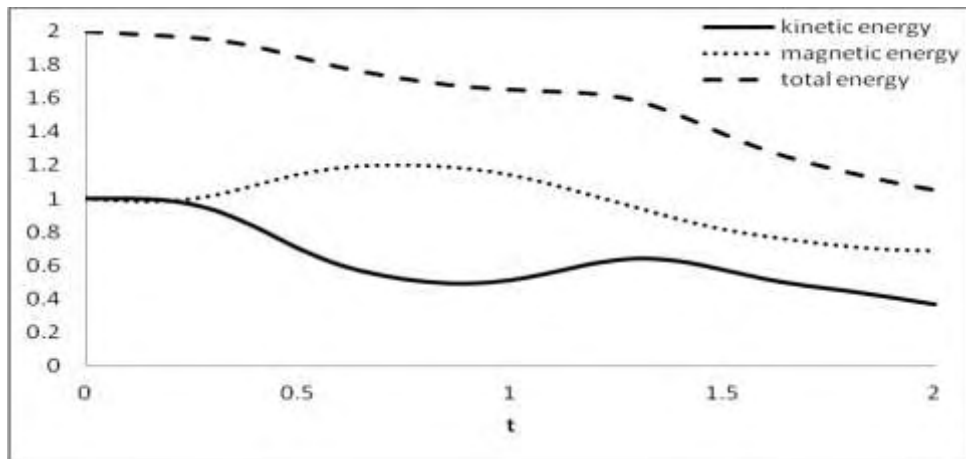


**Fig. 4.6** Evolution of kinetic, magnetic and total energy for  $\eta=v=0.02$  using a  $512 \times 512$  grid

**B. Magnetohydrodynamic natural convection in a differentially heated shallow cavity with transverse magnetic field (numerical results)**

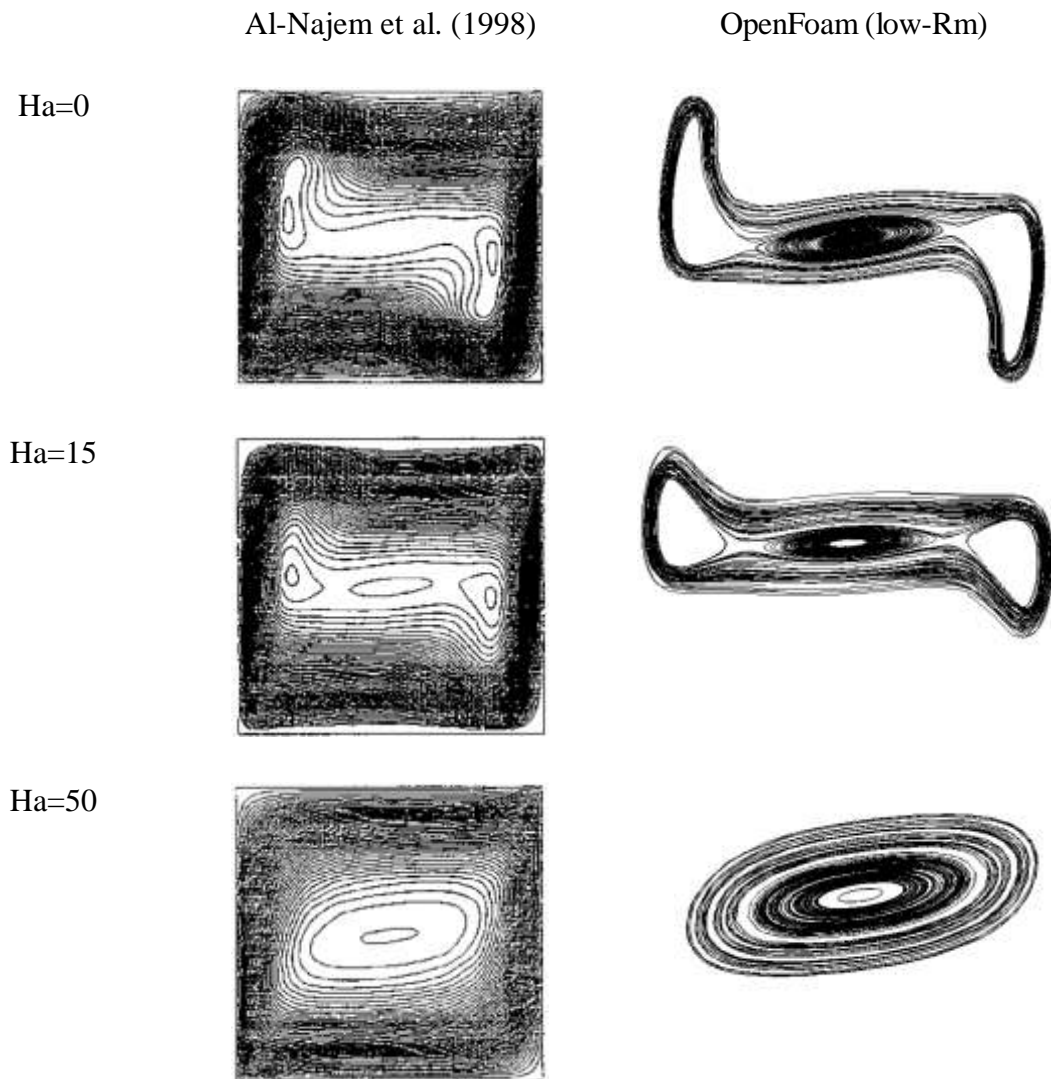


*Fig. 5.4 Profiles of the streamfunction field for various values of  $Ha$  and  $Gr=10^6$ . OpenFOAM's profiles represent the streamfunction in the middle area of the cavity*

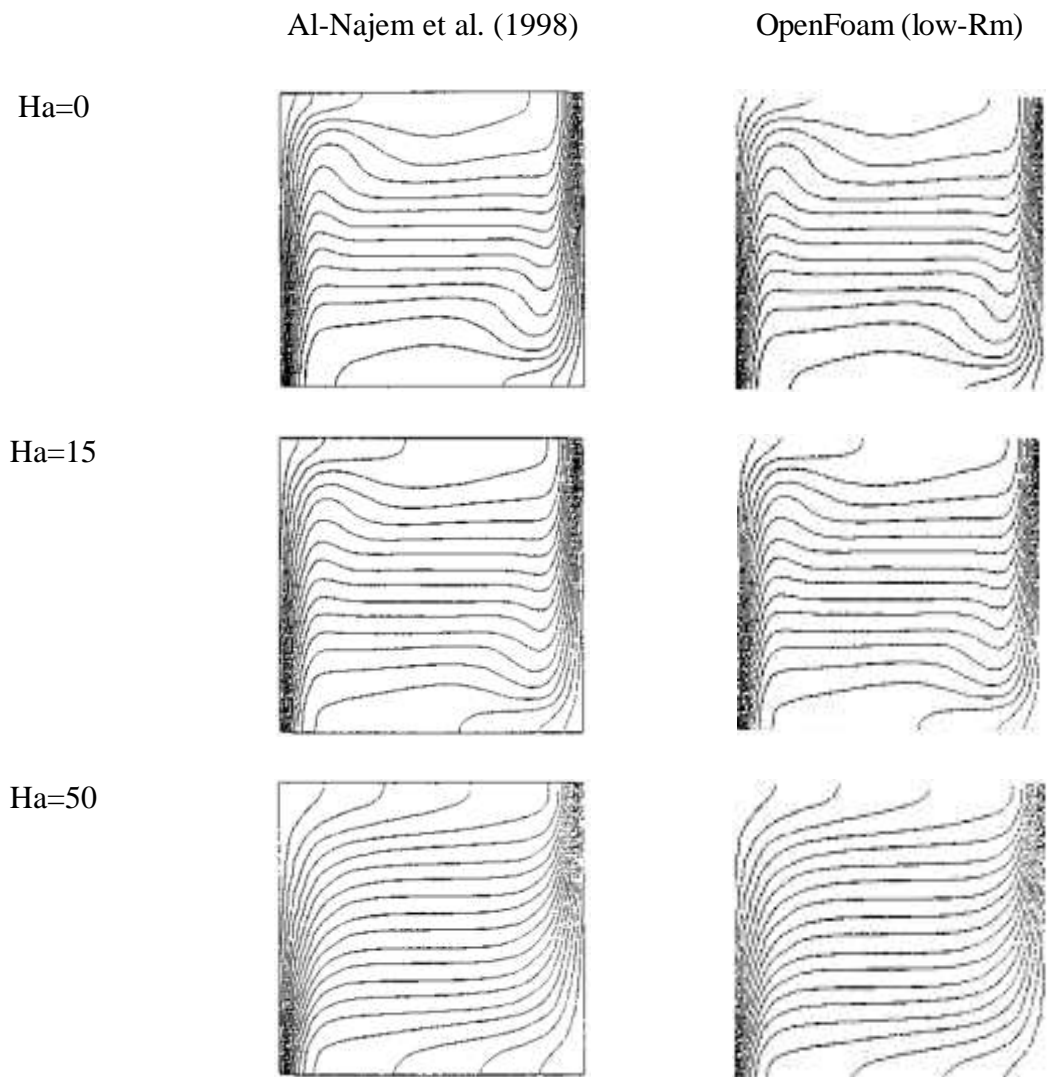


**Fig. 5.5** Comparison between the isotherms conducted by Al-Najem et al (1998) and OpenFOAM for various values of Ha at  $Gr=10^6$



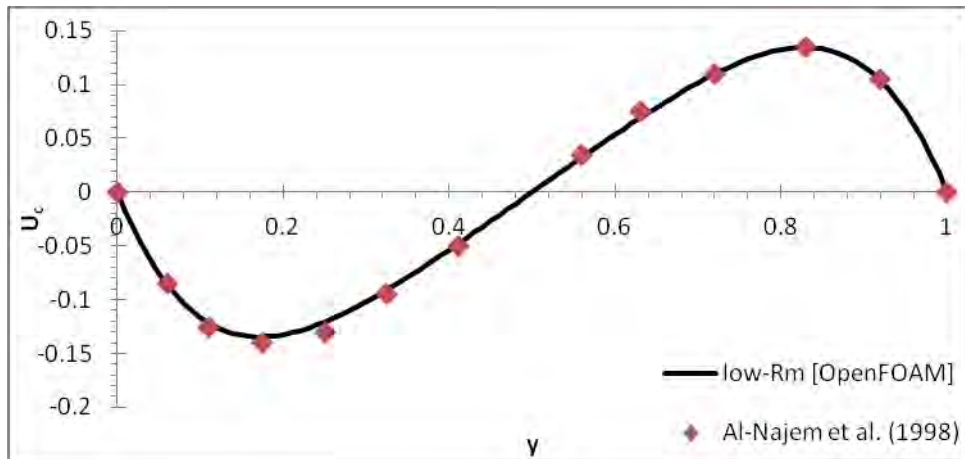


**Fig. 5.6** Comparison of the midsection velocity between the present low-Rm model and Al-Najem et. Al (1998) at  $Ha=10$  and  $Gr=10^4$

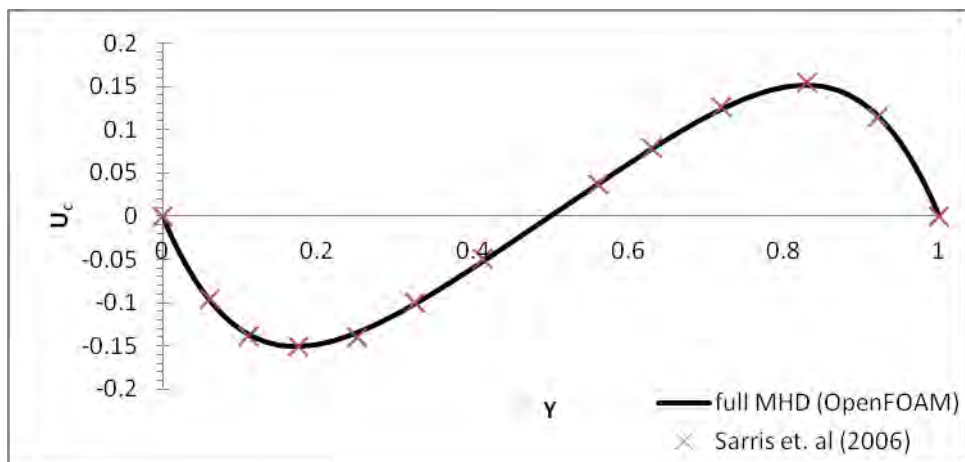


**Fig. 5.7** Comparison of the midsection velocity between the present full MHD model and Sarris et. al at  $Ha=10$  and  $Gr=10^4$

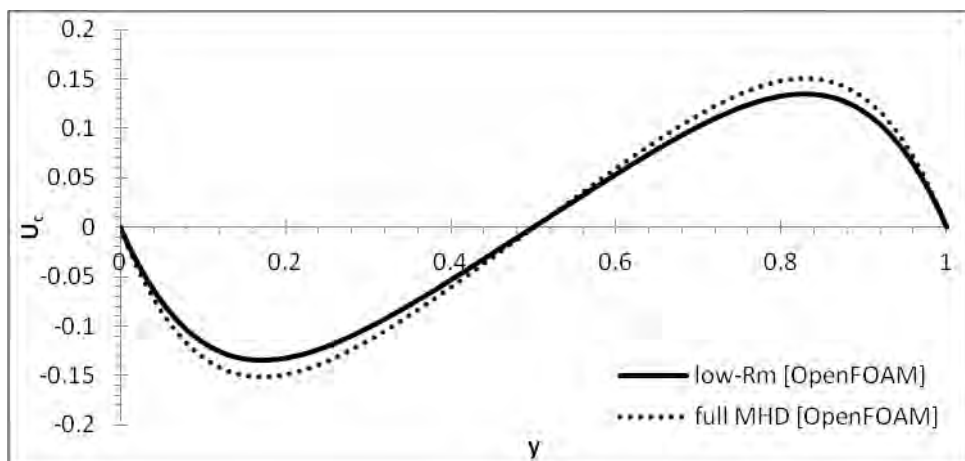


**Fig. 5.8** Comparison of the midsection velocity between the low-R<sub>m</sub> and full MHD models applied in OpenFOAM at  $Ha=10$  and  $Gr=10^4$

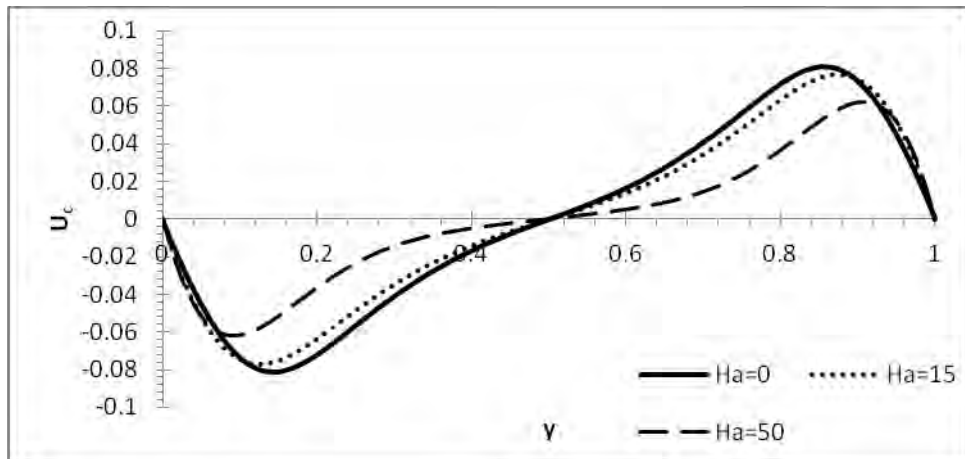


**Fig. 5.9** Velocity profiles at the midsection of the cavity for different values of  $Ha$  at  $Gr=10^6$  with the low- $R_m$  model applied in OpenFOAM

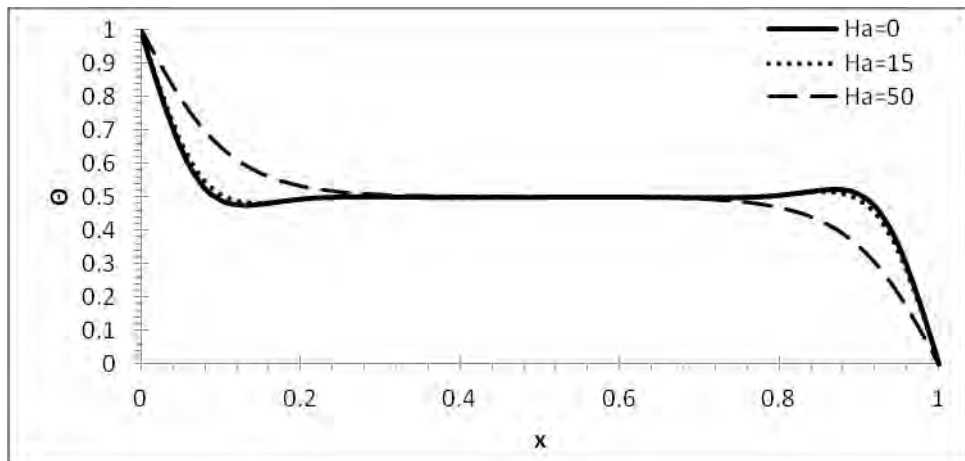


**Fig. 5.10** Temperature profiles at the midsection of the cavity for different values of  $Ha$  at  $Gr=10^6$  with the low- $R_m$  model applied in OpenFOAM

**C. Two dimensional magnetohydrodynamic natural convection flow in an internally heated shallow cavity (comparison of the analytical and numerical results)**

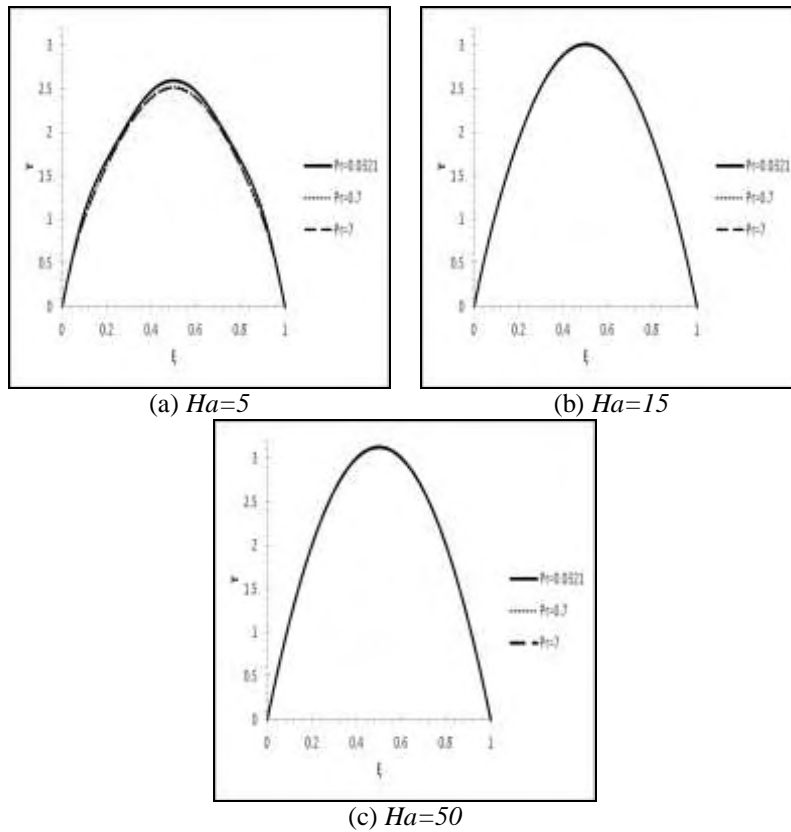


**Fig. 5.12** Temperature profiles obtained by the low- $R_m$  numerical model for  $Pr=0.0321, 0.7$  and  $7$ , and  $R_s=3000$ : (a)  $Ha=5$ , (b)  $Ha=15$ , (c)  $Ha=50$

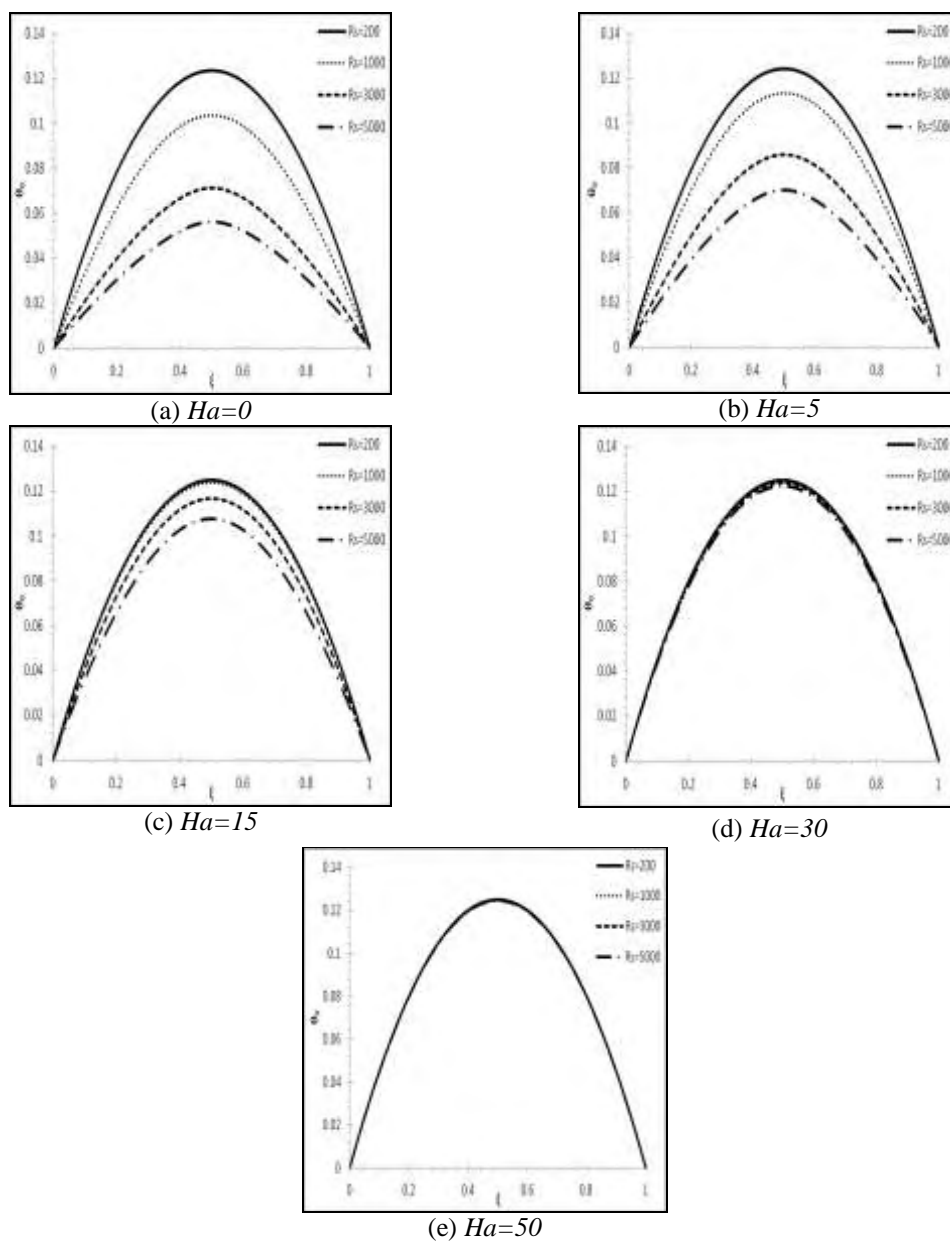
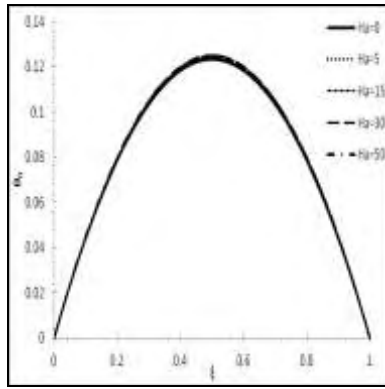
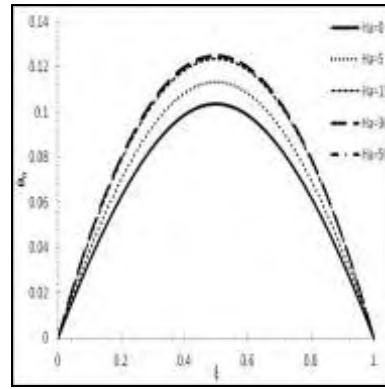


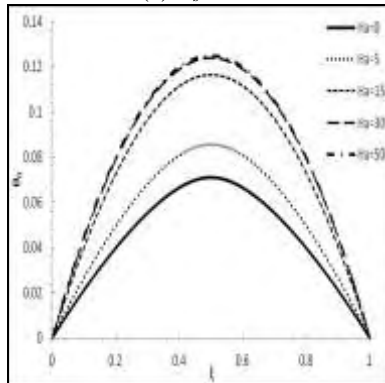
**Fig. 5.13** Core temperature profiles for various values of  $R_s$ : (a)  $Ha=0$ , (b)  $Ha=5$ , (c)  $Ha=15$ , (d)  $Ha=30$ , (e)  $Ha=50$



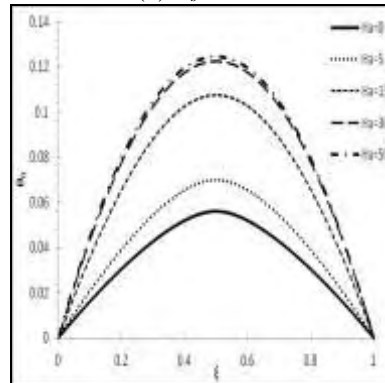
(a)  $R_s=200$



(b)  $R_s=1000$

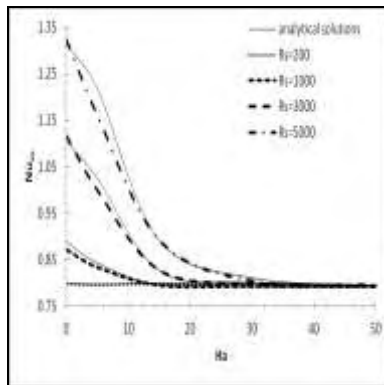


(c)  $R_s=3000$

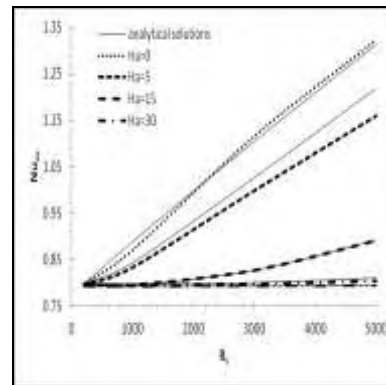


(d)  $R_s=5000$

**Fig. 5.14** Core temperature profiles for various values of  $Ha$ : (a)  $R_s=200$ , (b)  $R_s=1000$ , (c)  $R_s=3000$ , (d)  $R_s=5000$

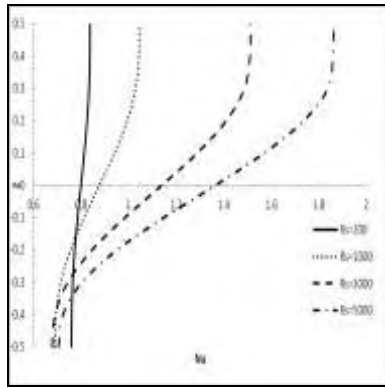


(a)

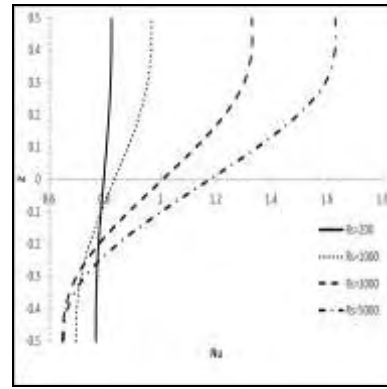


(b)

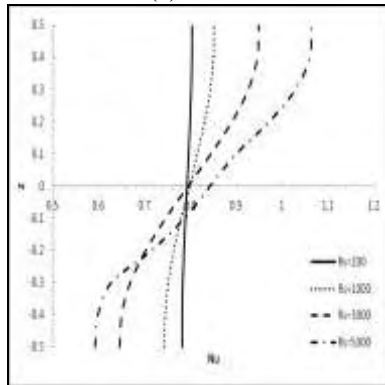
**Fig. 5.15** Variation of the average Nusselt number with (a)  $R_s$  and (b)  $Ha$



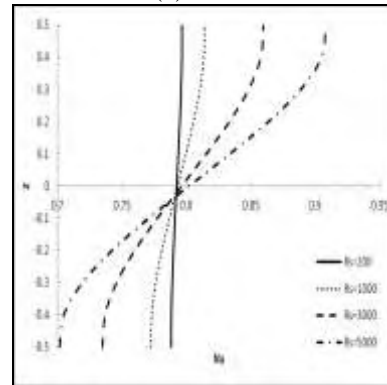
(a)  $Ha=0$



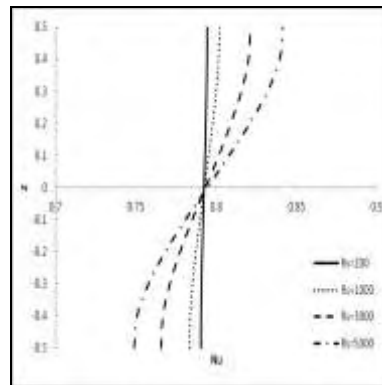
(b)  $Ha=5$



(c)  $Ha=15$

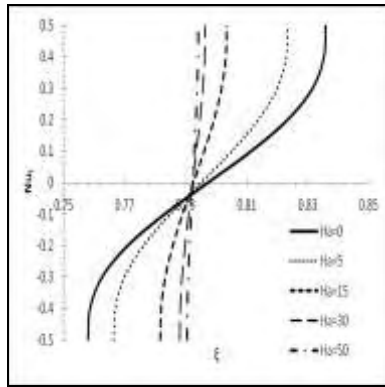


(d)  $Ha=30$

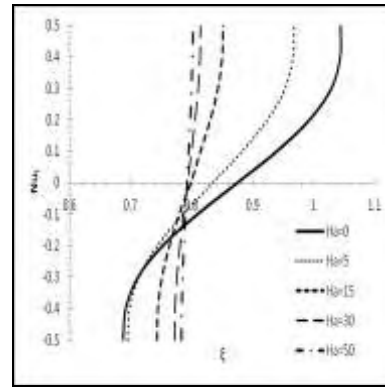


(e)  $Ha=50$

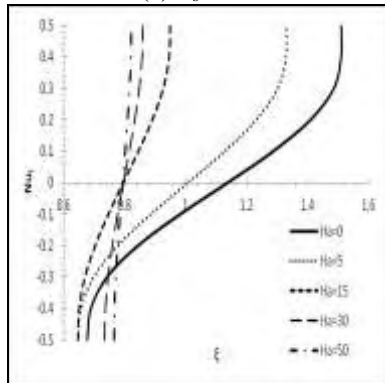
**Fig. 5.16** Distribution of the local Nusselt number for various values  $Re$ ; (a)  $Ha=0$ , (b)  $Ha=5$ , (c)  $Ha=15$ , (d)  $Ha=30$ , (e)  $Ha=50$



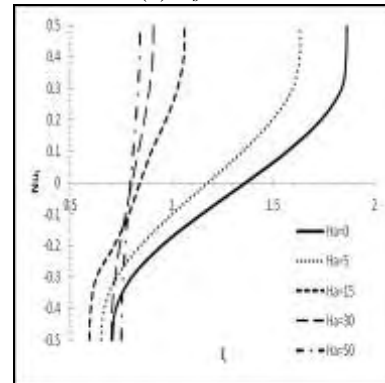
(a)  $R_s=200$



(b)  $R_s=1000$



(c)  $R_s=3000$



(d)  $R_s=5000$

**Fig. 5.17** Distribution of the local Nusselt number for various values of  $Ha$ : (a)  $R_s=200$ , (b)  $R_s=1000$ , (c)  $R_s=3000$ , (d)  $R_s=5000$

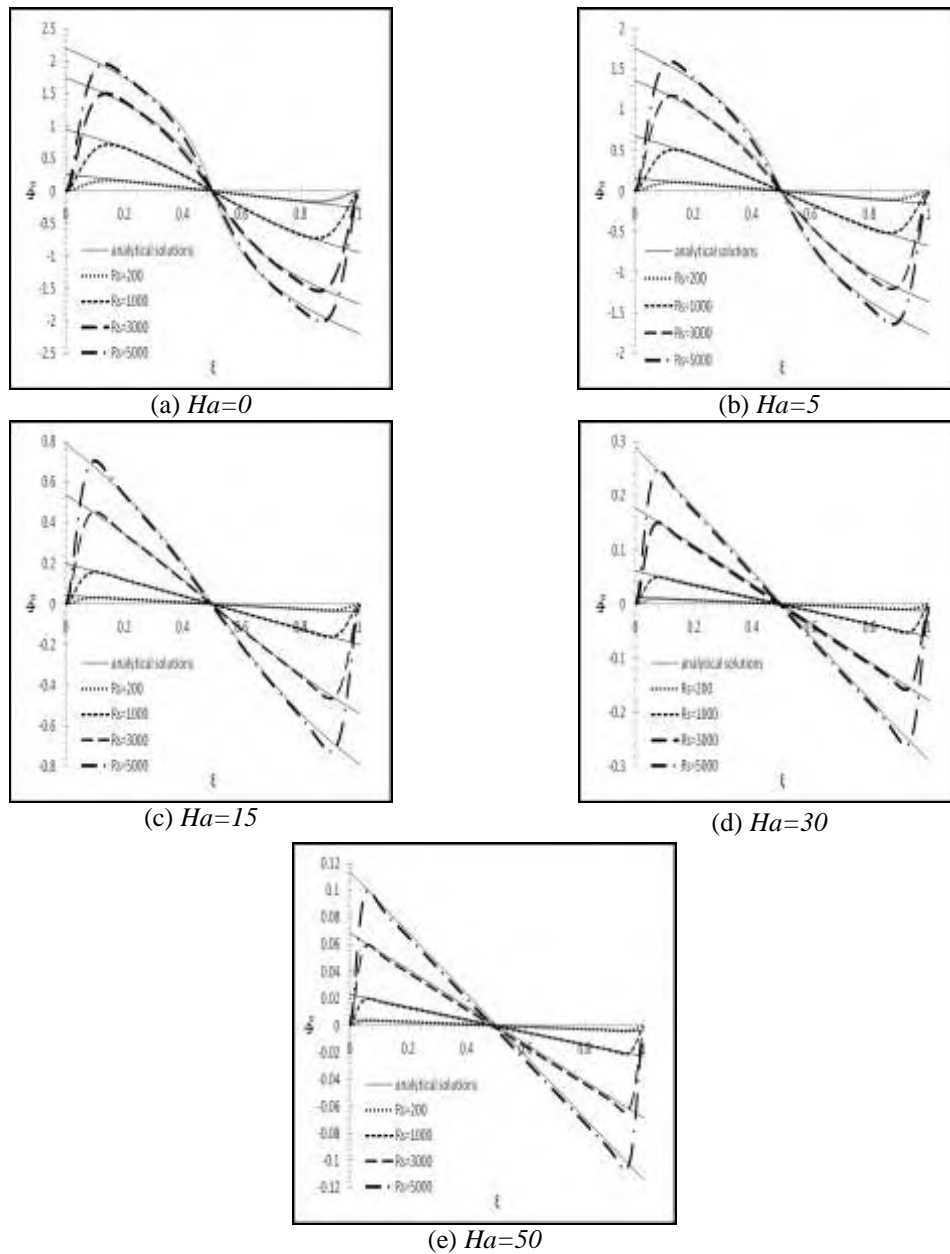
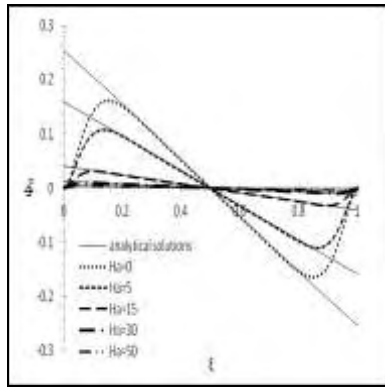
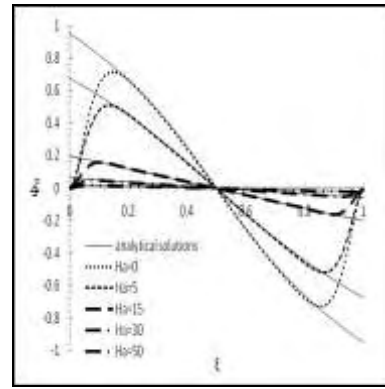


**Fig. 5.18** Distribution of the core streamfunction  $\psi_0$  at mid-cavity height ( $z=0$ ) for various values of  $R_s$ :  
 (a)  $Ha=0$ , (b)  $Ha=5$ , (c)  $Ha=15$ , (d)  $Ha=30$ , (e)  $Ha=50$

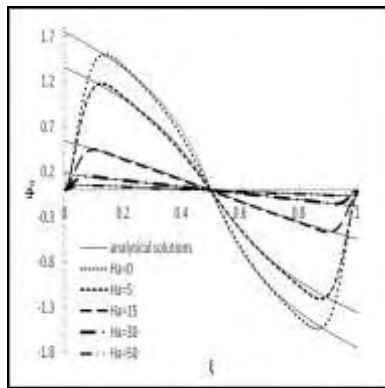




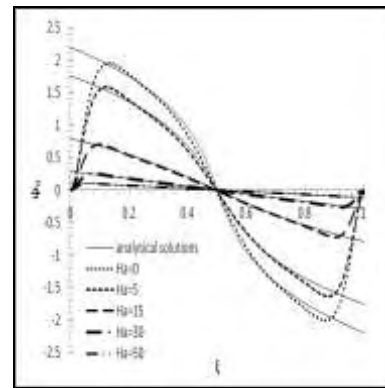
(a)  $R_s=200$



(b)  $R_s=1000$

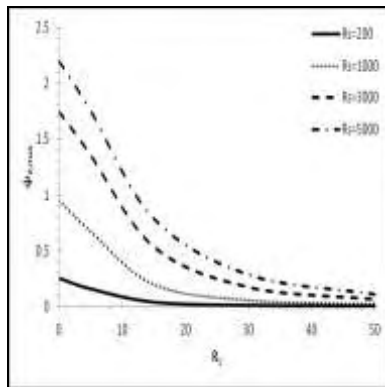


(c)  $R_s=3000$

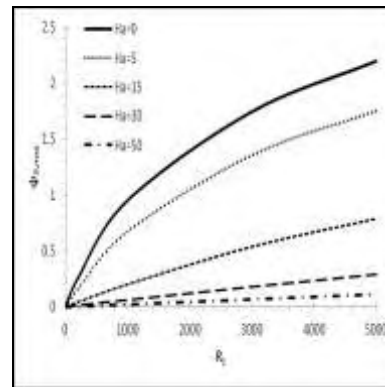


(d)  $R_s=5000$

**Fig. 5.19** Distribution of the core streamfunction  $\psi_0$  at mid-cavity height ( $z=0$ ) for various values of  $Ha$ : (a)  $R_s=200$ , (b)  $R_s=1000$ , (c)  $R_s=3000$ , (d)  $R_s=5000$

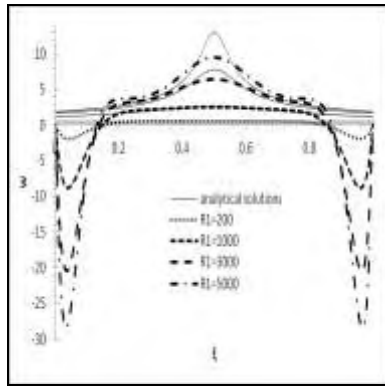


(a)

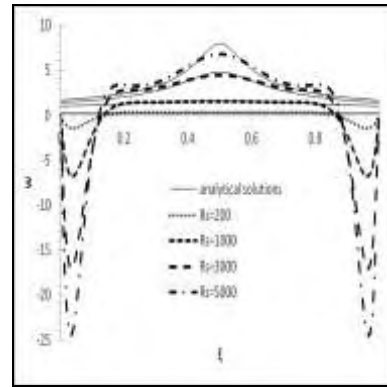


(b)

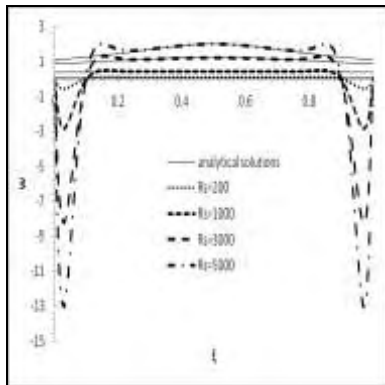
**Fig. 5.20** Distribution of the maximum analytical core streamfunction  $\psi_0$  for various values of (a)  $R_s$  and (b)  $Ha$



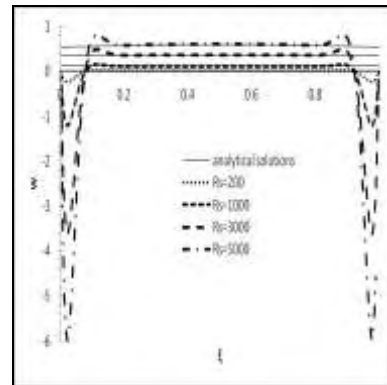
(a)  $Ha=0$



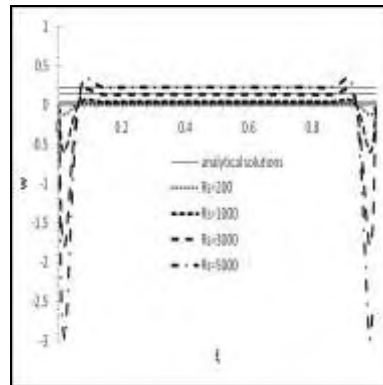
(b)  $Ha=5$



(c)  $Ha=15$



(d)  $Ha=30$



(e)  $Ha=50$

**Fig. 5.21** Distribution of the vertical velocity at mid-cavity height ( $z=0$ ) for various values of  $R_s$ : (a)  $Ha=0$ , (b)  $Ha=5$ , (c)  $Ha=15$ , (d)  $Ha=30$ , (e)  $Ha=50$

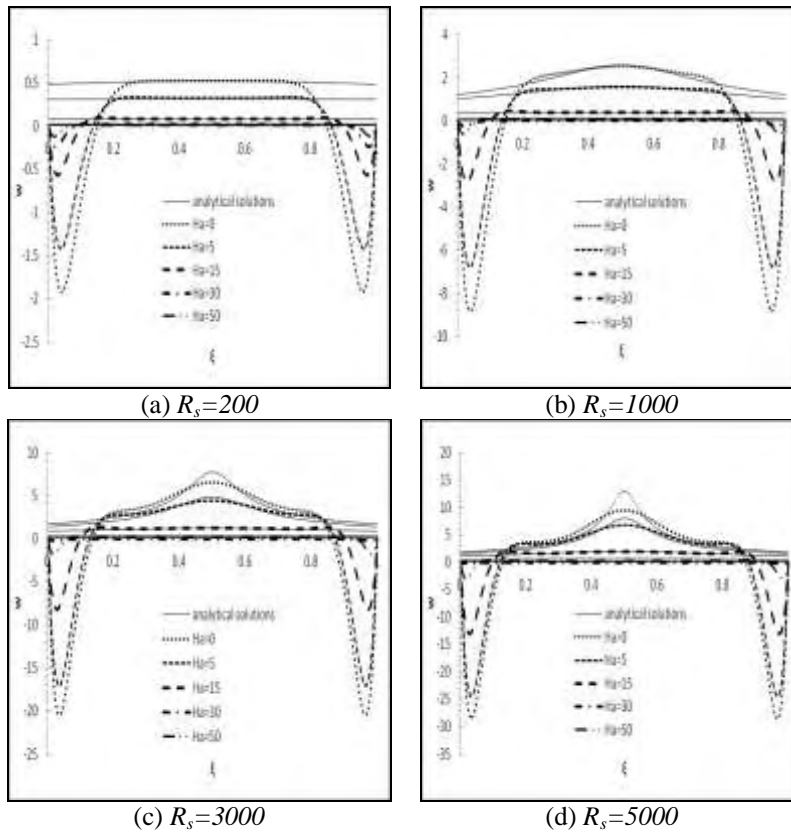


**Fig. 5.22** Distribution of the vertical velocity at mid-cavity height ( $z=0$ ) for various values of  $Ha$ : (a)  $R_s=200$ , (b)  $R_s=1000$ , (c)  $R_s=3000$ , (d)  $R_s=5000$

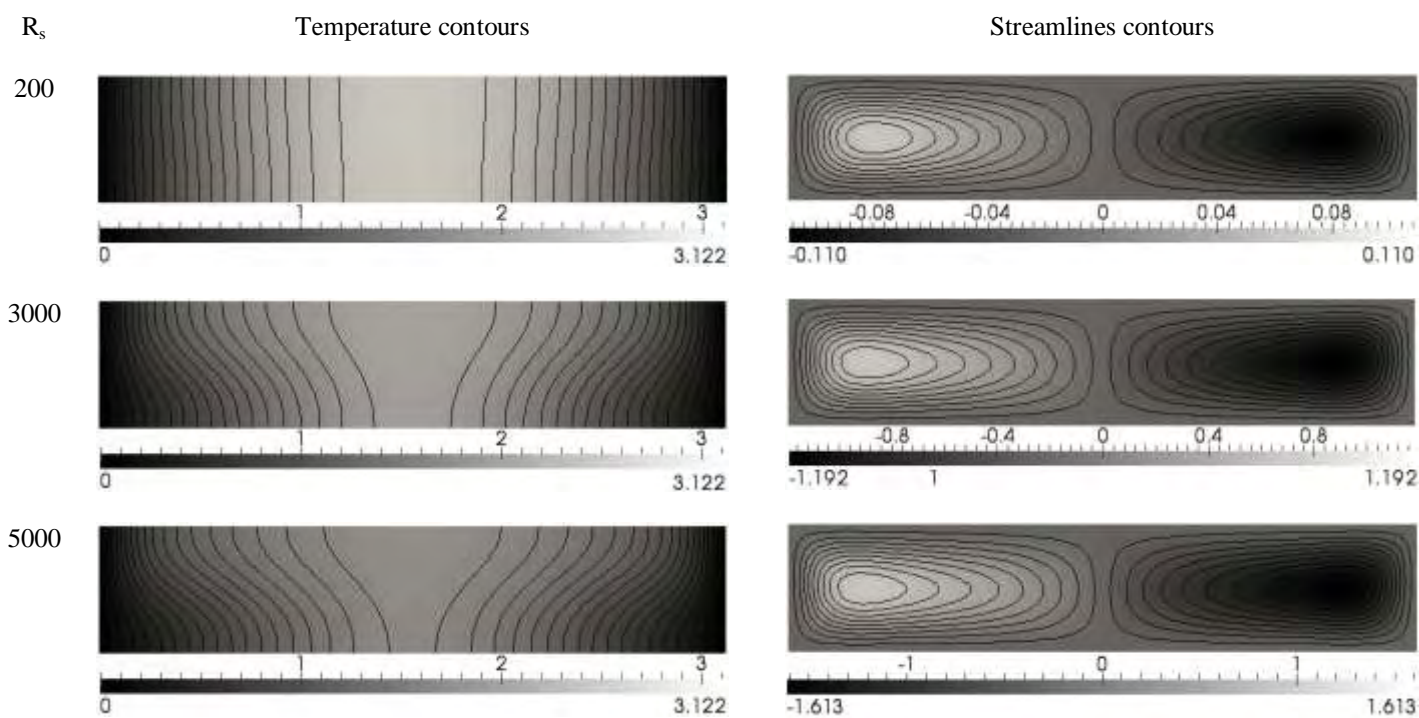


*Fig. 5.23 Temperature and streamlines contours for  $Ha=5$  and  $R_s=200, 3000$  and  $5000$*

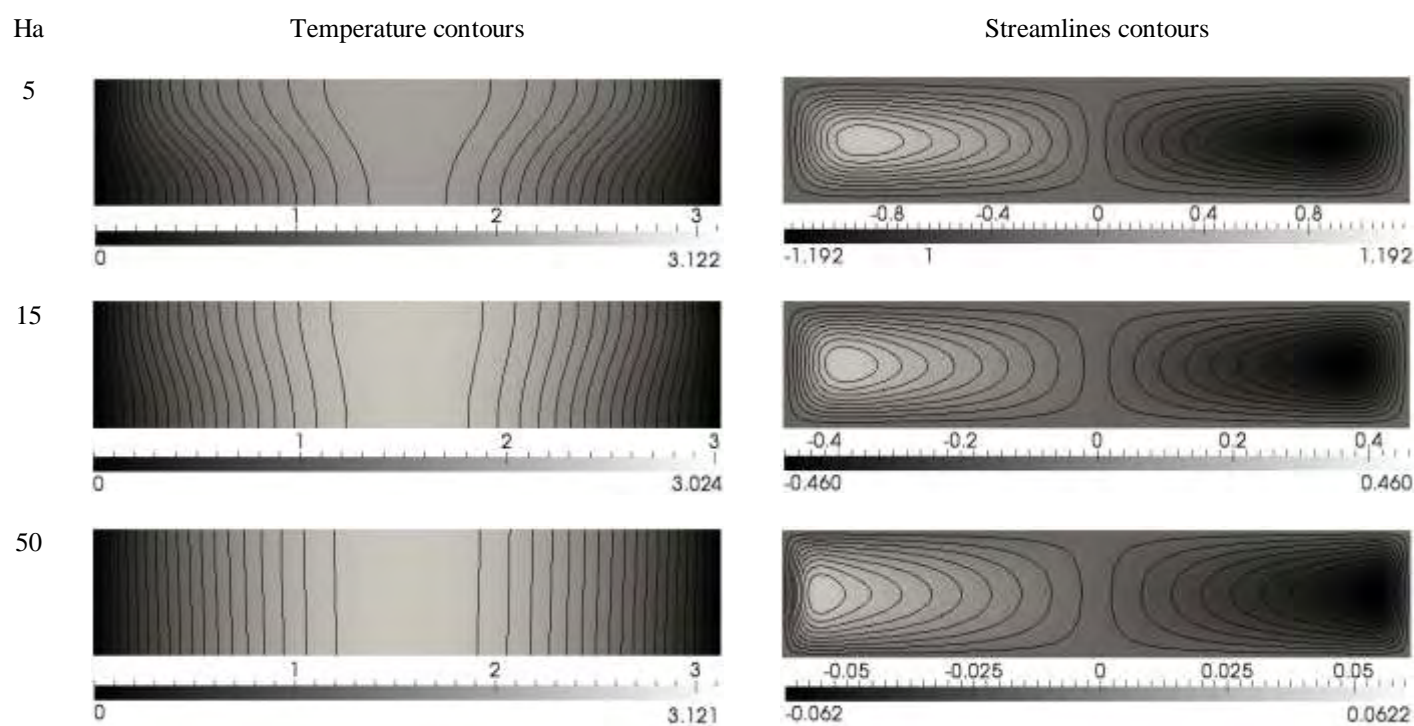


*Fig. 5.24 Temperature and streamlines contours for  $R_s=3000$  and  $Ha=5, 15$  and  $50$*

# CURRICULUM VITAE

## LEFTERIS TH. BENOS

(Last update: October 10, 2012)

### PERSONAL DETAILS

*Year of birth:* 1984

*Place of birth:* Volos

*Citizenship:* Greek

*Marital status:* Single

*Address:* Sikoutri 2, 38333 Volos, Greece

*Telephone:* 0030 6972781807, 0030 24210 74092

*E-mail:* [lefterisbenos@yahoo.gr](mailto:lefterisbenos@yahoo.gr)

### UNIVERSITY EDUCATION

2010–today Graduate studies (MSc), Mechanical Engineering Department, University of Thessaly, Volos, Greece.

*Grades: Advanced Transport Phenomena: 9/10, Advanced Fluid Mechanics: 8/10, Computational Fluid Dynamics & Heat Transfer/Finite Elements: 8/10, Kinetic Theory & Micro Fluid Dynamics: 8/10, Turbulence and industrial applications: 8.5/10, Thermal Systems Design: 8.5/10.*

To be accepted to the Master program I had to attend successfully six courses: *Partial Differential Equations, Fluid Mechanics, Transport Phenomena, Advanced Energy Conversion Systems, Thermal Process Equipment, Computer Programming.*

Thesis title: “*Analytical and numerical study of the magnetohydrodynamic natural convection in an internally heated horizontal shallow cavity*”

Thesis supervisor: Professor emeritus Nikolaos Vlachos

*Abstract: The two-dimensional MHD natural convection flow of an electrically conductive fluid in an internally heated horizontal shallow cavity with electrically insulated walls is studied. The case of adiabatic horizontal and isothermal vertical walls is considered while an external uniform magnetic field is applied in the vertical direction. The main feature of the present flow is a symmetric double-cell Hadley circulation with the fluid ascending in the centre of the cavity and descending near the vertical cold walls. The method of the matched asymptotic expansions is used to obtain solutions of the flow and heat transfer problem. This analysis which is valid for large cavity aspect ratios and for any magnetic field strength is particularly helpful for the determination of the flow field with inexpensive calculations. In addition to the analytical solution, the same flow is also studied numerically for a range of Hartmann, Prandtl and Rayleigh numbers in order to verify the accuracy and validity of the analytical results, to calculate the constants arising by the analytical approach and to characterize the non-linear regions of the flow. Finally, the analytical and numerical results were in good agreement indicating the correctness of the analysis and its applicability. This*

work was financially supported by the European Commission within the Association EURATOM-Hellenic Republic.

- 2009-10 Sales Manager of the multinational furniture company *Black Red White*.
- 2004-09 Undergraduate studies (BSc), Physics Department, Aristotle Univ. of Thessaloniki, Greece. Field of Applied and Environmental Physics  
Thesis title: *Study of wind potential of the wind farm in Alogorachi*  
Thesis supervisor: Assoc. Professor Alkiviadis Bais  
Abstract: *In this thesis the wind potential of the wind farm in Alogorachi, in Greece, is investigated from June 2007 to May 2008. The farm is located at the mountain Othris and at an altitude of 1652m. The main wind direction is northwest and the mean velocity is 6.79m/s. First of all, the measurements of the wind velocity were carried out by NRGIceFree3<sup>TM</sup> anemometers that are placed at a height of 55m. Then, the mean power per m<sup>2</sup> was estimated for each month. Furthermore, the mean power per m<sup>2</sup> was measured for the fictitious case where the anemometers were located at heights of 10m and 30m. The unreal velocities were estimated via the relationship  $U_s = U_{ref}(H_s/Z_{ref})^p$ , where  $U_{ref}$  and  $Z_{ref}$  stand for the reference velocity and reference height, respectively,  $U_s$  represents the wind velocity at  $H_s = 10m$  and  $H_s = 30m$  and  $p$  is a number that depends on the stability of the atmosphere. For the present study  $p$  was considered equal to 0.14. Finally, the total kinetic energy for 12 months was calculated for each case and a comparison between them was performed. Last but not least, this thesis has a comprehensive analysis on the wind energy, global warming and the climate changes around the world.*  
GPA: 10/10 (Excellent)
- 2003-04 Technical School of Engineering of the Hellenic Air Force Academy.

#### SCHOLARSHIPS – AWARDS

Scholarship of the Association EURATOM-Hellenic Republic.

#### RESEARCH INTERESTS

Computational Fluid Dynamics (CFD), Magnetohydrodynamics (MHD), MHD Turbulence, Plasma Physics, Kinetic Theory & Micro Fluid Dynamics, Environmental Science, Transport Phenomena, Magnetically Confined Fusion.

#### RESEARCH EXPERIENCE

*Graduate Researcher* - Laboratory of Fluid Mechanics & Turbomachines, Department of Mechanical Engineering, University of Thessaly.

#### PUBLICATIONS - PRESENTATIONS

1. C. Dritselis, A. Iatridis, I. Sarris, L. Benos and N. Vlachos, *Near wall coherent structures in MHD turbulent channel flow with heat transfer*, 7th National Conference on Fluid Flow Phenomena, Thessaloniki, 12-13 November 2010
2. L. Benos, I. Sarris and N. Vlachos, *Fusion resistive non-linear plasma solver based on the OpenFOAM cfd library*, 10<sup>th</sup> School of Fusion Physics & Technology, Volos, Greece, 9-13 May 2011.
3. L. Benos, S. Kakaratzas, I. Sarris and N. Vlachos, *Analytical and numerical study of the magnetohydrodynamic natural convection in an internally heated horizontal shallow cavity*, in preparation, 2012.

4. L. Benos, S. Kakaratzas, I. Sarris and N. Vlachos, *Analytical and numerical study of the magnetohydrodynamic natural convection in an internally heated horizontal shallow cavity*, 8th National Conference on Fluid Flow Phenomena, Volos, 16-17 November 2012.
5. S. Kakaratzas, L. Benos, I. Sarris and N. Vlachos, *Magnetohydrodynamic natural convection in annuli with respect to different aspect ratios*, 8th National Conference on Fluid Flow Phenomena, Volos, 16-17 November 2012.

#### PARTICIPATION IN CONFERENCES

1. 7th National Conference on Fluid Flow Phenomena, Thessaloniki, 12-13 Nov. 2010.
2. 9<sup>th</sup> School of Fusion Physics & Technology (technical assistant), Volos, 2010.
3. 10<sup>th</sup> School of Fusion Physics & Technology (technical assistant), Volos, 9-13 May 2011.
4. MHD Summer Program, Free University of Brussels, Belgium, 2011.
5. 8th National Conference on Fluid Flow Phenomena, Volos, 16-17 Nov. 2012.

#### VISITING PROFESSORSHIPS

1. Visiting Professor D. Carati, Free University of Brussels, Belgium, 2010.
2. Visiting Professor D. Carati, Free University of Brussels, Belgium, 2011.
3. Visiting Professor N. Pometescu, University of Craiova, Romania, 2011.

#### COMPUTER SKILLS

Open Field Orientation and Manipulation simulation package (OpenFOAM), Paraview (post processing package), Microcal Origin, Mathematica, Fortran 90/95, C<sup>++</sup> language.

#### OTHER AFFILIATIONS/MEMBERSHIPS

Active member of the CFD online forum (OpenFOAM)

President of Graduate & Doctoral Students, Mechanical Engineering, University of Thessaly.

#### LANGUAGES

Greek Native Language - English First Certificate.

#### OTHER INTERESTS

Football, Team Captain (4 years), Physics Department, Aristotle Univ. of Thessaloniki, Computers, Basketball, Kick-Boxing.